HEXIS

Empa

ON THE STRENGTH AND FAILURE OF AN ELECTROLYTE SUPPORTED SOLID OXIDE FUEL CELL

Dissertation zur Erlangung der Doktorwürde
an der
Montanuniversität Leoben

eingereicht von
Dipl. Ing. Felix Fleischhauer

Leoben, Januar 2016

Eidesstattliche Erklärung:

Ich erkläre an Eides statt, dass ich diese Arbeit selbstständig verfasst, andere als die angegebenen Quellen und Hilfsmittel nicht benutzt und mich auch sonst keiner unerlaubten Hilfsmittel bedient habe.

Affidavit:

I declare in lieu of oath, that I wrote this thesis and performed the associated research myself, using only literature cited in this volume.

Leoben, Januar 2016

Felix Fleischhauer

„Das Problem ist mit der Arbeit fertig zu werden,
in dem Gedanken nie und mit Nichts fertig zu werden.
Es ist die Frage weiter, rücksichtslos weiter oder aufhören, Schluss machen.
Es ist eine Frage des Zweifels, des Misstrauens und der Ungeduld."

Thomas Bernhard
(Aus der Rede zur Verleihung des Georg-Büchner-Preis 1970)

Danksagung/Acknowledgement

Mein Dank gilt zuvorderst Prof. Robert Danzer für die Bereitschaft mich als externen Doktoranden am *Institut für Struktur- und Funktionskeramik* (ISFK) aufzunehmen und meine Arbeit zu betreuen. Insbesondere der offene, vorbehaltlose, von immenser Sachkenntnis, Hilfsbereitschaft und Intuition geprägte Umgang hat mich stark beeindruckt und wird mich auch zukünftig prägen.

Des Weiteren möchte ich von Herzen Herrn Jakob Kübler danken, der als mein Vorgesetzter mich während meiner Zeit an der *Empa* an die Fraktographie und Schadensfallanalytik herangeführt hat und mich das Denken eines Detektivs lehrte. Auch sein Sinn für Organisation und Ordnung ist nicht spurlos an mir vorübergegangen.

Dr. Andreas Mai gebührt ebenfalls an dieser Stelle meine gesonderte Anerkennung, dafür dass er mir durch seinen vielschichtigen Einblick und ausgedehnte Gespräche, die verschiedensten Aspekte von Hochtemperaturbrennstoffzellen näher brachte und bis zum heutigen Tage bringt.

Ebenfalls möchte ich mich bei Prof. Alexander Michaelis bedanken. Seine Vorlesungen an der *TU-Dresden* haben den Grundstein für eine andauernde Leidenschaft bezüglich der Entwicklung von Hochtemperaturbrennstoffzellsystemen gelegt und mich überhaupt erst dazu bewogen mich einer solchen Thematik zu widmen.

Das Engagement des *Bundesamts für Energie* der Schweiz und von *Swisselectric Research* sei an dieser Stelle hervorgehoben. Beide Institutionen haben durch ihre Förderung das Entstehen dieser Arbeit im Rahmen des Projektes SOFC*H*-ESC (*BfE*-Vertragsnr.: 8100076; SI/500084-02) ermöglicht.

Ein überwiegender Teil der experimentellen Arbeiten wurde an der *Empa, Swiss Federal Laboratories for Materials Science and Technology, Laboratory for High Performance Ceramics*/Dübendorf, Schweiz durchgeführt, wo ich für die meiste Zeit meiner Promotion angestellt war. Ich möchte der *Empa* und insbesondere dem Labor für Hochleistungskeramik mit seinem Leiter Prof. Thomas Graule dafür danken, mir eine Arbeitsumgebung bereitgestellt zu haben, die in einem erheblichem Maße die Durchführbarkeit meiner Studien ermöglichte. Besonders seien die hervorragende

Ausstattung und die Möglichkeiten des Mechanik-Labors zu erwähnen auch wenn ich nicht mehr in den Genuss kam mit dem neuen Zeiss 3D-Stereo-Mirkoskop meine Fraktographie zu treiben. Die Arbeit zeichnete sich vor allem durch einen offenen, freundlichen Umgang aus. Ein Umgang der oft auch zum Ausgang führte. Danke Tzu-Wen für die Zeit innerhalb und ausserhalb des Büros *(Remember the Bridge!)*.

Herrn Ueli Weissen, Dr. J. Andreas Schuler, Dr. Boris Iwanschitz und überhaupt dem Hexis-Team möchte ich für die Versorgung mit Probenmaterial, die Nutzung ihrer Infrastruktur und für die vielen Diskussionen Danke sagen. Es freut und ehrt mich uber alle Maßen nach Jahren des fruchtvollen und äußert angenehmen Austausches Teil dieses unschlagbaren Teams geworden zu sein *(The power in [y]our Hand!)*.

Während meiner Promotion hatte ich Gelegenheit einige Wochen in Leoben verweilen zu dürfen, wo ich in kürzester Zeit so viele Proben zerbrochen habe wie vor mir wahrscheinlich keiner. Am Ende waren die Vorräte an Probenschachteln aufgebraucht. Neben vielen Scherben, gab es aber auch eine Menge wertvoller Gespräche und das eine oder andere Glaserl. Den Kollegen am ISFK möchte ich für diese Zeit danken und dabei die danach andauernde und hervorragende Kooperation mit Dr. Raul Bermejo herausstreichen.

Innerhalb des Projektes SOFC*H*-ESC war Herr Markus Linder als weiterer Doktorand mein Schicksalsgenosse. Aus diesem Zustand erwuchs ein gemeinsames Projekt, was hoffentlich in Form einer ordentlichen Veröffentlichung nach vielen Jahren seinen Abschluss finden wird. Unserer beiden Fünfte. Danke im Voraus.

Zu guter Letzt möchte ich den blauen Libellen für ihren jährlich wiederkehrenden Tanz Danke sagen. *Merci!*

Table of Content

Chapter 0

Introduction

0.1 Background

With the upcoming of high performance ceramics in the fifties and sixties of the last century an environment was established in which the foundations where laid regarding cost efficient processing of artificial new materials into new components and devices. This emerging of a new engineering material class propelled also the development of the so called solid oxide fuel cell (SOFC); a technology to transform efficiently chemical energy directly into electrical power. The unique characteristic of this ceramic based cell type is the utilization of a solid oxide electrolyte, which main characteristic is that it solely conducts oxygen ions at sufficiently high temperatures. The necessity of elevated temperatures becomes hereby also the key advantage as this kind of cell is the most tolerant among all fuel cells regarding the fuel type [1]. The potential fuels reach from gasified coal over natural gas to pure hydrogen, which opens up a multitude of potential applications. As one of the first manufacturers *Westinghouse* pioneered in the sixties with the manufacturing of the first SOFC, demonstrating the principle idea [2]. Several decades of research and development in academia and industry and several drawbacks later the technology has matured, which is for instance reflected in the fact that *Solid·Power* has achieved an initial electrical efficiency of 74% with a pre-commercial SOFC stack [3], while *Ceramic Fuel Cell Ltd.* has introduced its *Bluegen* system into the market with 60% ac net efficiency taking also the balance of plant into account [4]. The latter value has been achieved on a small scale and is predicted to be even increased when going to larger nominal power outputs, as the power demand of supporting components of the system can be reduced [5] (see Figure 0.1).

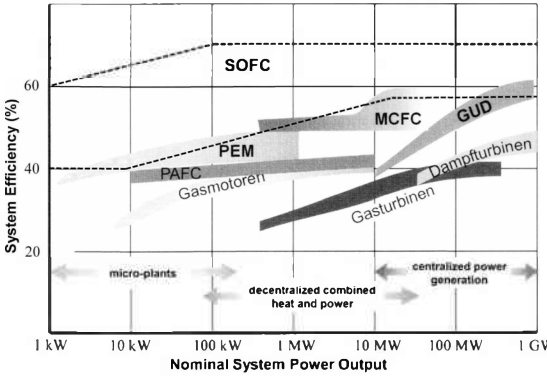

Figure 0.1: Comparison of different technologies for electrical power generation regarding the achievable plant efficiency and how it scales with the nominal power output of the plant. Original figure taken from [6] updated with the current prospective efficiencies of SOFC based plants.

Many countries are currently working on concepts to deal with the ever increasing demand of energy, while at the same time facing the inevitability to decrease the emission of pollutants and carbon dioxide. As for instance described consistently in the „Energiestrategie 2050", „Energiekonzept 2050" and „Energiestrategie Österreich (2020)" of the federal governments of Switzerland, Germany and Austria, respectively, a central role falls to the reduction of the consumption of primary energy resources. One way of achieving this goal, is to steadily increase the overall efficiency of the national heat and in particular electricity production. SOFC-technology fits right into these concepts. Not only because of its electrical performance, discussed above, but also since it can be operated efficiently at small power scales. As shown in Figure 0.1 many alternative technologies suffer quite severely with respect to their plant efficiency coming to small power scales, so that they are comparably limited. For that matter the efficiency of SOFC devices proofs to be less sensitive. This creates the opportunity to place small power plants in a decentralized manner at sites where the electricity is actually consumed – for

instance single family homes in middle and north Europe. Because of the additional heat demand especially during the winter seasons also the waste heat, these plants inevitably produce, can be directly used on site. This simple fact has led to the development of so called micro combined heat and power plants (μCHPs), which reach an overall utilization of the chemical stored energy of the consumed fuel of up to 95%. A wide spread installation of these systems can therefore significantly contribute to the solution of the current and future energy challenges.

Although some manufacturers namely *Ceramic Fuel Cell Ltd.*, *Hexis* and *Toyota/Aisin* already introduced first SOFC-based μCHPs into the market, these systems themselves have still to overcome certain challenges. First of all the costs related to production, installation and maintenance are at the moment too high for broad consumer acceptance. Further, robustness and longevity are issues, which are still subject to continuing optimization [7]. The here presented collection of studies is addressing the latter two issues as it is concerned with the mechanical robustness and service strength of the very core element of a SOFC-system, the fuel cell.

0.2 Solid oxide fuel cells

0.2.1 Working principle

A SOFC like any other fuel cell is an electrochemical device, transforming chemical energy into electricity and thus like any other cell requires three constituents as depicted in Figure 0.2: *(i)* an electrolyte, which separates spatially the oxidation and reduction reaction zones, which are *(ii)* the anode and *(iii)* the cathode, respectively. At the cathode oxygen gets reduced with four electrons towards two oxygen ions, which then enter the electrolyte:

$$O_{2(g)} + 4e^{-}_{(cath)} \rightarrow 2\,O^{2-}_{(el)} \tag{0.1}$$

The electrolyte exclusively conducts these oxygen ions to the anode where hydrogen is oxidized into water, while two electrons are released:

$$H_{2(g)} + O^{2-}_{(el)} \rightarrow H_2O_{(g)} + 2e^{-}_{(an)} \tag{0.2}$$

Typically SOFC-based systems do not run on just pure hydrogen, but are rather fed with a fuel consisting of hydrocarbons, such as for instance methane, methanol or

propane. Before entering the fuel cell these fuels are reformed either with water (steam reforming) and/or with oxygen (partial catalytic oxidation) and turned into most dominantly carbon monoxide and hydrogen [8]. Additionally to Equation (0.2) the carbon monoxide can be alternatively or simultaneously oxidised to CO_2 at the anode according to:

$$CO_{(g)} + O^{2-}_{(el)} \rightarrow CO_{2(g)} + 2e^{-}_{(an)} \tag{0.3}$$

However, as this reaction path possesses comparably slow reaction kinetics [9], predominantly the so called water gas shift reaction takes place:

$$CO_{(g)} + H_2O \rightarrow CO_{2(g)} + H_2 \tag{0.4}$$

where the carbon monoxide is oxidised with water, which is the product of Equation (0.2).

Combining Equation 0.1-0.4 leads to the overall reaction:

$$n\,H_2 + m\,CO + \frac{(n+m)}{2}\,O_2 \rightarrow n\,H_2O + m\,CO_2 \tag{0.5}$$

Three phases are required, in order for these single reactions to happen: First, a gaseous phase, which supplies the gaseous educts and leads away the gaseous products. Second, a phase, which conducts oxygen ions; and third an electrically conductive phase, which provides the electrons or electron holes, respectively. Only where these three phases come together, the so called triple phase boundary, the basic requirement, for these respective reactions to take place, are met. Note, that sometimes materials are used, which are mixed ionic and electronic conducting, thus representing the two required phases at once. Connecting the anode and cathode externally closes the circuit and the electrons released at the cathode can be transported to the anode.

In order to observe an electric current within this circuit, a driving electric potential is necessary. Like for every thermodynamic system, the driving force for a reaction is determined by the change of Gibbs free enthalpy. If the overall reaction happens within an electrochemical device, so that the reduction and oxidation takes place at spatially separated sites, this change in enthalpy can be translated into the so called Nernst potential (here for gaseous reactants) [10]:

$$U_{Nernst} = -\frac{\Delta g^0}{nF} - \frac{RT}{nF} ln \prod p_i^{\nu_i} \tag{0.6}$$

with Δg^0 being the temperature dependent standard free enthalpy of the reaction, n the number of transferred electrons, R the universal gas constant, F the Faraday constant, p_i the partial pressure and ν_i the stoichiometric pre-factor (negative sign if on the product side) of the respective species. In case of an SOFC, Equation (0.4) can be simplified to:

$$U_{Nernst} = \frac{RT}{4F} ln\left(\frac{p_{O_2}^C}{p_{O_2}^A}\right) \tag{0.7}$$

Here, the superscripts A or C refer to the anode and cathode, respectively. Equation (0.7) reveals that the cell voltage of a SOFC is solely dependent on the difference of the oxygen partial pressure between anode and cathode side, reflecting that the gradient in the chemical potential of the oxygen is the actual driving force behind its diffusion in form of oxygen ions through the electrolyte. Already from the Nernst equation it becomes clear, that when a current is drawn from the cell, therefore oxygen transferred to the anode side, the partial pressure of oxygen there is raised and the observed voltage declines. Apart from this pure thermodynamic phenomenon, this decay of the cell voltage is further increased by several losses. With the current also the finite ohmic resistance at which the charge carriers are conducted creates an over potential which follows Ohm's law and hence rises with the current linearly. Further losses are due to polarisation resistances, which reflect for instance the activation of certain kinetically hindered reaction steps (like charge transfer or vacancy creation) or the starvation of the reaction sites with fuel, as it is faster converted than it can be replenished via gas diffusion. These losses together with the drop in Nernst potential limit the power output a cell can deliver and determine the maximum efficiency it can be operated at.

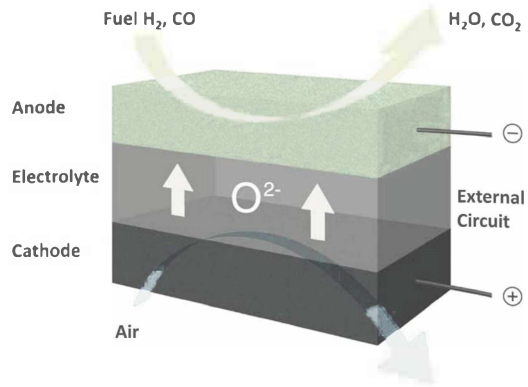

Figure 0.2: Working principle and structure of a solid oxide fuel cell

0.2.2 Cell

Having presented the basic principles of a SOFC, this section is concerned with how these fundamental aspects are actually translated into a working technology. The basic constituents of the cell are the anode, cathode and electrolyte.

(i) The main role of the electrolyte is to conduct exclusively oxygen ions, possessing a several orders of magnitude lower electronic conductivity. Otherwise a short circuit current would compensate immediately any electrical potential. For the cell to be efficient, the material to be chosen has to have sufficient ionic conductivity. The second task of the electrolyte is to completely separate the fuel and air or else leakage would decrease the Nernst voltage and lower the power output. Hence gas tightness has to be ensured. The established and mainly employed materials for these tasks are zirconia based electrolytes [11-13]. By doping zirconia with varying amounts of three valent metal oxides like yttria or scandia, extrinsic oxygen vacancies can be introduced into its structure (up to 5% of oxygen sites vacant), which gives rise to the high ionic conductivity [14, 15]. Basically the application of zirconia gives the SOFC its name and despite these high achievable vacancy

concentrations, which promote ionic conductivity, zirconia is also responsible for the high operating temperatures encountered in the derived systems, as it just reaches a sufficient conductivity between 600°C and 800°C, depending on the specific composition and thickness [13, 16, 17].

(ii) The cathode on the other hand, has to conduct oxygen ions and electrons and has to offer diffusive pathways for the diffusion of oxygen and thus will always possess a porous structure. Here the porosity has to be large enough, so that the polarisation losses due to fuel starvation are small, while a high ionic and electronic conductivity of the structure has to keep the ohmic losses to a minimum. It also must provide certain catalytic activity to promote the oxygen reduction, which is adjusted by the material selection and the total surface of the catalytic active sites. This is predominately achieved by manufacturing a porous ceramic composite out of $(La,Sr)MnO_{3-\delta}$ which is responsible for the catalytic activity and electronic conductivity and again zirconia based compounds, which provide the ionic conductivity [18, 19]. A common alternative to this composite is the application of mixed ionic-electronic conductors such as $(La,Sr)CoO_{3-\delta}$ or $(La,Sr)(Co,Fe)O_{3-\delta}$, which provide sufficient catalytic activity even at temperatures lower than 800°C [20-23].

(iii) The demands on the anode are almost equal, differing in the requirement to promote the oxidation of hydrogen. The material of choice providing excellent catalytic activity and low electronic resistance is nickel. Basically, all commercial SOFC-anodes rely on it [24]. As for the cathode it is combined with highly ionic conductive zirconia or ceria to form a porous cermet. However, nickel is prone to oxidation at elevated temperature, which sets certain boundaries on its application [25].

Today there are two popular commercial concepts among several others meeting these requirements: the anode supported and the electrolyte supported SOFC, as sketched in Figure 0.3.

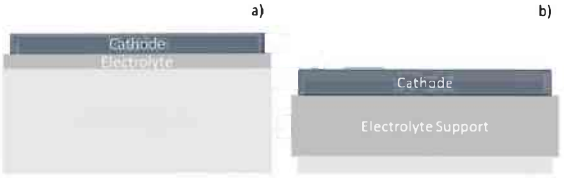

Figure 0.3: Principle sketch of an a) anode and b) electrolyte supported SOFC

The electrolyte supported SOFC distinguishes itself through the comparably thick electrolyte which gives the cell its structural integrity at the cost of a comparably high ohmic resistance, which has to be countered with an increased operating temperature. The two electrodes are screen printed typically in multiple sublayers onto the already dense electrolyte and then sintered [5, 26]. The main idea behind the anode supported cell on the other hand is to use a robust and comfortable to handle electrode to support a thin and dense electrolyte layer and subsequently the cathode layers. These layers are commonly applied by tape casting or screen printing methods [27]. Due to achievable thicknesses down to 8 µm, the ohmic losses at the electrolyte can be kept to a minimum, allowing lower operating temperatures.

0.2.3 Repeat unit

In order to utilize the potential of these cells, they must be incorporated into a functional unit to close the electrical circuit, to supply fuel and air and to lead the exhaust gases away, while preventing external and internal leakage of any of these gases [28]. During the electrochemical reactions at the anode (see Equations (0.2)-0.3)) electrons are released and have to be transferred to the cathode, where they reduce the oxygen (see Equation (0.1)). As the electrons are released and consumed throughout the whole cell area they have to be gathered and supplied to each area of the two electrodes. The electrodes possess a limited electrical conductivity, thus it is necessary to connect them homogeneously to a much more conductive current collecting component - the metallic interconnect (MIC). This keeps the conduction paths through the electrodes short and minimises the ohmic losses. Next to the current collection the MIC is also responsible for the homogeneous distribution of the

fuel and the air, which is for technical reasons the source of oxygen. An inhomogeneous distribution of the two process gases would lead to local starvation, so that the active cell area and the local Nernst potential would decrease. The MIC must then also provide the necessary pathways for the exhaust gases to escape. As the current collection demands a maximised contact area, while the gas distribution requires wide array of gas channels, the MICs structure must realise an optimum between these two contradicting features. The MIC must also provide for an optimal thermal management by redistributing an inhomogeneous heat release. Further, the design has to support a sufficient sealing at the edges of the cell to ensure that no leakage of any of the gases occurs. The last main task of the MIC is to clamp the cell and the sealing evenly. All of the above mentioned requirements demand that the MIC, the cell and the sealing, whose assembly reflects then the actual repeat unit (RU), possess compatible thermal expansion coefficients. Any design of the RU now seeks to provide the highest global performance of the cell by optimising the above mentioned problems.

0.2.4 Stack

One single cell and hence a repeat unit typically does not generate enough power for most potential applications, it is therefore connected in series to form a stack of several RUs. The stack is then regarded as the actual power generating entity for any SOFC-system with a nominal power output of several hundreds to a couple of thousand watts. Within the stack again channels are incorporated, supplying all repeat units evenly with fuel and air, while each MIC connects the anode side of one cell with the cathode side of the subsequent one. Next to an even gas distribution, the stack itself has to be laid out in a fashion so that the temperature distribution over the hole stack is sufficiently homogeneous, while the thermal mass should allow for fast start up times.

Figure 0.4 shows exemplarily a stack concept developed by the *Fraunhofer-Institute IKTS*-Dresden/Germany. Here the above made aspects and requirements for an optimal operation of an SOFC are realised. It is a planar rectangular closed cross flow design where the flow direction of the air and the fuel are perpendicular to each other. The active cell area is 127 cm^2. The fuel streams through two channels onto the cells. The non-consumed fuel is lead out of the stack via two channels at the

opposite side both towards an afterburner outside of the stack where it is burned off utilizing the additional heat. The sealing mounted at the sealing faces of each MIC closes off the fuel and the exhaust gas hermetically. The air flows openly and non-sealed in and out of the stack. The MIC structure is simply an array of parallel channels and sealing faces.

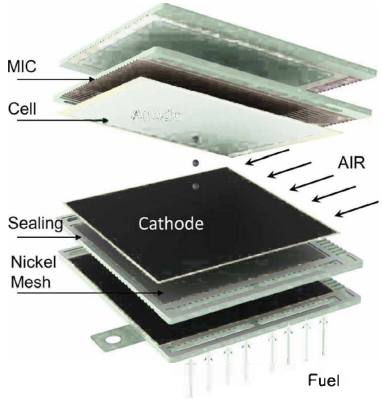

Figure 0.4: Stack concept MK 351 of the IKTS-Dresden/Germany (courtesy of IKTS) [29].

Figure 0.5 depicts an alternative concept of the μCHP manufacturer Hexis AG Winterthur/Switzerland. It is a unique planar radial open co-flow design. The fuel is distributed through a central hole, while the air is introduced via four air inlet channels at the outside and redirected from the inside back to the outside. The afterburner is integral to the stack and located directly at the circumference of the stack where air and the non-utilized fuel meet. This makes it a completely open stack as the air can in principle enter the anode side when the fuel flow stops. The necessary sealing of the fuel, air and exhaust gas during operation is realised just through respective sealing faces at the MIC which are simply pressed against the cell. Compared to the previous stack concept the MIC structure here is rather complex due to the radial geometry.

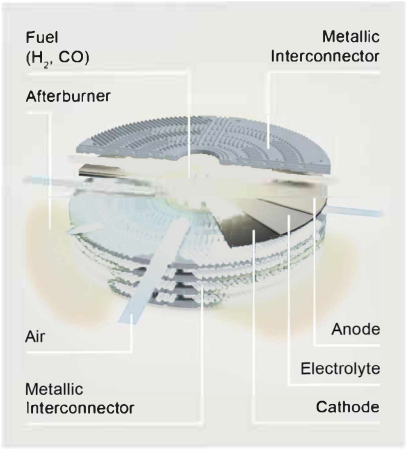

Figure 0.5: Current stack concept of Hexis AG Winterthur/Switzerland (courtesy of Hexis) [30].

Both concepts have overcome a series of difficult challenges, which was only achieved by extensive modelling of several different aspects influencing the cell performance, such as thermal-fluidic, electrochemical and thermo-mechanical models trying to elucidate the many parallel occurring processes and how they interact with each other at the cell [31-33], repeat unit [34, 35] and stack level [36-42]. Consequently after having taken principle design hurdles and found optimal material combinations, current research is mainly revolving around issues of longevity and robustness of today's fuel cell stacks. The main problems which are still being tackled are:

- the poisoning of the cathode's catalytic activity by volatile chromium species stemming from the commonly used MIC-materials or other components [43-46]
- the degradation of the contact resistance between the MIC and the cell [47-49]

- leakage at the sealing, as a consequence of thermo-mechanical instabilities or chemical interactions between MIC and sealing [50-52]
- intra cell leakage due to cell fracture or defect in the electrolyte [31, 53, 54]
- robustness of the cell against deliberate or accidental red-ox cycles [55-58]

0.3 Mechanical testing of thin sheets

One of the key issues of this study is the evaluation of the mechanical strength of thin (< 200 µm) brittle tapes and sheets. This requires methods that overcome a number of difficulties, which are related to the combination of *thin* and *brittle*. In this section these difficulties will be addressed.

The nature of brittle materials such as ceramics lies in the fact that they display inherently brittle fracture behaviour. Due to the absence of any plastic deformation local stress concentrations, as they occur at elastic inhomogeneities, cannot be equalised [59, 60]. Therefore, small flaws or irregularities in the microstructure, such as pores, agglomerates or scratches at the surface can act as origins for cracks, which then extend causing failure [61]. The criticality of such a flaw is practically described for a linear elastic, homogenous material via the stress concentration factor K_I, which is defined as [62, 63]:

$$K_I = \sigma \, Y\sqrt{\pi a} \tag{0.6}$$

with a being the characteristic size of the flaw, σ the applied stress at a sufficient distance uninfluenced by the flaw and Y a dimensionless geometric correction factor depending on the specific load situation and geometry of the flaw. Values of geometric correction factor for varying common cases can be found in literature [64-66]. A flaw now becomes critical, which means a crack will originate and expand, if the stress concentration factor exceeds the material characteristic resistance against crack extension, the so called fracture toughness K_{Ic} [62, 63]. Given the fracture toughness, based on Equation 0.6 the strength can now be expressed as a function of the flaw size.

Within a samples or components volume, typically a multitude of flaws of different sizes are present. Assuming a uniform stress state, the strength, the stress at which failure occurs, is determined by the largest flaw, because there the least stress is

required to reach a stress concentration factor, which equals the fracture toughness. In order to predict how the strength of a material, next to the fracture toughness, the size of the largest flaw has to be known. This fact creates one of the biggest problems, as this knowledge is hardly accessible.

The way this problem is resolved, is in general by turning to a probabilistic approach [67, 68]. *Jayatilaka* and *Trustrum* pointed out that for most cases the frequency density of critical flaws within a certain material decreases with the flaw size according to a simple power law and that under these circumstances the Weibull statistic is most suited to describe the strength distribution of this material [69]. Its fundamental equation is the Weibull distribution function, which expresses the probability of failure P as a function of the applied stress σ and the volume V the stress is applied at (here in the general form for an arbitrary tensile stress distribution) [61, 70]:

$$P(V,\sigma) = 1 - \exp\left[-\frac{1}{V_0}\int_V \left(\frac{\sigma}{\sigma_0}\right)^m dV\right] \tag{0.8}$$

m is hereby the Weibull modulus, reflecting the width of the distribution. V_0 is the reference Volume and σ_0 the characteristic strength. The latter two parameters are interdependent, meaning that for a given distribution several sets of V_0 and σ_0 are equivalent as long as the following relationship is fulfilled:

$$\sigma_{0_1}{}^m V_{0_1} = \sigma_{0_2}{}^m V_{0_2} \tag{0.9}$$

The most intriguing aspect implemented within Equation (0.8) is that the failure probability for a certain applied stress increases, if the stress is applied to a greater volume. This behaviour is intuitively comprehensible, when considering that it is simply more likely to find a large flaw within a larger volume than within a smaller one, as it is always the largest flaw, which determines the strength. This is an intrinsic property of brittle materials. Based on the above arguments, it becomes apparent that for most cases it is more suitable to describe the strength of a brittle material in terms of a failure probability at a given stress rather than giving an actual stress value called "strength".

In order to predict the failure probability the three Weibull parameters of a material have to be determined via suitable strength tests. The main goal hereby is to test a material at a volume scale which is not too far off from the expected loaded volume

during service. Otherwise an extrapolation towards larger or smaller volumes would cause large uncertainties as the Weibull modulus and the characteristic strength can only be determined with a finite certainty. Further the measured strength distribution might not even be representative or relevant if the scales of the measurement and the actual loaded volume during service differ too much [71-73]. The volume scale is in principle determined by the selected test method and the respective dimensions of the test rig and the samples. Furthermore, the test method must allow for easily machinable and testable sample geometries as the accuracy of the determination of the Weibull modulus and the characteristic strength immanently depends on the number of samples tested [68]. Also, an important requirement for a potential test method is that the applied force loading the sample results in a reproducible and defined stress field within the sample's volume, with the condition that from the force and the chosen geometry of the test set up a straight forward correlation between the applied force and the corresponding stress field can be deduced.

Following the above made requirements it is found that for brittle materials the in principle advantageous tensile test is not suitable. Despite the potential advantages of loading a large volume with an easy to describe uniform uniaxial stress, it has proven to be too demanding regarding sample preparation and the set-up of the test rig. Practically it is hardly possible to apply a homogenous uniform stress field to a brittle sample causing a large and difficult to handle error for each measurement. See for instance Ref. [74], where, although nominally uniformly loaded throughout the whole cross-section, all samples failed at or close to the carefully polished edges. This is a consequence of small errors in the alignment of the force introduction.

Therefore ceramics are typically tested in a bending regime, such as four or three point bending or the Ring-on-Ring test (see also standards *ISO 14704:2008*, *ISO 17565:2003* and *ISO 6474-1:2010*, respectively). All established bending tests rely on simple sample geometries such as bars and circular discs, while almost always analytically deducible relations between applied force F and obtained stress σ exist and can generally be expressed as [75]:

$$\sigma = g(geometry, \nu)\frac{F}{t^2} \tag{0.10}$$

with t the sample thickness and g being a dimensionless correction factor taking the geometry of the test rig and the sample and the Poisson's ratio of the tested material into account. However, this linear relationship between force and stress has a restriction. It is only valid, if the maximum deflection of the sample remains below about half of its thickness. Beyond this deflection, the relationship becomes more and more nonlinear. This is now the point where it becomes difficult to measure the strength distribution of thin sheet like samples for example ceramic tapes.

To illustrate these difficulties a 160 µm thick tape is considered. The first difference between thin and bulky samples is that the normalised bending stress over the sample height coordinate z, described generally by:

$$\frac{\sigma(z)}{\sigma_{max}} = \frac{2z - t}{t} \tag{0.11}$$

possesses a steep gradient. Therefore, any applied bending stress, which always reaches its maximum at the surface, decreases already 20 µm underneath the surface down to 75% of that maximum. Due to this steep stress drop, the probability to find a critical flaw rather scales with the loaded surface area S than the loaded volume. Hence, the Weibull distribution is written as:

$$F(V,\sigma) = 1 - \exp\left[-\frac{1}{S_0}\int_S \left(\frac{\sigma}{\sigma_0}\right)^m dS\right] \tag{0.12}$$

integrating over the stressed surface area.

For specimens obtained from a 160 µm thick tape a test configuration must be built, where the maximum deflection is lower than 80 µm. Miniaturizing the widely established and standardised four-point-bending test, would require a span width of less than 2 mm and much smaller dimensions of the single components of the rig. Furthermore, the downscaling would lead to increased and difficult to handle uncertainties regarding the applied stress [76].

Also for the Ring-on-Ring setup small test rig dimensions would be required. Figure 0.6 depicts the evolution of the maximum deflection of aforementioned tape, taking the Weibull strength parameters and the elastic constants as given in Table 0.1. The calculation is based on a finite element model of a Ring-on-Ring test rig. The dimensions are shown in Figure 0.7 [31] with respect to the diameter of the inner loading ring. For the deflection to be less than half of the sample thickness the

inner loading ring diameter should approximately not exceed 2-3 mm. Like for the four or three bending test the construction of a set up with these dimensions requiring a sufficiently small error are hardly achievable.

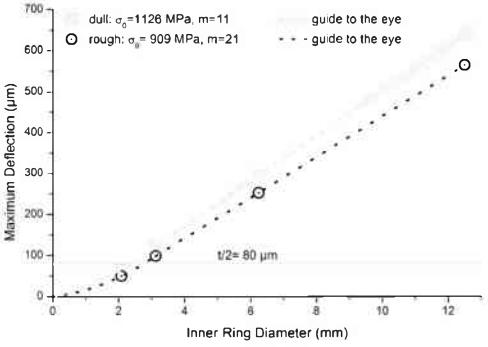

Figure 0.6: Expected maximum deflection for varying test rig size for a Ring-on-Ring geometry.

Hence, two approaches have been established to deal with this difficulty. The first is to test the strength in a large deflection mode preferably employing the Ring-on-Ring test, as this test allows neglecting edge defects of the samples. This then however requires a more advanced analysis of each measurement, which has to rely on a fairly accurate finite element model [77-80]. The model on the other hand demands the knowledge of all elastic parameters of the relevant components (rings and samples). Figure 0.8 shows the relationship between the effectively loaded surface and the test rig size with respect to the geometry depicted in Figure 0.7. By increasing the size, the loaded area can be increased along with the maximum deflection. However, Figure 0.8 already shows that this approach reaches fairly quickly its limit.

Table 0.1: Weibull parameter and elastic constants used for the Ring-on-Ring finite element simulation.

	Characteristic Strength σ_0 (MPa)	Weibull Modulus m	Surface Area S_0 (mm)	Young's Modulus E (GPa)	Poisson's Ratio ν
Rough tape side	909	21	11	214	0.32
Dull tape side	1126	11	18	214	0.32

Next to the careful determination of the actual fracture stress with regard to the measured fracture force, also the change of the effectively loaded surface area within a single sample set has to be accounted for in the statistical evaluation. This is because weaker samples are loaded on a comparably larger area than stronger ones [71]. Nonetheless, due to the large deflections the influence of friction becomes considerably large but is difficult to be factored into the finite element model. Hence, this test method can come with a considerable measurement uncertainty, which then can significantly disturb the correct determination of the Weibull modulus of a sample set of a material [81].

The second approach to directly and accurately measure the strength of thin and brittle samples is to come up with a test set up, which can be easily miniaturised, keeping the maximum deflection of the loaded samples and the measurement errors to a minimum, at the cost of a small loaded surface area. As a result of the search for a suitable set-up the Ball-on-three-Balls (B3B) test (see Figure 0.9), its correlation between applied stress and applied force and its sensitivity regarding mounting and sample errors has been revisited by *Börger* et al. [82-84]. It simply distinguishes itself by the fact that the support and load situation is always well-defined by the four contact points. The authors found that this test is particularly error tolerant. Further the test is very much suited for thin samples as the balls are readily available even in tiny sizes, while their correct arrangement is still feasible at small scales [85]. Another advantageous feature is that also rectangular samples are suited making the sample preparation cheap and easy [73, 86]. The main drawback here is however that the diameter of the effectively loaded surface area is just of the order of the sample thickness.

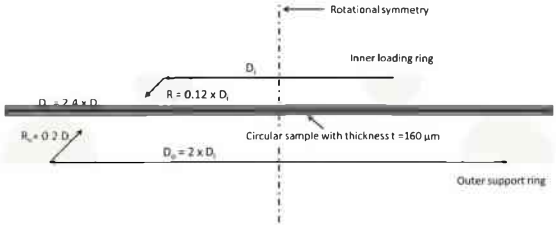

Figure 0.7: Dimensions of the Ring-on-Ring-setup with respect to the diameter of the inner loading ring (D_i), used for finite element simulation.

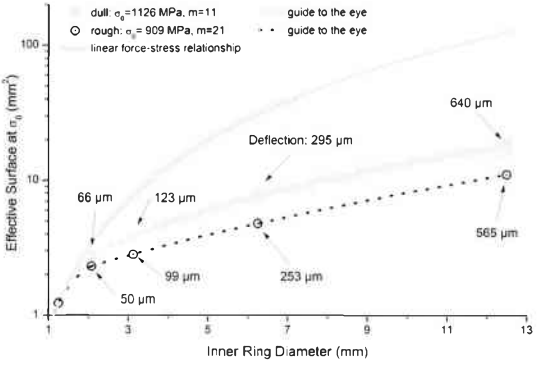

Figure 0.8: Effectively loaded surface area for varying Ring-on-Ring test rig size for the two simulated materials given in Table 0.1 and according to the linear theory, where the effectively loaded surface area corresponds to the area enclosed by the inner loading ring [87].

In order to measure the service relevant strength distribution of thin, extended and brittle components the ring-on-ring test in its large deflection mode remains despite the larger uncertainties the most suited set up. However, if it comes to evaluate the strength as a function of environmental influences like for instance atmosphere [88], temperature [89] or humidity [71, 90, 91] the B3B test becomes especially due to its accuracy the set-up of choice. Recent advances on this topic have led even to the possibility to measure the fracture toughness directly on thin samples [92] making it a powerful tool to directly and extensively characterise thin components regarding their intrinsic mechanical properties.

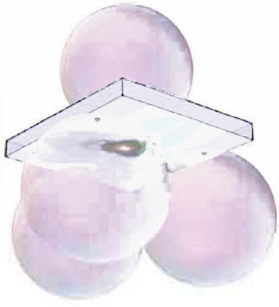

Figure 0.9: Principle sketch of the Balls-on-three-Balls strength test set-up (courtesy of *Raul Bermejo*) [90].

0.4 About this thesis

This thesis is a collection of publications containing recent research on the topic of mechanical strength and failure of commercial electrolyte supported solid oxide fuel cells (SOFCs) provided by *Hexis AG* (Winterthur/Switzerland). The general aim is to establish an understanding of the causes which lead to failure of the cells during operation, provide the necessary material data for a proper mechanical description of the cell and subsequently derive potential counter measures, which would reduce the probability of failure to a minimum. Based on this "single case study" general key aspects affecting the strength of these kind of cells are revealed from which general

design rules can be obtained, which will contribute to optimize other cells in different system environments.

To apply any design rule or to make an optimal material selection several material parameters of different cell components have to be gathered. Regarding the mechanical integrity of an electrolyte supported cell, the properties of the electrolyte are decisive. Hence, a large part of this thesis is concerned with proper and exhaustive description of several electrolyte materials, so that for any prospective electrolyte supported cell a well-founded selection regarding the electrolyte can be made.

The first study (Chapter 1) elucidates the stress situation such a cell is subjected to and the failure mechanism, which causes cracking and ultimately complete fracture. For this purpose a classical failure analysis with a holistic top down approach is undertaken, including the survey of all possible stress sources, while putting them in perspective with the findings of a broad fractographic investigation.

One approach in order to minimise fracture is of course to increase the cells strength. Prior to any optimization step, this property has to be properly described though. This is the aim of the following chapters, where the focus is set on the analysis of the strength of the electrolyte, which is the structural backbone of the cell. As the electrolyte is of brittle nature its strength has to be described in the form of a distribution which assigns any spatial applied stress distribution a probability of failure. This will be mainly addressed in Chapter 2, by testing several commercially available zirconia tapes covering the influence of surface structure, composition, tested sample surface and tape thickness at room temperature. Furthermore the phenomenon of sub critical crack growth (SCCG) is looked into, which can be responsible for a substantial weakening of zirconia based materials. Secondly the influence of an increased temperature on the strength distribution and SCCG is investigated in Chapter 3.

The final study, Chapter 4, covers the influence of the two electrodes on the fracture behaviour of the cell with regard to temperature, ageing and atmospheres. Therefore, drawing a comprehensive picture of the strength of the cell, by which mechanisms it is governed and how it is affected by the environment.

0.5 References

[1] M.L. Perry, T.F. Fuller, Journal of The Electrochemical Society, 149 (2002) S59.
[2] J. Weissbart, R. Ruka, Journal of The Electrochemical Society, 109 (1962) 723-726.
[3] S. Modena, in: 5th IPHE Higher Educational Round, Rome, 2014.
[4] K. Föger, P. Payne, in: N. Christiansen, B.H. Hansen (Eds.) 11th European SOFC Forum, European Fuel Cell Forum AG, Lucerne, 2014, pp. A05-17-A05-24.
[5] S.P.S. Badwal, K. Foger, Ceramics International, 22 (1996) 257-265.
[6] K. Ledjeff-Hey, F. Mahlendorf, J. Roes, Brennstoffzellen - Entwicklung, Technologie, Anwendung, Müller-Verlag, 2000.
[7] A.M. Kusnezoff, J. Schiel, cfi/Berichte DKG, 90 (2013) E27-E33.
[8] R.M. Ormerod, Chapter 12 - Fuels and Fuel Processing, in: S.C. Singhal, K. Kendal (Eds.) High Temperature and Solid Oxide Fuel Cells, Elsevier Science, Amsterdam, 2003, pp. 333-361.
[9] Y. Matsuzaki, I. Yasuda, Journal of The Electrochemical Society, 147 (2000) 1630-1635.
[10] W. Winkler, Chapter 3 - Thermodynamics, in: S.C. Singhal, K. Kendal (Eds.) High Temperature and Solid Oxide Fuel Cells, Elsevier Science, Amsterdam, 2003, pp. 53-82.
[11] J.W. Fergus, Journal of Power Sources, 162 (2006) 30-40.
[12] T. Ishihara, N.M. Sammes, O. Yamamoto, Chapter 4 - Electrolytes, in: S.C. Singhal, K. Kendal (Eds.) High Temperature and Solid Oxide Fuel Cells, Elsevier Science, Amsterdam, 2003, pp. 83-117.
[13] S.P.S. Badwal, F.T. Ciacchi, D. Milosevic, Solid State Ionics, 136-137 (2000) 91-99.
[14] V.V. Kharton, F.M.B. Marques, A. Atkinson, Solid State Ionics, 174 (2004) 135-149.
[15] J. Kimpton, T.H. Randle, J. Drennan, Solid State Ionics, 149 (2002) 89-98.
[16] J.B. Goodenough, Ann. Rev. Mater. Res., 33 (2003) 91-128.
[17] A. Nakamura, J.B. Wagner Jr., Journal of the Elektrochemial Society, 133 (1986) 1542-1548.
[18] S.P. Jiang, Journal of Materials Science, 43 (2008) 6799-6833.
[19] S.P.S. Badwal, S. Giddey, C. Munnings, A. Kulkarni, Journal of the Australien Ceramics Society, 50 (2014) 23-37.
[20] A. Mai, V.A. Haanappel, F. Tietz, D. Stöver, Solid State Ionics, 177 (2006) 2103-2107.
[21] A. Mai, V.A. Haanappel, S. Uhlenbruck, F. Tietz, D. Stöver, Solid State Ionics, 176 (2005) 1341-1350.
[22] J. Yang, H. Muroyama, T. Matsui, K. Eguchi, International Journal of Hydrogen Energy, 35 (2010) 10505-10512.
[23] C. Sun, R. Hui, J. Roller, J Solid State Electrochem, 14 (2009) 1125-1144.
[24] P.I. Cowin, C.T.G. Petit, R. Lan, J.T.S. Irvine, S. Tao, Advanced Energy Materials, 1 (2011) 314-332.
[25] J.L. Young, V. Vedahara, S. Kung, S. Xia, V. Birss, ECS Transactions, 7 (2007) 1511-1519.
[26] S. Gamble, Materials Science and Technology, 27 (2011) 1485-1497.
[27] F. Tietz, H.-P. Buchkremer, D. Stöver, Solid State Ionics, 152 (2002) 373-381.
[28] K. Kendall, N.Q. Minh, S.C. Singhal, Chapter 8 - Cell and Stack Designs, in: S.C. Singhal, K. Kendal (Eds.) High Temperature and Solid Oxide Fuel Cells, Elsevier Science, Amsterdam, 2003, pp. 197-228.

[29] S. Megel, M. Kusnezoff, N. Trofimenko, V. Sauchuk, A. Michaelis, A. Venskutonis, K. Rissbacher, W. Kraussler, M. Brandner, C. Bienert, ECS Transactions, 35 (2011) 269-277.
[30] A. Mai, B. Iwanschitz, U. Weissen, R. Denzler, D. Haberstock, V. Nerlich, A. Schuler, in: S.C. Singhal, K. Eguchi (Eds.) ECS Transactions, 2011, pp. 87-95.
[31] J. Kuebler, U.F. Vogt, D. Haberstock, J. Sfeir, A. Mai, T. Hocker, M. Roos, U. Harnisch, Fuel Cells, 10 (2010) 1066-1073.
[32] L. Holzer, B. Münch, B. Iwanschitz, M. Cantoni, T. Hocker, T. Graule, Journal of Power Sources, 196 (2011) 7076-7089.
[33] R. Bove, S. Ubertini, Journal of Power Sources, 159 (2006) 543-559.
[34] D. Larrain, F. Maréchal, D. Favrat, Journal of Power Sources, 131 (2004) 304-312.
[35] M. Linder, T. Hocker, L. Holzer, K.A. Friedrich, B. Iwanschitz, A. Mai, J.A. Schuler, Journal of Power Sources, 272 (2014) 595-605.
[36] A. Nakajo, P. Tanasini, S. Diethelm, D. Favrat, Journal of The Electrochemical Society, 158 (2011) B1102-B1118.
[37] A. Nakajo, Z. Wuillemin, P. Metzger, S. Diethelm, G. Schiller, D. Favrat, Journal of The Electrochemical Society, 158 (2011) B1083-B1101.
[38] A. Nakajo, Z. Wuillemin, J. Van herle, D. Favrat, Journal of Power Sources, 193 (2009) 203-215.
[39] A. Nakajo, Z. Wuillemin, J. Van herle, D. Favrat, Journal of Power Sources, 193 (2009) 216-226.
[40] S.S. Wei, T.H. Wang, J.S. Wu, Energy, 69 (2014) 553-561.
[41] M. Roos, E. Batawi, U. Harnisch, T. Hocker, Journal of Power Sources, 118 (2003) 86-95.
[42] J. Mantzaras, S.A. Freunberger, F.N. Büchi, M. Roos, W. Brandstätter, M. Prestat, L.J. Gauckler, B. Andreaus, F. Hajbolouri, S.M. Senn, CHIMIA International Journal for Chemistry, 58 (2004) 857-868.
[43] S.P. Jiang, X. Chen, International Journal of Hydrogen Energy, 39 (2014) 505-531.
[44] M. Stanislowski, J. Froitzheim, L. Niewolak, W. Quadakkers, K. Hilpert, T. Markus, L. Singheiser, Journal of Power Sources, 164 (2007) 578-589.
[45] J.A. Schuler, C. Gehrig, Z. Wuillemin, A.J. Schuler, J. Wochele, C. Ludwig, A. Hessler-Wyser, Journal of Power Sources, 196 (2011) 7225-7231.
[46] E. Bucher, M. Yang, W. Sitte, Journal of The Electrochemical Society, 159 (2012) B592-B596.
[47] Z. Yang, International Materials Reviews, 53 (2008) 39-54.
[48] W. Quadakkers, J. Piron-Abellan, V. Shemet, L. Singheiser, Materials at high temperatures, 20 (2003) 115-127.
[49] M. Linder, T. Hocker, L. Holzer, K.A. Friedrich, B. Iwanschitz, A. Mai, J.A. Schuler, Journal of Power Sources, 243 (2013) 508-518.
[50] I. Donald, P. Mallinson, B. Metcalfe, L. Gerrard, J. Fernie, Journal of Materials Science, 46 (2011) 1975-2000.
[51] A.A. Reddy, D.U. Tulyaganov, V.V. Kharton, J.M. Ferreira, Journal of Solid State Electrochemistry, 19 (2015) 2899-2916.
[52] N.H. Menzler, D. Sebold, M. Zahid, S.M. Gross, T. Koppitz, Journal of Power Sources, 152 (2005) 156-167.
[53] N.H. Menzler, P. Batfalsky, S.M. Gross, V. Shemet, F. Tietz, Post-Test Characterization of an SOFC Short Stack After 17,000 hours of Steady Operation, in: S.C. Singhal, K. Eguchi (Eds.) Solid Oxide Fuel Cells 12, 2011, pp. 195-206.
[54] S. Onuki, F. Iguchi, M. Shimizu, T. Kawada, H. Yugami, ECS Transactions, 68 (2015) 2421-2428.

[55] A. Faes, Z. Wuillemin, P. Tanasini, N. Accardo, J. Van Herle, Journal of Power Sources, 196 (2011) 3553-3558.
[56] A. Faes, Z. Wuillemin, P. Tanasini, N. Accardo, S. Modena, H.J. Schindler, M. Cantoni, H. Lübbe, S. Diethelm, A. Hessler-Wyser, J. Van herle, Journal of Power Sources, 196 (2011) 8909-8917.
[57] A. Faes, A. Nakajo, A. Hessler-Wyser, D. Dubois, A. Brisse, S. Modena, J. Van herle, Journal of Power Sources, 193 (2009) 55-64.
[58] A. Faes, J.-M. Fuerbringer, D. Mohamedi, A. Hessler-Wyser, G. Caboche, J. Van herle, Journal of Power Sources, 196 (2011) 7058-7069.
[59] J.B. Wachtman, W.R. Cannon, M.J. Matthewson, Mechanical properties of ceramics, John Wiley & Sons, 2009.
[60] S. Somiya, Handbook of Advanced Ceramics: Materials, Applications, Processing, and Properties, Academic Press, 2013.
[61] R. Danzer, T. Lube, P. Supancic, R. Damani, Advanced Engineering Materials, 10 (2008) 275-298.
[62] B. Lawn, Fracture of Brittle Solids, Cambridge University Press, Cambridge, 1993.
[63] D. Gross, T. Seelig, Fracture Mechanics: With an Introduction to Micromechanics, Springer Berlin Heidelberg, 2011.
[64] Y. Murakami, Stress intensity factors handbook, Pergamon, 1987.
[65] J.C. Newman, I.S. Raju, Engineering Fracture Mechanics, 15 (1981) 185-192.
[66] S. Strobl, P. Supancic, T. Lube, R. Danzer, Journal of the European Ceramic Society, 32 (2012) 1491-1501.
[67] R. Danzer, Journal of the European Ceramic Society, 10 (1992) 461-472.
[68] R. Danzer, T. Lube, P. Supancic, Zeitschrift Fur Metallkunde, 92 (2001) 773-783.
[69] A.D.S. Jayatilaka, K. Trustrum, Journal of Materials Science, 12 (1977) 1426-1430.
[70] W. Weibull, Journal of applied mechanics, 18 (1951) 293-297.
[71] F. Fleischhauer, M. Terner, R. Bermejo, R. Danzer, T. Graule, A. Mai, J. Kuebler, Journal of Power Sources 275 (2015) 217-226.
[72] R. Danzer, Journal of the European Ceramic Society, 26 (2006) 3043-3049.
[73] R. Danzer, P. Supancic, W. Harrer, Journal of the Ceramic Society of Japan, 114 (2006) 1054-1060.
[74] A. Faes, H.L. Frandsen, A. Kaiser, M. Pihlatie, Fuel Cells, 11 (2011) 682-689.
[75] W.C. Young, R.G. Budynas, Roark's Formulas for Stress and Strain, 7th ed., MacGraw-Hill, New York, 2002.
[76] T. Lube, M. Manner, R. Danzer, Fatigue & Fracture of Engineering Materials & Structures, 20 (1997) 1605-1616.
[77] J. Malzbender, R.W. Steinbrech, Journal of the European Ceramic Society, 27 (2007) 2597-2603.
[78] N. Orlovskaya, S. Lukich, G. Subhash, T. Graule, J. Kuebler, Journal of Power Sources, 195 (2010) 2774-2781.
[79] A. Selcuk, A. Atkinson, Journal of the American Ceramic Society, 83 (2000) 2029-2035.
[80] R. Kao, N. Perrone, W. Capps, Journal of the American Ceramic Society, 54 (1971) 566-&.
[81] R. Bermejo, P. Supancic, R. Danzer, Journal of the European Ceramic Society, (2012).
[82] A. Börger, P. Supancic, R. Danzer, Journal of the European Ceramic Society, 22 (2002) 1425-1436.

[83] A. Börger, P. Supancic, R. Danzer, Journal of the European Ceramic Society, 24 (2004) 2917-2928.
[84] R. Danzer, W. Harrer, P. Supancic, T. Lube, Z. Wang, A. Börger, Journal of the European Ceramic Society, 27 (2007) 1481-1485.
[85] W. Harrer, R. Danzer, P. Supancic, T. Lube, in: Key Engineering Materials, Trans Tech Publ, 2009, pp. 176-184.
[86] R. Wagner, W. Harrer, R. Danzer, in: CFI. Ceramic forum international, Göller, 2009.
[87] H. Fessler, D. Fricker, Journal of the American Ceramic Society, 67 (1984) 582-588.
[88] F. Fleischhauer, R. Bermejo, R. Danzer, A. Mai, T. Graule, J. Kuebler, Journal of Power Sources, 297 (2015) 158-167.
[89] F. Fleischhauer, R. Bermejo, R. Danzer, T. Graule, A. Mai, J. Kuebler, Journal of Power Sources, 273 (2015) 237-243.
[90] R. Bermejo, P. Supancic, C. Krautgasser, R. Morrell, R. Danzer, Engineering Fracture Mechanics, 101 (2013) 108-121.
[91] C. Krautgasser, R. Danzer, P. Supancic, R. Bermejo, Journal of the European Ceramic Society, 35 (2015) 1823-1830.
[92] S. Rasche, S. Strobl, M. Kuna, R. Bermejo, T. Lube, Procedia Materials Science, 3 (2014) 961-966.

Chapter 1

FAILURE ANALYSIS OF ELECTROLYTE-SUPPORTED SOLID OXIDE FUEL CELLS

Journal of Power Sources 258 (2014) 382-390

Felix Fleischhauer[1,2], Andreas Tiefenauer[3], Thomas Graule[1], Robert Danzer[2], Andreas Mai[4], Jakob Kuebler[1]

[1]Empa, Swiss Federal Laboratories for Materials Science and Technology, Laboratory for High Performance Ceramics, Ueberlandstr. 129, 8600 Duebendorf, Switzerland

[2]Institut für Struktur-und Funktionskeramik, Montanuniversität Leoben, Peter-Tunner-Str. 5, 8700 Leoben, Austria

[3]ZHAW Zürich University of Applied Sciences, Institute of Computational Physics, 8401 Winterthur, Switzerland

[4]Hexis Ltd., Zum Park 5, 8404 Winterthur, Switzerland

Abstract

For solid oxide fuel cells (SOFCs) one key aspect is the structural integrity of the cell and hence its thermo-mechanical long term behaviour. The present study investigates the failure mechanisms and the actual causes for fracture of electrolyte supported SOFCs which were run using the current μCHP system of Hexis AG, Winterthur/Switzerland under lab conditions or at customer sites for up to 40,000 h. In a first step several operated stacks were demounted for post-mortem inspection, followed by a fractographic evaluation of the failed cells. The respective findings are then set into a larger picture including an analysis of the present stresses acting on the cell like thermal and residual stresses and measurements regarding the temperature dependent electrolyte strength. For all investigated stacks, the mechanical failure of individual cells can be attributed to locally acting bending loads, which rise due to an inhomogeneous and uneven contact between the metallic interconnect and the cell.

1.1 Introduction

1.1.1 Background

Solid Oxide Fuel Cell (SOFC)-based systems are promising candidates for the conversion of chemical energy stored in natural gas or hydrogen into electricity. Due to the direct electro-chemical process it is possible to reach electrical efficiencies of 70% and more. Therefore, a lot of effort has been undertaken to develop systems which provide these high efficiencies while using materials and processing routes which are commercially acceptable. After several decades of intensive fundamental and materials research some systems are on the market (for instance the *BlueGen* of *Ceramic Fuel Cell Ltd.* and *Bloom's Energy Server* of *Bloom Energy*) or are close to their introduction (e.g. the *Galileo 1000 N* of *Hexis*). But despite the progress which is reflected in the availability of these devices nowadays, there is still room for improvement. Especially the long term issues have gotten more and more into the focus of the respective manufacturers. Some of the main problems which need to be improved are anode degradation, oxidation of the metallic interconnects, chromium poisoning of the cathode and the long-term thermomechanical stability of the whole cell and that within the frame of real operating conditions, like multiple thermo and redox cycles, variation in the quality of gas composition and accidental exposure to sulphur [1-4].

In this study the fracture behaviour and the individual causes for cell fracture of electrolyte supported fuel cells under real operating conditions are investigated. The examined cells were provided by *Hexis AG* in Switzerland and run in the company's current SOFC-System, the *Galileo 1000 N*.

One of the main tasks of the electrolyte is to physically separate the fuel from its oxidant, which it fails after its fracture. In any case the resulting intra cellular leakage will have a short- or long-term impact on the overall stack performance and could in the worst case lead to the instantaneous death of the respective fuel cell system [5]. Some experimental works have already been published regarding the mechanical stability of electrolyte supported cells [6-8] and the fracture behaviour outside a system at ambient conditions [9, 10], but so far none to our knowledge where cell fracture has been considered and investigated within the environment of an actual operating system.

1.1.2 System and Stack

The *Galileo 1000 N* employs a stack with a planar open radial design as sketched in Figure 1.1. Since the stack is "open", cells are required to maintain their structural integrity upon multiple redox-cycling. Currently, only electrolyte supported cells are able to fulfil this demand while having the drawback of a higher ohmic resistance compared to anode supported cells. On the other hand the open design allows the stack mounting to be a relative simple process. The nominal operating temperature is 850°C, measured at the bottom metallic interconnect. The fuel is supplied after being partially catalytically oxidized through the central hole of the stack onto the cell via the inner gas inlet channels of the anode side of the metallic interconnect (MIC) (see Figure 1.1). A fuel sealing plane at the opposite side prevents leakage onto the cathode. The air streams from the outside along four inlet channels towards the centre. It then flows back through the flow-field to the outer edge, where the non-utilised fuel is burned off and produces additional heat.

The MIC is a CrFe5 alloy manufactured and delivered by *Plansee SE* (Reutte, Austria) with a thermal expansion coefficient which matches that of the cell. The zirconia-electrolyte is purchased from *Nippon Shokubai* (Tokyo, Japan) and contained either 3 mol% of Y_2O_3 (3YSZ) or 6 mol% Sc_2O_3 (6ScSZ). These compositions were chosen due to their superior mechanical strength compared to the common electrolytes with 10 mol% Sc_2O_3 (10Sc1CeSZ) or 8 mol% Y_2O_3 (8YSZ) according to the supplier's data sheet. The discs are screen-printed with a $La_{0.75}Sr_{0.2}MnO_{3-\delta}$(LSM)-8YSZ-cathode and a Ni-$Ce_{0.4}Gd_{0.6}O_{2-\delta}$-anode developed by Hexis.

In order to understand the mechanisms which are responsible for cell fracture, stacks with a different operational history but the same design were chosen for post mortem inspection and fractography. Results from visual, light- and electron-microscopic analysis are then considered in a comprehensive context, laying the focus in particular on the mechanical behaviour of the electrolyte, as the element providing the cells integrity.

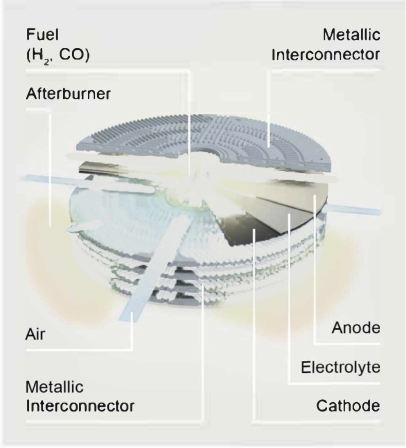

Figure 1.1: Working principle of the stack of the *Galileo 1000 N* (courtesy of *Hexis AG*).

1.2 Failure Analysis

1.2.1 Post Mortem Inspection and Fractography

Three stacks with 3YSZ and six stacks with 6ScSZ electrolytes were taken for post mortem inspection. Each system was running either at *Hexis* or at customer sites under real operational conditions in the frame of the German *CALLUX* project [11]. The operating time ranges from 300 up to 40'000 hours, the count of complete redox-cycles a stack had undergone from one to fourteen. After demounting, all examined stacks contained ruptured cells, while showing no severe or discontinuous loss in the overall performance during operation. This already indicates that the present stack design is relatively tolerant towards fracture and the resulting intra cellular leakage. This is due to the small pressure difference which is immanent to the open radial co-flow design. Nonetheless, a certain degree of leakage will happen reducing effectively the provided fuel. The quantitative assessment of the influence, which cell fracture has on the performance is the topic of a subsequent study.

The fracture pattern consists predominantly of radial cracks which can be accompanied by secondary fracture around the central hole, as seen in Figure 1.2. Less often occurred cracks with a tangential orientation, which usually followed the gaps between the bar arrays of the anode flow-field structure until at some point turning sideways, running towards the outer edge of the cell. For the stacks operated for more than 4000 hours the leakage around some cracks might have caused structural changes in the anode which can be attributed to the local burning of the fuel leading to increased temperatures and concentration of water and oxygen which may oxidise the Nickel. This effect is usually more pronounced close to the outer circumference (increased water concentration due to the utilised fuel) especially above the air inlet channels where the maximum leakage rate is expected (see Figure 1.2)

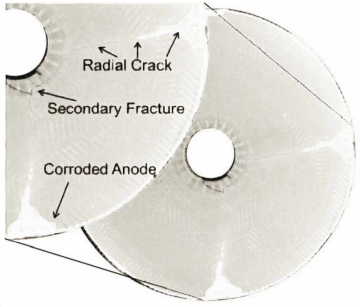

Figure 1.2: Anode side of a ruptured cell after 6700 h operation and two redox-cycles.

Fractography reveals that the majority of the cracks originate at distinct sites with respect to the MIC. These are the sealing planes on the cathode side at the air entrance and the area close to the central hole with the fuel inlet bars and the opposite fuel sealing plane (marked red in Figure 1.3). At the air inlet sealing planes, fracture always is associated with small bumps of the MIC coating on the cathode side (Figure 1.4a)) with a height typically between 10 - 60 µm compared to their direct surrounding. This leads to an uneven distribution of the mechanical pre-load and the stacks own weight (which reaches up to a quarter of the pre-load). These

bumps can occur randomly distributed over the whole MIC-structure. However, they coincide with fracture origin sites almost exclusively at the red marked areas in Figure 1.3.

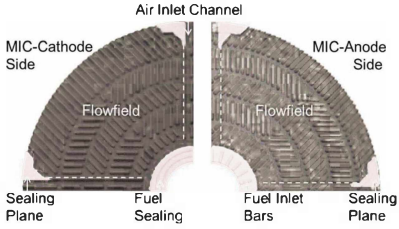

Figure 1.3: Cathode side (left) and anode side (right) MIC structure with the positions of the air inlet channels and the flow-fields. The areas where frequent cell fracture is initiated are marked red.

For stacks operated more than 4000 hours, cracks around the central hole become more frequent without being associated with bumps of the contact coating at the fuel sealing plane of the cathode side. Since no additional seal prevents the cathode from being exposed to the fuel flowing in the central hole, it will gradually be decomposed and lose its structural integrity, becoming a loose powder not able to support the cell at the fuel sealing plane, also leading to an undefined uneven distribution of the pre-load.

Just behind the inner sealing ring the leaked fuel burns off with the cathode air, which creates a narrow zone of 0.5-0.6 mm where the decomposed cathode reacts with the electrolyte forming a new porous layer leaving the electrolyte grooved (Figure 1.5). EDX indicates the formation of several different zirconate compounds like La_2ZrO_7 or $SrZrO_3$, which have been already observed for LSM based cathodes [12, 13]. Although the surface profile is significantly changed these grooves do not appear to be origins for fracture, but only preferential pathways for crack propagation.

In general the crack initiation sites exhibit always the same morphology as represented by Figure 1.4b) and c), showing a rough and jagged fracture surface

which is between 2-4 mm wide for radial cracks and can reach up to several centimetres for cracks starting with a tangential orientation. The fracture edge at the cathode side of the electrolyte is smooth, while the anode side shows rather a zigzag pattern. The ends of these zones are marked by an edge curved concavely towards the anode (see Figure 1.4c)), indicating that the crack extension did not proceed continuously but stopped, while changing the crack surface morphology after resuming propagation.

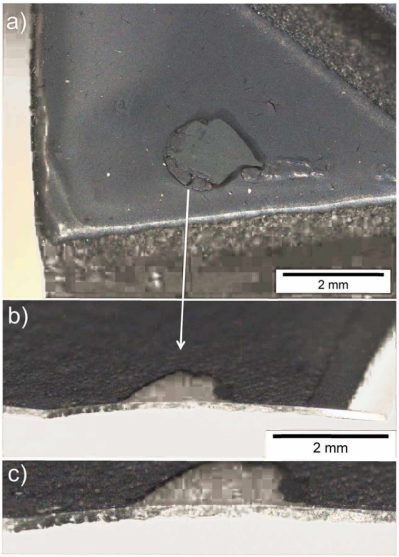

Figure 1.4: Crack origin at the cathode sealing plane at the air inlet channel with a) the associated bumps on the cathode side, b) the fracture surface of the cell from a tilted cathode side perspective with the delaminated cathode in the contact zone and c) the magnification of the fracture surface.

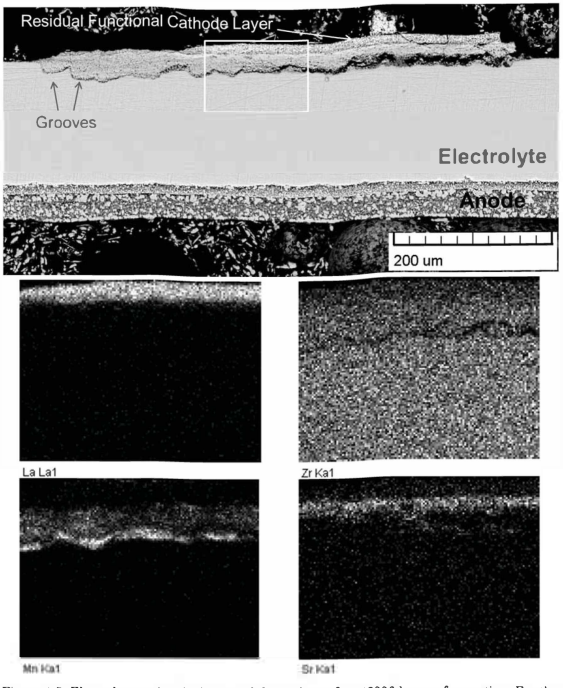

Figure 1.5: Electrolyte and cathode material reactions after 40000 hours of operation. For the marked section the EDX-element mappings of La, Zr, Mn and Sr are shown (30 kV acceleration voltage).

1.2.2 Mechanical Load Situation

(i) *Pre-load*: After being able to identify the location for crack initiation the question of the fracture mechanism and the involved stresses leading to macroscopic cell rupture arises. The most apparent source for mechanical stress acting on the cell is the pre-load of 390 N on the stack which results in a vertical average compression of σ_{prel} = 0.036 - 0.046 MPa considering the stacks own weight and assuming an even distribution. While these loads are very small, they might lead to significant stresses when distributed unevenly over the cell area. This is the case for the observed bumps on the cathode side which are associated with the crack origin sites. Here the pre-load is concentrated and a certain deflection, which is the height of the bumps, is impressed in the cell. Assuming the cell to be clamped between two MICs and being lifted and pressed into the Nickel mesh the resultant stresses can be estimated. The respective elastic model is taken from *Roark's Formulas for Stress and Strain* [14] and shown in Figure 1.6. This approach is just a rough image of the real load situation but can provide an upper limit of the occurring stresses, neglecting the stiffness of the Nickel mesh and a redistribution of the nominal pre-load. Since the maximum deflection y_{max} is given by the height of the bumps, it is possible to calculate the radius R for the lifted cell area. Taking the force F needed to bend the cell until the given deflection and comparing it with the nominal compressive stress $\sigma_{prel}$the system provides ($F = \sigma_{prel}\pi R^2$), R becomes:

$$R = \left(\frac{16\, D^* y_{max}}{\sigma_{prel}}\right)^{1/4} \tag{1.1}$$

where D^* is the effective plate constant at the operating temperature calculated according to *Hsueh* and *Luttrell* [15] using the values in Table 1.1 and assuming a Poisson's ratio of ν = 0.3 for all layers. The resulting maximum stress which arises in this situation for the electrolyte at its interface with the anode is plotted for varying y_{max} in Figure 1.7 also following the approach of *Hsueh* and *Luttrell*, with:

$$\sigma(y_{max}) = \frac{E_{El}\left(t_{C_1} + t_{C_2} + t_{El} - z_n^*\right)}{4\pi\,(1-\nu^2)D^*}\, F\,(1+\nu)\ln\frac{R}{r_0} \tag{1.2}$$

where z_n^* is the neutral bending plane of the multi-layer, E_{El} the electrolyte's Young's modulus and t_i the respective thickness of the two cathode layers and the electrolyte

and r_0 the contact radius. In order to assess the severity of these stresses the probability of failure is plotted as well using the Weibull equation [16]:

$$F\left(\sigma(y_{max}),\, S_{eff}\right) = 1 - \exp\left[-\frac{S_{eff}}{S_0}\left(\frac{\sigma(y_{max})}{\sigma_0}\right)^m\right] \tag{1.3}$$

and the material parameters given in Table 1.2. Since no fitting material data is available in the literature, double ring bending tests have been performed on samples 30 mm in diameter of bare 3YSZ and 6ScSZ electrolytes using the test rig and FE-model described in [17] for evaluating the stresses and effectively loaded surfaces S_0. Both sides of the electrolyte have been tested regarding their fracture stress at room temperature (RT) and a relative humidity of 37%, with a load rate so that the fracture time was between t_f = 10-15 s, showing that the side used for the anode layers is significantly weaker, since it is rougher than the cathode side. Since the roughness apparently determines the strength, the effectively loaded surface has to be taken into account rather than the effectively loaded sample volume. The rougher side of the 6ScSZ electrolyte has also been tested at elevated temperatures giving the Young's modulus and the fracture strength values in Table 1.1 and 1.2. Applying the values valid for T = 950°C for the operating temperature T = 850°C makes the estimation more conservative regarding the failure prediction, since the strength would rise by lowering the temperature.

Table 1.1: Layer thicknesses and Young's modulus for the different cell materials

	Cathode Current Collecting Layer	Cathode Functional Layer	Anode Current Collecting Layer	Anode Functional Layer	3YSZ-Electrolyte	6ScSZ-Electrolyte
Thickness (µm)	70	15	30	10	140	160
Young's-Modulus (GPa) at T=850°C	60*	40*	40*	60*	155*	140
Young's-Modulus (GPa) at RT	70*	80*	50*	65*	212	202
$\bar{\alpha}$ (25-1000°C) (10^{-6}/K)	11.00*	10.70*	12.50*	12.25*	10.90**	10.70**
ΔT after sintering (K)	1075	1075	1195	1195	-	-

*taken from *Kuebler* et al. [17]; **values according to the supplier

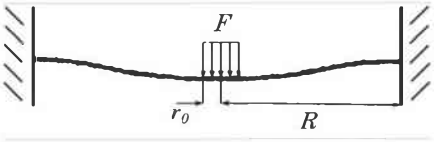

Figure 1.6: Elastic model for a circular plate being fixed at the outer edge at a radius R and loaded with an over a radius r_0 evenly distributed force F.

It becomes apparent that the estimated stresses will most certainly not lead to fracture. Only at elevated temperatures and relatively high deflections does 6ScSZ become slightly susceptible to fracture, however bumps higher than 60 μm are scarce and thus play a lesser role. At RT the plate stiffness increases. Since the deflection is constant this leads to an increased stress, which is overcompensated by an increase in strength diminishing the likelihood for failure to be always close to zero. Because the stress is local and deformation controlled, a possible fracture event would only lead to a local crack, since any crack extension would reduce its own driving force by giving the cell the chance to comply.

Table 1.2: Electrolyte Weibull parameters for the two different electrolyte materials.

	Characteristic Strength σ_0 (MPa) T=950°C	Characteristic Strength σ_0 (MPa) T=25°C	Weibull modulus m	Effective surface S_0 at T=950°C (mm²)	Effective surface S_0 at T=25°C (mm²)
3YSZ	350*	937	31	6.0	6.0
6ScSZ	250	701	19	14.5	11.3

*estimated using the relation $\sigma_0(25°C)/\sigma_0(950°C) \approx K_{Ic}(25°C)/K_{Ic}(950°C)$ with $K_{Ic}(T)$ being the mode I fracture toughness taken from [17]

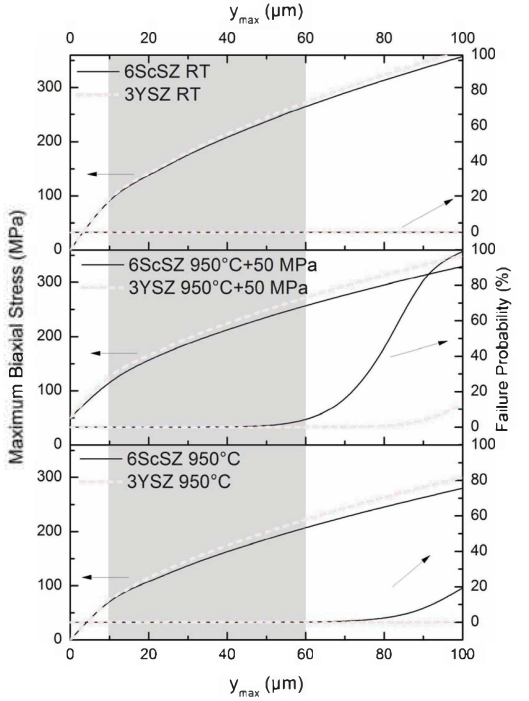

Figure 1.7: Maximum biaxial stress according to the elastic model shown in Figure 1.6 for a varying deflection y_{max}, σ_{pre} = 0.04 MPa, $S_{eff} = \pi r_0^2$, r_0 = 1 mm and with the respective failure probability for 3YSZ and 6ScSZ electrolytes. Bottom: for T = 950°C, middle: for T = 950°C adding 50 MPa to account for possible thermal stresses (see Figure 1.8), top: for room temperature; the shaded area marks the typical height of the bumps on the cathode side.

(ii) *Thermal stress*: During operation the conversion rate of the fuel and therefore the released heat decreases over the cell radius leading to an inhomogeneous lateral temperature distribution. A two-step numerical simulation of the repeat unit based on the model shown in Figure 1.8a) for a cell with 3YSZ electrolyte and the layer thicknesses of Table 1.1 has been performed employing the finite element software *NM-SESES* (*ZHAW-ICP*, Winterthur/Switzerland). First the temperature distribution for maximum power output (MPO) and open circuit (OC) conditions over the cell is calculated employing the numerical volume averaging method [18]. The condition, where the greatest power output is reached, represents the normal operating condition for the cell. When the stack is shut down the electrical circuit is opened before the fuel is turned off, leading for a short time to a new stationary temperature distribution represented by the OC-condition. In a second step the resulting thermal stresses are calculated linear elastically using the parameters in Table 1.1. The resulting maximum principle stresses within the electrolyte are shown in Figure 1.8b) and c). For the MPO- condition the electrolyte is at the outer circumference under tangential stress and slightly tangentially compressed at the inner cell area. Since the main part of the fuel is electrochemically converted at the inner cell area the temperature drops from the inside to the outside. In the case of an open circuit the whole fuel is burned off at the outer cell edge. Hence, the heat production takes place mainly at the outer edge of the cell creating a temperature gradient falling from the outside to the inside, resulting in a maximum stress which is of a tangential nature for the whole cell but also giving a positive radial component. For both conditions the peak mechanical loads are around 50 MPa appearing at the air entrance and at the inner cell edge in the case of MPO and OC, respectively.

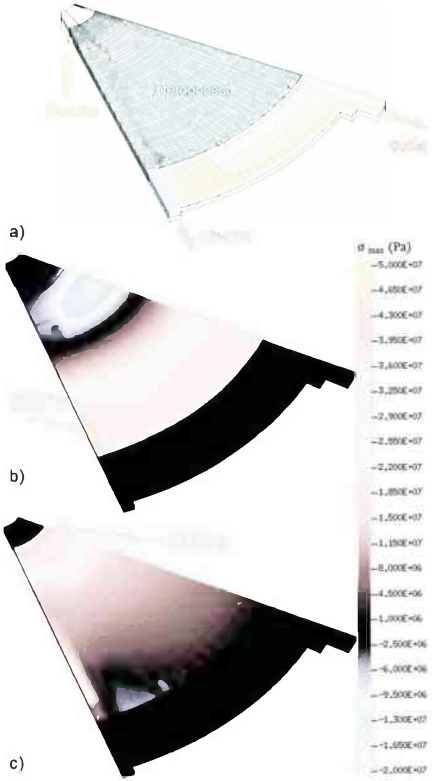

Figure 1.8: a) 3D thermo-mechanical-flow-model of ⅛th of the cell to obtain the temperature distribution within a single repeat-unit and to calculate the stresses caused by local temperature-gradients; b) maximum principal stresses of a cell mounted in a repeat-unit under MPO-conditions and c) under OC-conditions for a cell with 3YSZ electrolyte. The highest stresses are indicated in yellow, stress-free zones are shown in black and compressive stresses in blue and green.

It is possible to evaluate the failure potential of thermal stresses by calculating the mode I stress intensity factor K_I for a crack being introduced at either the inner or the outer edge of the electrolyte. Following the approach proposed by *Munz* and *Fett* [19], which was already applied to a similar problem by *Schneider* and *Danzer* [20], K_I is obtained by solving:

$$K_I = \int_0^a \sigma_\phi(x) h(a,x) dx \tag{1.4}$$

where $h(a,x)$ is the weight function weighing the stress perpendicular to the crack faces σ_ϕ along the crack length. The respective expression for an annular circular plate can be found in the table book of *Wu* and *Carlsson* [21] and reads:

$$h(x,a) = \frac{1}{\sqrt{2\pi a}} \sum_{i=1}^{n=3,4} \beta_i(a) \left(1 - \frac{x}{a}\right)^{i-\frac{3}{2}} \tag{1.5}$$

For internal cracks n becomes 3 and for external 4. The coefficients β_i are given in [21] for discrete values of crack length a to plate width W. Figure 1.9 presents the stress intensity factor solutions for an internal crack (inner edge) in the middle of the flow field (45°) for the open circuit operation and for external cracks being introduced either in the air inlet channel (0°) or in the middle of the flow-field (45°) for MPO.

Taking the toughness of the 3YSZ electrolyte to be between 1,75 and 2 MPa $m^{½}$ at T= 950°C [17] an initial crack has to be between 1-2 mm in order to get extended. If the crack is close to the edge but still has two ends as seen in Figure 1.4 this length might be roughly up to twice as long, since the stress is distributed over two crack edges. After this sub critical length the stress intensity remains above the toughness being able to extend the crack from one edge to the other. Therefore, thermal stresses can explain the occurrence of the radial fracture, which includes the vast majority of cracks. But in order to do so flaws within the millimetre range have to be introduced into the electrolyte.

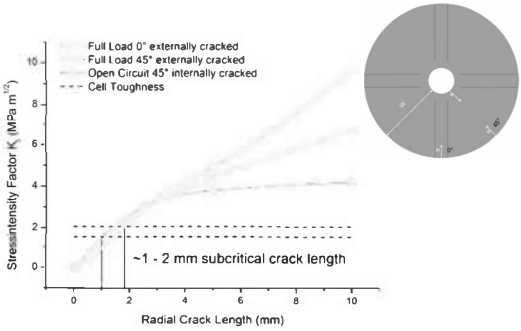

Figure 1.9: Stress intensity factor solutions at various angles and internal and external cracks (dots are spline interpolated).

(iii) *Residual stresses*: The five individual cell layers exhibit different thermal expansion coefficients, which cause thermal mismatch strains hence residual stresses after sintering and cooling upon room temperature. In order to assess these strains, strips of half cells have been prepared. These strips consist of a 160 μm thick 6ScSZ electrolyte and either the two cathode or anode layers. The dimensions were 95x10 mm^2. The cells were sintered while being constrained to be flat. After sintering the different thermal expansions lead to a curvature of the strip, which was measured using a camera. The curvature is then fitted by a circle to obtain its radius. Although the deflection was above the strip thickness, the sample showed no significant inhomogeneous bending. The single electrolyte remains flat even after annealing at the sinter temperature, thus the curvature can be attributed solely to thermal mismatch. When repeating the measurement of one sample, the method gives results with a reproducibility of ± 5%. It is not possible to determine the thermal mismatch strains and thus the residual stresses for all three layers of the half-cell just by measuring the radius of curvature. Therefore, the two electrode layers are considered as one. Compared to the electrolyte the Young's modulus of the electrode layers is similar and their thermal expansion coefficients are close to each other as well. Therefore assuming the electrodes to be one homogeneous layer will not influence the interpretation of the results.

For a bilayer the thermal mismatch strain $\varepsilon_{th} = \left(\overline{\alpha_1}(\Delta T) - \overline{\alpha_2}(\Delta T)\right)\Delta T$ is easily accessible following the elastic solutions of *Hsueh* and *Evans* [22], while applying a thickness weighed average Young's modulus and their combined thickness of the electrode layers. Figure 1.10a) shows the resulting biaxial stress in the electrode and the electrolyte obtained by applying the multi-layer solutions of *Hsueh* [23]. Additionally the nominal stresses which are to be expected according to the thermal expansion coefficients are presented. For comparison the radius of curvature for strips is calculated using the approach in [23], the data given in Table 1.1 and a ΔT which is the difference between RT and the respective sintering temperature. The stresses are then calculated as for the measured samples taking the two electrode layers as one. The residual stress for a cathode half-cell is relatively small and is close to what could be expected from the expansion mismatch. The deviation might be due to a lower effective temperature difference to the reference temperature (temperature with no residual stress) which is usually lower than the sintering temperature. The surface of the cathode after sintering shows a bubble-like morphology and small separate cracks which are characteristic for the cathode current collecting layer (see Figure 1.10c)). After etching and hence the removal of the LSM from the cathode the residual ceramic 8YSZ backbone of the former cermet structure of the functional cathode layer shows almost no defects.

The opposite is the case for the anode. After sintering the anode exhibits a completely developed channel crack network (see Figure 1.10b)). These channel cracks explain the large deviation from the measured stress and the nominal one, which is almost five times higher. That means that the anode cannot withstand the tension which emerges during cooling after the sintering. After being reduced the anode continues shrinking leading to a slightly increased stress level but leaving the crack pattern unchanged. The nominal compressive stress for the electrolyte at RT as part of a whole cell would be almost the sum of the single contributions of the electrodes being $\sigma_{El,nom} = -43$ MPa, while the measured stress would be $\sigma_{El,exp} = -15$ MPa. The residual stress reaches its maximum at RT while it almost vanishes at operating temperature. This becomes even more apparent when taking into account that the reference temperature is always somewhat lower than the sinter temperature and that the reference wanders towards the operating temperature due to creep.

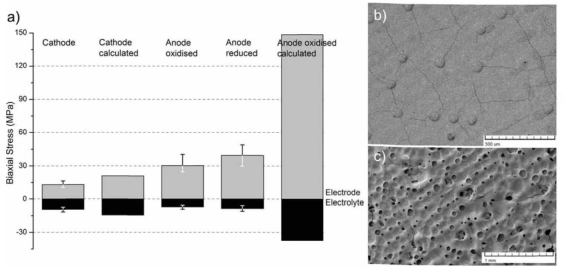

Figure 1.10: a) Residual stresses of cathode and anode half cells at RT from curvature measurements (error bars represent the sample spread) and the corresponding expected stresses based on the thermal expansion coefficients and according to values in Table 1.1; b) image of the anode and c) the cathode surface (BSE detector, 20 kV). The bubbles visible at the surfaces of the two electrode images are a consequence of the manufacturing process.

1.3 Discussion

Fractography reveals that the cell fracture happens in two steps. This is indicated by the two different morphologies of the fracture surface, which are clearly separated by distinct edges curved towards the anode (see Figure 1.11). At these edges the crack front comes to a halt. This is supported by the repeated observation of two of these pre-cracks in one extended crack. Underlining that the moment for the pre-crack formation is different from the one when the crack is being extended, otherwise there would be no chance for the development of a second pre-crack. It is obvious that the load which causes the pre-crack initiation is of local nature, while the cause for the overall crack extension has to be global. As already mentioned in Section 1.2.2, thermal stresses are fulfilling this requirement, as they are able to extend flaws in the range of several millimetres throughout the cell. This leads to the conclusion that the pre-crack has to form when the thermal stresses are absent or less pronounced. This is further supported by the fact that even a combination of the thermal stress peaks and the stresses introduced by the bumps on the cathode side are not sufficient to be the single cause for fracture, since the failure probabilities do not match with the observed damage, especially for the 3YSZ electrolyte (see Figure 1.7).

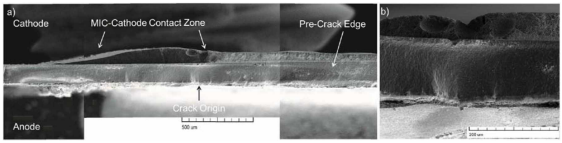

Figure 1.11: a) Pre-crack zone of a cell fractured at sealing plane at the air inlet; b) Magnified crack origin.

So far only the stresses at the electrolyte have been considered as causes for fracture. But it has been already shown that the strength of the electrolyte can be affected by the electrodes as well [9, 10]. Given a substrate which is coated with a more compliant layer, cracks in the layer reaching down to the interface may penetrate into the substrate until a certain depth following laterally the cracks of the coating. This is the case for the anode layers as seen in Figure 1.10. The elastic problem of coatings on relatively thick substrates being under residual stress due to thermal mismatch has been already developed by *Ye* and *Suo* [24] and reviewed by *Hutchinson* and *Suo* [25]. Depending on the elastic constants and the in plane stress and the thickness of the film, an expanding crack in the substrate being nucleated underneath a channel crack would have a positive energy release rate. The rate decreases with the depth. The substrate's toughness decides whether a crack propagates and how deep, but in any case the crack extension would be stable.

The situation for the electrolyte as part of the cell is somewhat different (see Ref. [25]). Because of its comparable thickness with respect to the electrodes it gets significantly compressed when the electrodes are under tension. Therefore the energy release rate for a substrate crack in the electrolyte is lowered if not negative. Hence it is no surprise that without an external mechanical load no damage to the electrolyte due to the highly stressed anode is observed. Nonetheless, if an external load is applied to the cell overcoming the compressive stress and increasing the overall energy release rate for an into the substrate expanding channel crack, the anode will then become the strength determining element of the cell. Figure 1.12 is a comparison between the fracture surfaces of an anode half-cell (electrolyte with only one electrode) with a 6ScSZ electrolyte flexed either with the anode side or the uncoated electrolyte side under tension. In the first case the morphology is jagged as for the pre-cracks in the actual ruptured cells (compare Figure 1.4). In the second

case, the electrolyte surface is smooth while the anode still displays a zigzag fracture line. The reason for this distinct behaviour of the anode is the fact that it is already greatly damaged, so that a global crack will follow the pre-existing channel cracks. If tension is applied on the anode, these cracks will be able to penetrate into the electrolyte imprinting the fracture path of the anode in the electrolyte. By comparing the morphology of Figure 1.12a) and 1.4 it becomes apparent that the crack origins for the observed pre-cracks are the pre-existing channel cracks of the anode.

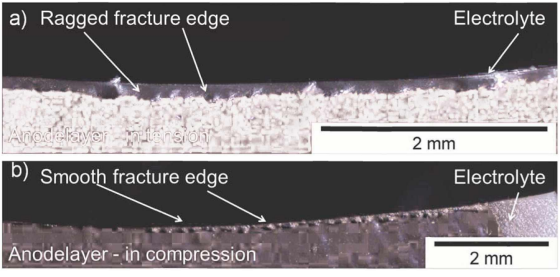

Figure 1.12: Fracture edges of an anode half-cell with a 6ScSZ electrolyte after being flexed with the anode being either a) in tension or b) under compression.

The driving force for the propagation of theses cracks into the electrolyte is given in any case by the inhomogeneous MIC-Cell contact (in the form of the bumps, the contact coating or the disintegration of the cathode at the fuel sealing plane) leading to multiple local stress peaks in the cell and the residual stress in the anode due to thermal mismatch. Both of these driving forces increase with decreasing temperature competing against the rising fracture toughness of the electrolyte, which gives a hint that the pre-cracks are formed during the cooling or the heating up of the stack. Additionally the electrolyte might exhibit a so called low thermal degradation (LTD). This is a phenomena characteristic to tetragonal stabilized zirconia like 3YSZ and 6ScSZ, where the strength severely suffers if the material is exposed to a humid media at temperatures between 150 and 400°C [26]. During cooling the stack needs several hours in order to reach RT, while residual moisture

might linger in the fine pore structure of the functional anode layer. Furthermore, the nickel of the anode undergoes a magnetic phase transition between 200 and 300°C so that the thermal expansion coefficient rises relatively steeply coming from high temperatures until it reaches a maximum at 240°C [27]. Hence, the residual stress will rise accordingly. LTD and this non-monotonic behaviour of thermal mismatch strain might crucially affect the failure probability and the formation of pre-cracks.

The explanation as for why the fracture origins for widely extended cracks are correlated with the stress peaks for the two presented operating conditions can now be given. Pre-cracks are probably formed throughout the whole cell since bumps on the cathode side are found for arbitrary sites at the MIC. The probability for these pre-cracks to propagate depends on the local thermal stress level, thus the stress peaks in Figure 1.8 correspond with the red areas in Figure 1.3, where crack origins were predominately found.

In order to prove these hypotheses it is necessary to measure the bi-axial bending strength of the cell over the whole temperature range in its oxidised state and for the operating temperature in its reduced one. Because the loads present are deformation controlled the critical strain of the electrolyte and the critical deflection of the whole cell should be taken into account in order to assess the susceptibility of the cell for fracture within the stack.

Furthermore, it remains unclear how the microstructural changes within the anode during operation, which have been reported by *Holzer* et al. for this anode material [28, 29], will affect the residual stresses. Additionally, for most of the Ni-based anode materials significant creep rates are to be expected at operating temperature [30]. Since all discussed sources for stress are deformation controlled, creep would simply relax crucial stresses and it would be therefore beneficial. However, the creep rate is mostly determined by the ceramic backbone which is with CGO different from the so far reported zirconia based ones. Hence, it is at this point not possible to consider possible creep effects.

1.4 Conclusion

Nine SOFC stacks of the *Galileo 1000 N* being operated at customers sites or at Hexis have been inspected post mortem. Each examined stack contained fractured cells. After a fractographical and fracture mechanical analysis it becomes apparent that for almost all of the cells fracture happens according to one distinct failure pattern. When mounted, the anode of the cells exhibits channel cracks as a consequence of the large thermal mismatch to the electrolyte. Due to the occurrence of bumps on the cathode side and the disintegration of the cathode at the fuel sealing around the central hole, the pre-load leads to local stress peaks loading predominantly the anode side of the cell. Along with residual stresses in the anode either due to thermal mismatch or the shrinkage due to the Ni-reduction, the anode's channel cracks are able to propagate into the electrolyte. Because the external stress for the cell is local and deformation controlled, a stable pre-crack forms in the electrolyte most likely when the stack is below the operating temperature, hence while it is either cooling down, heating up or idle at RT. Such a damaged cell will most likely rupture at places where thermal stresses are high. These sites are at the air entrance while the stack operates at MPO-conditions and around the central hole in the case of an OC. Pre-cracks might form in the whole cell but appear to be critical mostly at these areas.

Based on this failure analysis it is now possible to evaluate general and system specific design guidelines in order to reduce the cells failure probability, which will be part of a subsequent study.

1.5 Acknowledgments

The authors would like to thank *R. Bächtold, U. Weissen, B. Iwanschitz, D. Haberstock, R. Denzler* and *J.A. Schuler* for the priceless discussions and the unconditional support. Furthermore, the funding of this work by the *Swiss Federal Office of Energy* under the contract no. 8100076; SI/500084-02 and by *Swisselectric Research* within the *SOF-CH-ESC* project is gratefully acknowledged.

1.6 References

[1] M.Y. Gong, X.B. Liu, J. Trembly, C. Johnson, Journal of Power Sources, 168 (2007) 289-298.
[2] N. Shaigan, W. Qu, D.G. Ivey, W.X. Chen, Journal of Power Sources, 195 (2010) 1529-1542.
[3] M. Ettler, H. Timmermann, J. Malzbender, A. Weber, N.H. Menzler, Journal of Power Sources, 195 (2010) 5452-5467.
[4] H. Yokokawa, H. Tu, B. Iwanschitz, A. Mai, Journal of Power Sources, 182 (2008) 400-412.
[5] J. Malzbender, P. Batfalsky, R. Vaßen, V. Shemet, F. Tietz, Journal of Power Sources, 201 (2012) 196-203.
[6] J. Laurencin, G. Delette, F. Lefebvre-Joud, A. Dupeux, Journal of the European Ceramic Society, 28 (2008) 1857-1869.
[7] A. Atkinson, A. Selcuk, Acta Materialia, 47 (1998) 867-874.
[8] J. Malzbender, R.W. Steinbrech, Journal of the European Ceramic Society, 27 (2007) 2597-2603.
[9] A. Selcuk, A. Merere, A. Atkinson, Journal of Materials Science, 36 (2001) 1173-1182.
[10] B.F. Sorensen, S. Primdahl, Journal of Materials Science, 33 (1998) 5291-5300.
[11] A. Mai, B. Iwanschitz, U. Weissen, R. Denzler, D. Haberstock, V. Nerlich, A. Schuler, Status of Hexis' SOFC Stack Development and the Galileo 1000 N Micro-CHP System, in: S.C. Singhal, K. Eguchi (Eds.) Solid Oxide Fuel Cells 12, 2011, pp. 87-95.
[12] A. Hessler-Wyser, Z. Wuillemin, J.A. Schuler, A. Faes, J. Van Herle, Journal of Materials Science, 46 (2011) 4532-4539.
[13] M. Chen, Y.L. Liu, A. Hagen, P.V. Hendriksen, F.W. Poulsen, Fuel Cells, 9 (2009) 833-840.
[14] W.C. Young, R.G. Budynas, Roark's Formulas for Stress and Strain, 7th ed., MacGraw-Hill, New York, 2002.
[15] C.H. Hsueh, C.R. Luttrell, Compos. Sci. Technol., 67 (2007) 278-285.
[16] R. Danzer, T. Lube, P. Supancic, R. Damani, Advanced Engineering Materials, 10 (2008) 275-298.
[17] J. Kuebler, U.F. Vogt, D. Haberstock, J. Sfeir, A. Mai, T. Hocker, M. Roos, U. Harnisch, Fuel Cells, 10 (2010) 1066-1073.
[18] M. Roos, E. Batawi, U. Harnisch, T. Hocker, Journal of Power Sources, 118 (2003) 86-95.
[19] D. Munz, T. Fett, Ceramics, first ed., Springer, Berlin, 2001.
[20] G.A. Schneider, R. Danzer, Engineering Fracture Mechanics, 34 (1989) 547-552.
[21] X.R. Wu, A.J. Carlsson, Weight Functions and Stress Intensity Factor Solutions, first ed., Pergamon Press, Oxford, 1991.
[22] C.H. Hsueh, A.G. Evans, Journal of the American Ceramic Society, 68 (1985) 241-248.
[23] C.H. Hsueh, Thin Solid Films, 418 (2002) 182-188.

[24] T. Ye, Z. Suo, A.G. Evans, International Journal of Solids and Structures, 29 (1992) 2639-2648.
[25] J.W. Hutchinson, Z. Suo, Advances in Applied Mechanics, Vol 29, 29 (1992) 63-191.
[26] J. Chevalier, L. Gremillard, A.V. Virkar, D.R. Clarke, Journal of the American Ceramic Society, 92 (2009) 1901-1920.
[27] M. Mori, T. Yamamoto, H. Itoh, H. Inaba, H. Tagawa, Journal of The Electrochemical Society, 145 (1998) 1374.
[28] L. Holzer, B. Iwanschitz, T. Hocker, B. Münch, M. Prestat, D. Wiedenmann, U. Vogt, P. Holtappels, J. Sfeir, A. Mai, T. Graule, Journal of Power Sources, 196 (2011) 1279-1294.
[29] L. Holzer, B. Münch, B. Iwanschitz, M. Cantoni, T. Hocker, T. Graule, Journal of Power Sources, 196 (2011) 7076-7089.
[30] A. Nakajo, J. Kuebler, A. Faes, U.F. Vogt, H.J. Schindler, L.-K. Chiang, S. Modena, J. Van Herle, T. Hocker, Ceramics International, 38 (2012) 3907-3927.

Chapter 2

FRACTURE TOUGHNESS AND STRENGTH DISTRIBUTION AT ROOM TEMPERATURE OF ZIRCONIA TAPES USED FOR ELECTROLYTE SUPPORTED SOLID OXIDE FUEL CELLS

Journal of Power Sources 275 (2015) 217-226

Felix Fleischhauer[1,2], Mark Terner[3], Raul Bermejo[2], Robert Danzer[2], Andreas Mai[4], Thomas Graule[1], Jakob Kuebler[1]

[1]Empa, Swiss Federal Laboratories for Materials Science and Technology, Laboratory for High Performance Ceramics, Ueberlandstr. 129, 8600 Duebendorf, Switzerland

[2]Institut für Struktur-und Funktionskeramik, Montanuniversität Leoben, Peter-Tunner-Str. 5, 8700 Leoben, Austria

[3]ZHAW Zürich University of Applied Sciences, Institute of Materials and Process Engineering, CH-8401 Winterthur, Switzerland

[4]Hexis Ltd., Zum Park 5, 8404 Winterthur, Switzerland

Abstract

Zirconia tapes are established for the application as electrolytes in solid oxide fuel cells. One of their functional tasks is to provide the structural integrity of the cell. The mechanical failure of the electrolyte would cause leakage between the electrodes, leading to a reduction of the performance of a whole fuel cell stack. In order to assess the reliability of a certain zirconia tape with respect to a specific stress distribution and environment, the strength has to be properly characterised. In the present study a selection of several commercial highly ionic conductive scandia doped zirconia tapes was investigated regarding their strength under inert and humid conditions at room temperature, which required the determination of the elastic constants and the fracture toughness as well.

The strength of the different zirconia tapes ranks according to their fracture toughness, while the strength distributions typically exhibit a Weibull modulus of $m = 10$. It was found that all tapes suffer from sub critical crack growth, which leads to a limited lifetime at a given static load and a drastic reduction of the room temperature strength at time scales relevant for actual operation.

2.1 Introduction

The determination of the tensile strength is a crucial issue in order to predict the probability of rupture of a ceramic electrolyte used in solid oxide fuel cells (SOFC) since one of its main tasks is to physically separate fuel and air. The strength depends on two material specific features: (i) The flaw size and shape distribution within the materials volume or at the surface and (ii) its fracture toughness [1]. Both are first of all influenced by the material processing and handling but also later on by the exposure to a system specific environment, where mechanical stresses, elevated temperatures and contact with other compounds may alter these properties either instantaneously or with time. For instance sub critical crack growth (SCCG) [2-5] and cracks growing from the electrodes into the electrolyte [6, 7] in combination with an applied stress influence the critical flaw size distribution, whereas temperature itself changes the toughness. Ageing effects, which are diffusion controlled and thus time dependent processes, may also de- or increase the materials resistance towards fracture [8-10]. A sufficient understanding of these aspects is crucial to properly assess the suitability of a particular electrolyte for a specific system and cell type after its electrical and thermal properties have been found to be promising.

This study focuses on a detailed description of the strength distribution and hence the distribution of flaws of several commercially available electrolytes as well as subcritical crack growth at room temperature (RT). This provides the necessary foundations for the further description of the high temperature behaviour, ageing and the strength of electrolyte-electrode assemblies, which will be the topic of a subsequent article. Furthermore, electrolytes which are used as the structural backbone of SOFCs which are operated in so called µ-Combined-Heat-and-Power-Plants such as the *Galileo 1000 N* [11] are kept idle at RT depending on the heat demand for some time of the year. In a previous study it was found that in these systems significant stresses in the cell and the electrolyte can occur due to an irregular distributed clamping load, which is applied to create a tight lateral electrical contact [12]. Hence it is relevant to also assess the strength under these conditions.

The emphasis here lays on the characterization of scandia doped zirconia tapes, which are known for their high ionic conductivity [13] and 3 mol% yttria stabilized zirconia (3YSZ) as a reference material. A comprehensive overview of the available strength data of commercial and experimental tapes is given by *Nakajo* et al. [14] and includes different yttria stabilized zirconia and $Ce_xGd_yO_{2-\delta}$ compounds. For scandia stabilized zirconia two studies have been published addressing the strength of experimental 10Sc1CeSZ tapes [15] and of commercial 6ScSZ tapes [16]. The strength data published so far is somewhat difficult to compare and to interpret. The main problem is that brittle materials cannot be characterised by a single strength value but by a strength distribution, which is typically assumed to be of the Weibull type. This distribution however requires a set of three parameters to be defined [1], (i) the Weibull modulus, (ii) a size parameter, which is for thin sheets subjected to bending, as has been already pointed out by *Malzbender* et al. [16], the effectively loaded surface area, and (iii) the characteristic strength, which is the strength at which 63 % of the specimens fail. The latter value is bound to the corresponding Weibull modulus and the specific size parameter and without them meaningless.

The Weibull modulus and the characteristic strength are typically given, while the effectively loaded surface area is generally not mentioned (except for Ref. [16]). Hence, the strength distribution is not completely defined so that the published strength values have to be assessed with caution. Still, following trend is observable. Compared to 3YSZ all other materials with a superior conductivity appear to be mechanically less robust, which can be easily explained by the superior fracture toughness of 3YSZ. Furthermore, the Weibull modulus lies just between 4 and 9, which might be disastrous for achieving a high reliability and does not promote especially the application of the highly conductive compounds in electrolyte supported SOFCs. A high conductivity on the other hand is necessary to compete with anode supported SOFCs while providing enough robustness to ensure the long term structural integrity of the cell. Hence the motivation to characterise scandia doped zirconia tapes regarding their mechanical strength and lifetime in ambient environments and to assess their suitability.

2.2 Experimental

2.2.1 Material of study

The experimental investigation was performed on four different zirconia compounds, which were 3 mol% Y_2O_3 stabilized ZrO_2 (3YSZ), 6 mol% Sc_2O_3 stabilized ZrO_2 (6ScSZ), 6 mol% Sc_2O_3 and 1 mol% CeO_2 stabilized ZrO_2 (6Sc1CeSZ) and 10 mol% Sc_2O_3 and 1 mol% CeO_2 stabilized ZrO_2 (10Sc1CeSZ). The various ceramic tapes, which were mechanically tested in this study, were provided by the *Hexis AG* (Winterthur, Switzerland) and are commercially available. Based on the data of the manufactures the grain size (diameter *d*) of these compounds is $d_{50\%} = 0.1 - 0.2$ µm for 3YSZ, $d_{50\%} = 0.5 - 1$ µm for 6ScSZ, $d_{50\%} = 0.5 - 1$ µm for 6Sc1CeSZ and $d_{50\%} = 2 - 4$ µm for 10Sc1CeSZ.

Depth profile measurements were carried out for different tapes and their respective sides using a Leica DCM 3D confocal microscope with blue LED light. The roughness was calculated by taking the mean of the root mean squared of ten 15 mm long line scans choosing the devices smallest step size of 0.2 µm. Topographic images of different tapes and surfaces were obtained by mapping a 9 mm^2 squared area with the same step size to check for large flaws and the general surface morphology.

2.2.2 Elastic properties

The elastic constants of 3YSZ, 6ScSZ, 6Sc1CeSZ were measured using the Impulse-Excitation-Technique (IET) as described in [17]. As this method is not applicable to the mechanically tested tapes due to their in this regard too low thickness, rectangular plates (12x45x3.25 mm^3) were manufactured for the sole purpose of determining the elastic constants of these three compounds. The 6ScSZ and 6Sc1CeSZ samples were manufactured via uniaxial pressing and sintering (1580°C/2 h) from the same powder as was used for the respective tapes, while for 3YSZ a powder purchased from *Tosoh* (Tokyo, Japan) was used. The sample densities were determined via the dimensions and the weight and are greater than or equal to 98 % of the theoretical density. These thick plates are then either placed on a cross or two parallel bars in order to measure either their flexural or torsional frequencies in accordance with the EN 843-2 standard. The elastic constants are obtained from these frequencies following the approach of *Spinner* and *Tefft* [18].

2.2.3 Fracture toughness measurements

The fracture toughness was determined applying the Single-Edge-V-Notched Beam method (SEVNB). For this purpose discs of 6ScSZ (thickness: 160 µm), 3YSZ (140 µm), 6Sc1CeSZ (110 µm) and 10Sc1CeSZ (230µm) were cut into 5x50 mm² stripes, ten for each material. A V-notch was then cut by a razor blade coated with diamond paste into one of the longer edges of each sample. This procedure resulted in either a well-defined notch with a root radius between two to four micrometres (see Figure 2.1a)), in a notch with a pre-crack ahead of it (see Figure 2.1b)), or in complete failure. The samples which survived were then tested in a 3-Point-Bending setup as described in [19]. Each test was conducted in a dry nitrogen atmosphere applying a load-rate so that fracture occurred in less than ten seconds. The apparent toughness K_{Ic}^{*} is calculated for a support span width of B = 30 mm according to the *CEN TS 14425-5* standard and [20]:

$$K_{Ic}^{*} = \frac{F \cdot B}{t\sqrt{W}} \cdot \frac{3\sqrt{a/W}}{2} \cdot Y^{*} \tag{2.1}$$

with the dimensionless geometric factor:

$$Y^{*} = 1.9887 - 2.837\frac{a}{W} + 13.71\left(\frac{a}{W}\right)^{2} - 23.25\left(\frac{a}{W}\right)^{3} + 24.31\left(\frac{a}{W}\right)^{4} \tag{2.2}$$

where F is the fracture force, a is the depth of the notch or the combined depth of notch and maximum pre-crack length, W and t are the sample width and thickness, respectively.

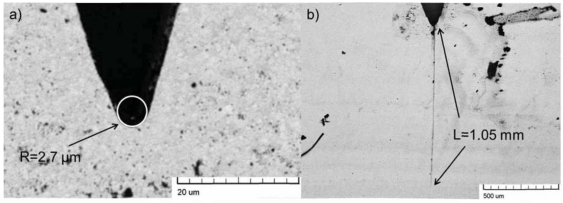

Figure 2.1: SEM micrograph of a) a notch root and b) a pre-crack underneath a notch of two 6Sc1CeSZ samples

2.2.4 Biaxial strength

The strength distributions of various tapes including different sides and thicknesses were measured performing either Ring-on-Ring (RoR) or Ball-on-3-Balls (B3B) bending tests. The sides possess a varying surface quality. The side of the tape which was cast on the support foil comes in two different ways. They are addressed as "smooth" if the ceramic tape was cast on a very smooth support foil or "rough" if a deliberately rough support foil was used. Compared to the smooth side the opposite side appeared rather dull and hence is called "dull".

2.2.4.1 Ring-on-Ring tests

For the RoR-tests the same setup as described in [19] was used with the support ring being 25 mm and the load ring 12.5 mm in diameter. To ensure that no significant SCCG might influence the results, all specimens were tested in a dry nitrogen atmosphere at room temperature (RT), which in general varied between 21 and 25°C. The load rate was chosen so that fracture occurred in less than 15 seconds. Discs of a diameter of 30 mm were obtained by laser cutting from 3YSZ (nominal thickness: 140 μm) and two 6ScSZ (nominal thickness: 160 μm) tapes, which were available either with a smooth and dull or with rough and dull surfaces. All the three different sides were tested independently.

The thickness of the tapes is relatively small compared to the dimensions of the test rig, so that the specimens fracture at large deflections. Hence the radial stress distribution has to be calculated by employing a rotationally symmetric 2D-finite-element-model (also described in [19]) to account for the strongly non-linear relationship between the applied load, the stress amplitude and the effectively loaded surface area, neglecting frictional effects. Apart from the geometry of the test rig and the load, the stress distribution strongly depends on the specimen thickness and its elastic constants. Therefore, the average thickness of every specimen was determined at five positions with accuracy of ± 0.5 μm and the elastic constants were taken from the respective IET measurements. Since the tangential stress component does not increase as much as the radial stress with increasing deflection as shown in Figure 2.2a), the first principle stress criterion (FPS) is chosen, which gives the maximum principle stress as the fracture strength. An evaluation between this

approach and the principle of independent action (PIA) [1], where all principle stresses are considered, results in no significant difference.

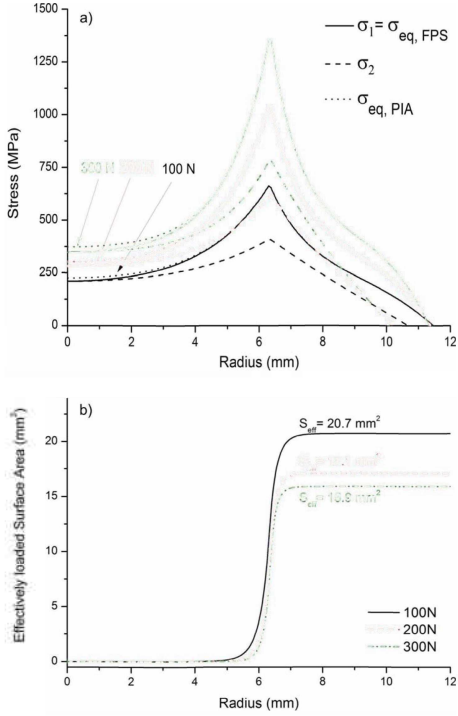

Figure 2.2: a) Stress distribution and b) the corresponding effective surface area for different applied loads considering a RoR test rig with 25 mm outer and 12.5 mm inner diameter loading a Ø30 mm and 160 μm thick 6ScSZ disc and assuming a Weibull modulus of m = 10.

The effectively loaded surface area S_{eff} is calculated according to:

$$S_{eff} = \int_0^{r^*} \left(\frac{\sigma_{eq}(r)}{\sigma_{eq,max}} \right)^m 2\pi\, r\, dr \tag{2.3}$$

where r is the radial position vector, r^* is the radius where σ_{eq}, the equivalent uniaxial stress, becomes negative. By choosing the FPS criterion σ_{eq} is equal to the maximum principle stress. Since the effective surface is decreasing with increasing deflection and load and thus not constant over a set of measured specimens, as depicted in Figure 2.2b), the value corresponding to the characteristic strength assuming a Weibull distribution is chosen.

An analysis of the effect of the change of the loaded surface area over a sample set of up to 100 specimens was performed for the applied RoR test geometry and the used samples. An example calculation is presented in Figure 2.3 for a 160 µm 6ScSZ tape, for different Weibull moduli and an assumed characteristic strength of 1100 MPa. In general, the decrease of the loaded area with the load and deflection results in a decreased apparent and hence measured Weibull modulus. For moduli close or greater to $m = 10$ this effect however becomes negligible and has not been taken into account, which makes the results more conservative from a reliability perspective.

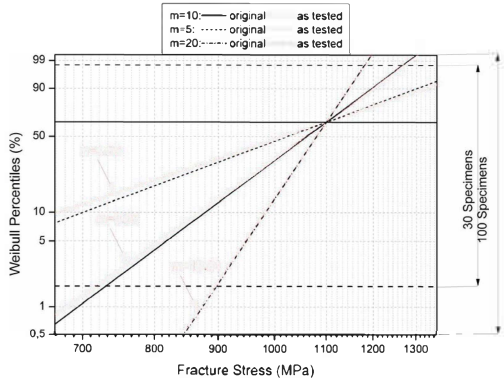

Figure 2.3: Original versus apparent strength distribution for the RoR-geometry employed in the present study assuming a 160 μm thick 6ScSZ tape with a characteristic strength of 1100 MPa and a Weibull modulus of either 5, 10 or 20.

2.2.4.2 Ball-on-three-Balls tests

B3B-tests were conducted on rectangular specimens as described in [21], since samples are easily available in large quantity by cutting ceramic tapes with a diamond wheel saw. The strength analysis of the B3B bending tests was based on the work of *Börger* et al. [22, 23], where the maximum principle stress σ_{max} is related to the fracture force F via:

$$\sigma_{max} = f\frac{F}{t^2} \tag{2.4}$$

t is the specimen thickness and f a dimensionless proportionality factor, which depends on the thickness, size and Poisson's ratio of the specimen and the diameter of the balls. This factor and the corresponding effective surface area (analogue to Equation (2.3)) were calculated for balls of three different sizes and for rectangular shaped specimens using the same finite element-model as in [21], taking into account the varying thicknesses and Poisson's ratios.

Since the model works within the confinements of linear plate theory, the maximum deflection of every specimen is limited to half of its thickness. Hence the balls radii of the used test rigs have to be adjusted to the thickness of the tested specimens. Therefore, balls with 1.2 mm diameter are used to test specimens as thin as 40 µm, 2.2 mm and 6 mm balls for thicknesses down to 100 µm and 140 µm, respectively. The B3B setup employing the 2.2 mm balls, which was used for most of the experiments, differs slightly from the one presented in [21]. Instead of having the load ball underneath the specimen and three support balls on top, the setup has been reversed as shown in Figure 2.4. This has just one single disadvantage: The fracture test cannot be performed in a free standing regime, where the support balls are still able to roll and thus to follow the specimens' deformation, leading to low friction. In a consecutive study however *Börger* et al. [23] showed that for fixed balls the systematic error is just less than 1%. On the other hand this setup allows performing measurements while a constant flow of a specific gas can be blown onto the surface which is subjected to tensile stress. The alignment for the ruby support balls was manufactured from stainless steel. Steel and ruby are well known for their very low coefficient of friction, which decreases the frictional error due to the non-free standing test regime to a minimum.

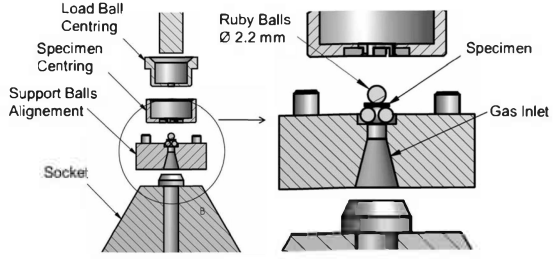

Figure 2.4: Ball-on-three-Balls multi atmosphere test rig for 4x3 mm² sized zirconia specimens.

2.3 Results

2.3.1 Fracture toughness

The fracture toughness is a crucial parameter, which reflects a materials resistance towards fracture and is indispensable for life time calculation where SCCG is involved. It is also a parameter which depends on the manufacturing process and thus should be directly measured using the same samples, which are of further interest. This is a relative difficult task considering the generally low thickness, so among the possibilities the SEVNB-method was found to be the most promising one. Figure 2.5 shows the results of the SEVNB-experiments, where the fracture toughness for 6Sc1CeSZ and 10Sc1CeSZ was calculated from the pre-cracked specimens resulting in $K_{Ic,6Sc1CeSZ} = 3.7 \pm 0.1$ MPa $m^{½}$ and $K_{Ic,10Sc1CeSZ} = 1.84 \pm 0.2$ MPa $m^{½}$, respectively. It is known that a critical notch root radius has to be reached, which is in the range of a characteristic material dependent flaw size [24], in order to measure the true fracture toughness. Therefore, the apparent toughness $K_{Ic,app}$ is plotted against the notch root radius to assess the results. A comparison between the $K_{Ic,app}$ obtained for the pre-cracked and notched samples of 10Sc1CeSZ and 6Sc1CeSZ shows that the notches are not sufficiently sharp enough to be equivalent to sharp edged cracks. Following the approach of ***Fett*** [25] the characteristic flaw size a can be determined by fitting the following implicit function:

$$\frac{K_{Ic}}{K_{Ic,app}} = tanh\left(2.24\left(\frac{2}{3} + 0.178\left(1 - exp\left(-\frac{1.64\,a}{R}\right)\right)\right)\sqrt{\frac{a}{R}}\right) \tag{2.5}$$

where K_{Ic} is the true fracture toughness and R is the notch root radius. For 6Sc1CeSZ and 10Sc1CeSZ this gives flaw sizes of $a_{6Sc1CeSZ} = 0.80$ µm and $a_{10Sc1CeSZ} = 0.84$ µm. If the fracture toughness of 3YSZ (identical material compared to the one used in this study) is taken from [19] with $K_{Ic,3YSZ} = 5.0$ MPa $m^{½}$ and the same procedure is performed, a value of $a_{3YSZ} = 0.83$ µm is obtained. These values differ remarkably little from one another, despite stemming from different zirconia compositions. By applying Equation (2.5) with the mean characteristic flaw size of the values above, the true fracture toughness of 6ScSZ has been determined to be $K_{Ic,6ScSZ} = 4.1 \pm 0.25$ MPa $m^{½}$ where the error is given by taking the sample spread and the lower and upper values found for a into account (also shown in Figure 2.5).

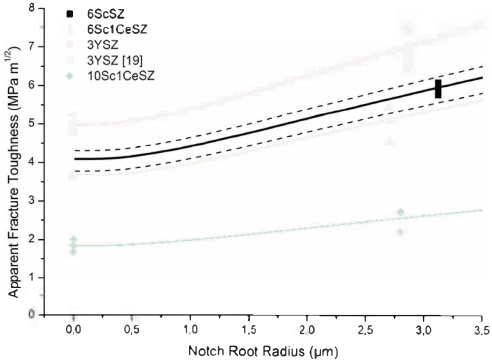

Figure 2.5: Apparent fracture toughness against notch root radius including room temperature fracture toughness for 3YSZ taken from [19] and fit functions according to Equation (2.5).

2.3.2 Inert Strength under biaxial bending

It is an inherent property of brittle materials that their strength scatters, following typically a Weibull distribution. In order to characterize such a material, this distribution has to be determined, so that the failure probability or the corresponding reliability for a given load situation can be calculated. In order to compare different materials the test conditions have to be equivalent. SCCG usually affects the strength values in the presence of humidity, which is basically the case for normal laboratory conditions. This effect depends on the material itself as well as on load rate, initial flaw sizes and the level of humidity. While the level of humidity and the load rate can be controlled, the initial flaw sizes and the material specific humidity sensitivity are typically unknown. Therefore only inert conditions guarantee comparability, which for zirconia means practically to ensure the absence of significant humidity. In the present study all (if not indicated differently) strength tests were conducted either under dry argon or nitrogen atmospheres. The elastic constants needed for the stress calculation are presented in Table 2.1.

Table 2.1: Material parameters including standard deviation and the fracture toughness including the sample spread of the tested Zirconia compounds. The Poisson's Ratio ν was calculated from the shear (G) and the Young's modulus (E) according to $\nu = E/2G - 1$. Values of 10Sc1CeSZ are taken from [26].

Material/ Parameter	3YSZ	6ScSZ	6Sc1CeSZ	10Sc1CeSZ
E (GPa)	214.3 (±0.1)	213.6 (±1.5)	209.5 (±0.1)	204.6
G (GPa)	81.6 (±0.1)	80.8 (±0.1)	79.7 (±0.1)	76.1
ν	0.314 (±0.002)	0.321 (±0.005)	0.314 (±0.001)	0.345
K_{Ic} (MPa m$^{\frac{1}{2}}$)	5.0* (±0.24)	4.1 (±0.25)	3.7 (±0.1)	1.8 (±0.17)

*taken from [19]

The results were analysed according to the Weibull theory [1]. The parameters such as the characteristic strength σ_0 and the Weibull modulus m of the Weibull distribution:

$$P = 1 - exp\left(-\frac{S}{S_{eff}}\left(\frac{\sigma}{\sigma_0}\right)^m\right) \tag{2.6}$$

are determined by the maximum-likelihood-method [27]. The Weibull modulus m describes the scatter of the strength data, while the characteristic strength σ_0 is the stress at which the failure probability is: $P(\sigma_0, S_{eff}) = 1 - e^{-1} \approx 63\%$. A compilation of the Weibull parameters including S_{eff} of all tested materials, tapes and their respective sides is given in Table 2.2. Each measurement of a sample set results in a different S_{eff}, since it depends next to the geometry of the test rig on the thickness and the Poisson's ratio of the specimens and the Weibull modulus. Hence the median strength is plotted for comparative purposes as a function of S according to:

$$\sigma_{P=50\%}(S) = \sigma_{P=50\%}(S = S_{eff}) \sqrt[m]{\left(\frac{S_{eff}}{S}\right)} \tag{2.7}$$

(which follows directly from Equation (2.6)) and is shown in Figure 2.6.

The dashed lines represent the extrapolation according to Equation (2.7). The lines are continuous if for several single values a common Weibull modulus is found fitting the single measurements while being within the 90% confidence interval of each measurement. The values obtained are shown for 3YSZ and 6ScSZ both for the rough and the dull sides.

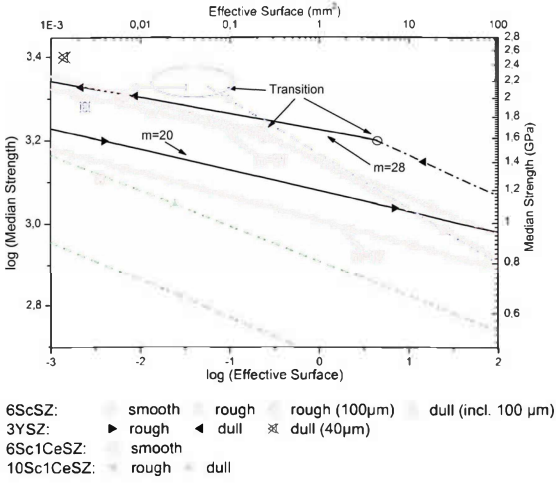

Figure 2.6: Strength data of Table 2.2 plotted against the loaded surface area. The dashed lines represent the extrapolation according to Equation (2.7). The lines are solid if for several single values a common Weibull modulus is found fitting the single measurements while being within the 90% confidence interval of each measurement. The values obtained are shown for 3YSZ and 6ScSZ both for the rough and the dull sides.

Table 2.2: Room temperature inert strength parameters and roughness for all tested materials, tape sides, thicknesses and specimen sizes. For σ_0 and m the 90% confidence intervals and for the roughness the standard deviations are given in the brackets.

Material /Side	Roughness R_{rms} (µm)	Sample set size	Thick-ness d (µm)	Specimen size (mm)**	Characteristic strength σ_0 (MPa)	Median strength $\sigma_{50\%}$ (MPa)	Weibull modulus m	Effective surface S_{eff} (mm²)
10Sc1CeSZ/ dull	0.18 (0.006)	30	230	4x3	1136 (1168|1106)	1112	12 (15.0|9.2)	2.5E-02
10Sc1CeSZ/ rough	0.8 (0.04)	30	230	4x3	679 (700|659)	665	11 (13.8|8.5)	2.8E-02
10Sc1CeSZ/ smooth	-	23	160	10x10	1230 (1337|1133)	1241	4.5 (5.9|3.4)	2.2E-01
3YSZ / dull	0.173 (0.006)	29	140	4x3	2162 (2188|2149)	2149	28 (35.7|21.7)	2.2E-03
		34	140	10x10	2056 (2083|2010)	2047	23 (29.4|18.7)	8.8E-03
		14	140	ø 30	1433 (1501|1369)	1407	10 (15.0|7.2)	1.5E+01
3YSZ / dull *	-	32	40	2x2	2544 (2611|2479)	2506	12 (15.1|9.5)	1.4E-03
3YSZ / rough	1.22 (0.06)	29	140	4x3	1634 (1661|1607)	1595	20 (25.7|15.6)	4.0E-03
		15	140	ø 30	1099 (1119|1079)	1089	26 (36.7|18.0)	6.9E+00
6Sc1CeSZ / smooth	0.08 (0.03)	102	110	4x3		2121		
		28	110	10x10	2066 (2158|1978)	1989	8 (9.9|5.9)	9.7E-02
6Sc1CeSZ / dull	0.09 (0.01)	30	110	4x3	1975 (2007|1944)	1929	20 (26.0|16.0)	2.4E-03
6ScSZ / dull	0.13 (0.003)	30	160	4x3	2017 (2050|1985)	1989	20 (25.3|15.5)	5.5E-03
		19	160	10x10	1863 (1894|1832)	1836	24 (33.3|17.8)	1.4E-02
		44	160	ø 30	1126 (1153|1100)	1097	11 (13.6|9.2)	1.8E+01
	0.2 (0.05)	30	100	4x3	2072 (2107|2037)	2018	19 (24.1|14.8)	2.0E-03
6ScSZ / rough	0.9 (0.006)	30	160	4x3	1379 (1404|1354)	1360	18 (22.4|13.8)	6.7E-03
		27	160	ø 30	909 (923|894)	885	21 (27.1|16.2)	1.1E+01
	1.1 (0.05)	30	100	4x3	1327 (1359|1297)	1284	14 (17.7|10.9)	3.6E-03
6ScSZ / smooth	0.041 (0.004)	19	160	4x3	2129 (2179|2081)	2056	18 (24.2|12.9)	6.7E-03
		30	160	ø 30	987 (1024|951)	969	9 (11.2|6.9)	2.5E+01

* measured under laboratory air conditions (relative humidity: 42%, load rate: 250 MPa/s)

**samples with diameter 30 mm were tested with the RoR all other with B3B set-up

By comparing different sides (dull, smooth and rough) of the investigated tapes it becomes obvious that the strength is strongly affected by the surface roughness, so that for small S a general trend is found where the strength decreases with the roughness. Hence the smooth and the dull tape sides have superior strength than the rough sides. Except for 10Sc1CeSZ this is also accompanied by relatively large values of the Weibull modulus. However this overall trend appears to be valid only for small loaded areas, since for 6ScSZ (dull and smooth), 6Sc1CeSZ (smooth) and 3YSZ (dull) a transition towards lower moduli occurs coming to larger loaded areas. For 6Sc1CeSZ this transition can even be recognised within a single sample set as shown in Figure 2.7. The high strength samples follow a much steeper trend and thus higher Weibull modulus ($m \sim 20$) than the low strength ones ($m \sim 5.5$). The modulus was roughly estimated, by fitting the 30 weakest and the 30 strongest samples, being aware that a proper analysis would require the assignment of every specimen to one distribution or the other by fractographical means. Since the overall sample set does not follow a single distribution it is futile to assign the typical Weibull parameters.

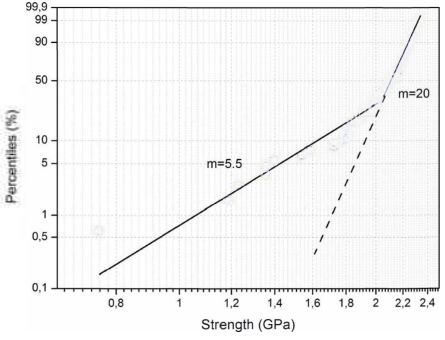

Figure 2.7: Weibull plot of 102 specimens (4x3 mm²) of 6Sc1CeSZ loaded at their smooth side with B3B test.

The limits of S_{eff} however have to correspond to the lower and upper Weibull modulus and are given in Figure 2.6. For the rough sides of 3YSZ and 6ScSZ such a transition is not found for the experimentally covered range of S, so that these samples retain their high modulus at large effective surfaces but at the cost of having a much lower strength to begin with. The low Weibull modulus of the smooth and dull 10Sc1CeSZ samples is interpreted such that the transition would occur at smaller tested surface areas. The transition presented here has also been found to occur for silicon-nitride samples tested over a wide range of S, where the high strength values are accompanied by a relatively high Weibull modulus too, which was reported by *Danzer* et al. [21].

Considering the four different zirconia compounds, 10Sc1CeSZ in general possesses the lowest strength, followed by 6Sc1CeSZ and 6ScSZ, while 3YSZ proves to be the strongest material. This ranking is in qualitative agreement with the fracture toughness values (see Table 2.1), with respect to similar surfaces and tape sides. Only the strength of the smooth 6Sc1CeSZ is slightly higher than the respective 6ScSZ side.

2.3.3 Effect of thickness on the strength

The ionic sheet resistance of zirconia electrolytes is of utmost importance. One easy way to keep this value to a minimum is to manufacture thinner tapes, which led to the development of tapes as thick as 40 µm. One question is whether these tapes maintain their strength compared to thicker ones. For this purpose a 6ScSZ tape with 100 µm and a 3YSZ tape with 40 µm have been tested using only the B3B-test, since it becomes more and more challenging to apply methods such as the RoR-test, which cannot be much miniaturised without increasing significantly measurement uncertainties (e.g. increasing deflection, increasing friction). The B3B becomes a good candidate to measure the bending strength of very thin specimens with low measurement uncertainties, which may affect the estimation of the Weibull parameters [28]. However with the thickness also the effectively loaded area S_{eff} is necessarily decreasing and so the extrapolation to application-relevant surface areas gets even more uncertain. This is because of the limited knowledge of the true Weibull modulus and secondly because of the possible change of the strength governing distribution as discussed above. For the dull side of the 100 µm 6ScSZ

tape it is possible to assume the same behaviour as for the dull side of the respective tape with 160 µm thickness, since its strength fits very well. The same on the other hand does not hold for the rough side. Having a similar roughness, its strength and Weibull modulus are significantly lower than the thicker reference tape. Also the dull side of the 40 µm 3YSZ tape has a much lower Weibull modulus than the tapes with 140 µm. The strength however is distinctively higher although it was measured in a humid environment. This makes it difficult to assess whether its inert strength extrapolated to surface areas larger than 1 mm^2 is comparable. Concluding the above made observations, it is not without further information save to adopt strength data of thicker tapes for the design and layout considerations of thinner ones.

2.3.4 Fractography

Fractography reveals that the low strength of the rough tape sides is a direct consequence of the surface morphology as shown in Figure 2.8. It is characterised by deep holes, which are interpreted as pores, originating from trapped air bubbles, where the largest act as fracture origins as seen in Figure 2.9a). For the high strength smooth and dull tested tape surfaces no fracture origins could be identified anymore, leading to the assumption that small grooves at the grain boundaries or slightly larger grains lead to failure. The lower strength is determined by surficial pores probably formed by air bubbles, which were trapped between the cast tape and the support foil (Figure 2.9b)), agglomerates (Figure 2.9c)) and inclusions (Figure 2.9d)). The transition in Weibull modulus thus follows from the relative scarcity of these three latter flaw types. For some tapes the B3B test loads such a small surface areas that it is simply too improbable to find one of these flaws, so that more frequent smaller micro-structural features become strength determining. For the rough tape sides the small pores cover the whole surface, which is why also a test loading small surface areas can measure the underlying distribution.

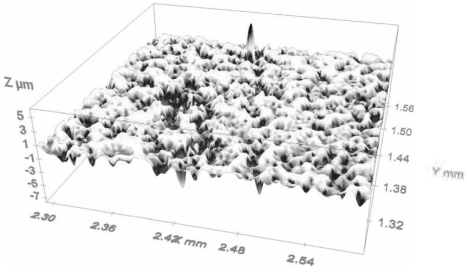

Figure 2.8: Surface morphology of the rough side of a 6ScSZ (160µm) tape.

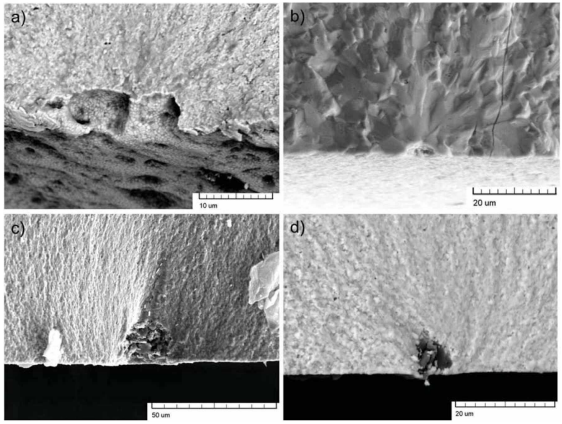

Figure 2.9: Examples of fracture origins of a) 6ScSZ (160 µm) rough side, b) 10Sc1CeSZ (230 µm) dull side, c) 6Sc1CeSZ (110 µm) smooth and d) 6Sc1CeSZ (110 µm) dull.

2.3.5 Effect of environment (humidity) on strength: subcritical crack growth

Since the perspective lifetime of a fuel cell is targeted to be seven years or more, while being subjected to humid environments on both sides, this strength lowering time dependent and life time determining effect has to be measured. The time dependent strength in ceramics is explained by a sub critical crack growth (SCCG) mechanism, which is a common weakening mechanism for ceramic materials, where a stressed flaw grows stably under applied stress, while being typically in contact with humid air, until reaching a certain size (critical size) which then causes instant fracture [29, 30]. This growth might lower the strength on short, but most importantly on large, time scales. Typically SCCG is described via the crack growth velocity da/dt of a crack or a flaw with the size a, which follows a Paris law in the form of:

$$\frac{da}{dt} = v_0 \left(\frac{K_{app}}{K_{Ic}}\right)^n \tag{2.8}$$

where v_0 is the crack growth rate when the applied stress intensity factor K_{app} reaches the fracture toughness K_{Ic}. n is the so called crack growth exponent, which is the lower the more sensitive a material is to moisture. Following the definition of the stress intensity factor, K_{app} does not just depend on the applied stress σ_{app} but also on the crack size a [31]:

$$K_{app} = \sigma_{app} Y \sqrt{\pi a} \tag{2.9}$$

with Y being the geometry factor of the crack. Hence, K_{app} even grows at a constant applied stress, so that the crack growth rate accelerates itself. In order to describe this phenomenon the two parameters v_0 and n have to be determined for a defined temperature and humidity. By inserting Equation (2.9) in Equation (2.8) a differential equation is obtained, where for an applied stress, which rises constantly with the load rate $\dot{\sigma}$, the following expression can be derived [1]:

$$\log \sigma_{app}(t_f) = \log \sigma_f = \frac{1}{n+1} \log \dot{\sigma} + \frac{1}{n+1} \log \left(\frac{2 K_{Ic}^2 (n+1)}{v_0 \pi Y^2 (n-2)} \sigma_{inert}^{(n-2)} \right) \tag{2.10}$$

with σ_{inert} being the inert strength in the absence of the SCCG effect and σ_f the fracture stress at the time of fracture t_f. By measuring the strength as function of the load rate, it is now possible to determine the crack growth parameters for a

specific level of humidity and temperature, while using the fracture toughness values given in Table 2.1.

Figure 2.10 depicts the results of these experiments, which were conducted for 4x3 mm² specimens applying the B3B test, while for 6ScSZ, 3YSZ and 10Sc1CeSZ the rough and for 6Sc1CeSZ the dull sides were loaded. Each plotted point σ_0^* represents the average between 12 and 18 specimens and is calculated applying following relation [32]:

$$\sigma_0^* = \sqrt[m^*]{\frac{1}{N}\sum_{1}^{N}\sigma_i^{m^*}} \qquad (2.11)$$

with

$$m^* = \frac{m(n+1)}{(n-2)}$$

where m^* is the corrected Weibull modulus, taking into account that if SCCG occurs the original distribution with the Weibull modulus m gets narrower, since smaller flaws grow relatively faster than larger ones [33]. n and v_0 are obtained by linear regression of the logarithmic strength versus the logarithmic load rate applying Equation (2.10) and a geometric factor $Y = 0.85$ for semi-elliptical surface cracks [34]. The SCCG corrected modulus is obtained by using the original Weibull modulus in Equation (2.11), to determine a preliminary value for the crack growth exponent. Recalculating the characteristic strength with the corrected Weibull modulus gives then the final n and v_0 [32].

The room temperature crack growth parameters are listed in Table 2.3. In general, all the tested zirconia materials are sensitive to moisture regarding their strength. This underlines first of all the importance of measuring the inert strength, since already at large load rates a drastic decrease in strength of up to a 75% was measured. Secondly, it is shown that the humidity level of the surrounding medium affects the lifetime of these zirconia materials. The level of humidity is hereby just shifting the respective curves towards lower strength, while the exponent remains approximately constant.

Table 2.3: Crack growth paramerter at $T = 22°C$ for different zirconia compounds measured in humid air (relative humidity given in the brackets) or dcionised water.

Material	6Sc1CeSZ	10Sc1CeSZ	6ScSZ		3YSZ	
Medium	Water	Air (92%)	Air (40%)	Water	Air (92%)	Air (32%)
n	65	37	54	56	55	54
v_0 (m/s)	4 E+02	4 E-03	9 E-01	9 E+00	9 E-02	3 E-02

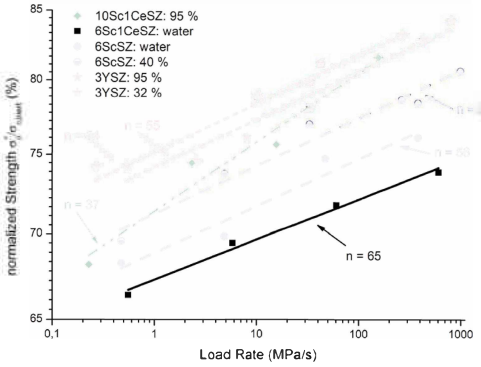

Figure 2.10: Humidity influenced characteristic strength normalised to the respective inert characteristic strength for various load rates, different zirconia compounds and humidity levels.

Compared to already published crack growth exponents, the one presented in Table 2.3 appear to be relatively large, which means that they indicate a lower sensitivity to humidity. For 3YSZ exponents between 19 and 31.5 [5, 35] and for 8YSZ values between 19 and 21.5 [36] have been reported. However, in these studies the crack growth was investigated on artificially introduced long cracks applying the double torsion technique. It has been pointed out, that a R-curve behaviour (rise of

the fracture toughness as a crack propagates) can influence the effectively measured SCCG parameter, so that it appears less sensitive to humidity [31]. For zirconia such a rise of the fracture resistance has been reported to appear as a crack grows its first 10 μm [37] running then in a plateau. The approach presented here tests small flaws and hence is affected by this R-curve effect. However it presents more reliable data on how the material actually behaves in a real load situation, since the behaviour of the strength determining flaws is tested directly.

2.4 Discussion

From a reliability perspective it is important to identify the largest flaws within a specimen's volume or at its surface and their underlying distribution. From this follows the requirement to apply a test set-up which loads relatively large surface areas, as the extrapolation towards greater surface areas becomes more and more uncertain the further it goes. This reveals the greatest disadvantage of the B3B bending test. Although it provides a high accuracy, while easily large sample sets can be tested, the tested sample surface is too small to predict the strength for large areas and low failure probabilities. Apart from this general aspect, it was found that the strength distribution might change for different tested surface areas, as can be seen for the smooth and dull sides of 6ScSZ and 3YSZ. This leads to the conclusion that the RoR test is the most suited in order to determine the strength distribution relevant for a reliability assessment.

Based on the measured material data, i.e. inert strength, toughness and the SCCG parameters, lifetime predictions can be made for a given material. As an example, the design stress σ_{stat}, to guarantee a certain probability of failure P_f over a certain time t_f, for a given zirconia tape can be described as:

$$\sigma_{stat}(S, P_f, t_f) = \left(\frac{{K_{Ic}}^2 \left(\frac{S_{eff}}{S} {\sigma_0}^m \ln\left(\frac{1}{1-P_f}\right) \right)^{\frac{n-2}{m}}}{v_0 \, t_f \, \pi \, Y^2 \left(\frac{n}{2}-1\right)} \right)^{1/n} \tag{2.12}$$

which is a function of the considered loaded surface area. A fuel cell has typically a surface area on one side between 100 and 250 cm², of which only a minor fraction is loaded [12]. Hence for further consideration a loaded area of 10 cm² is assumed while

a failure probability of 1:10,000 is taken. This is supposed to reflect the requirements of electrolytes as part of solid oxide fuel cells. The respective strength, which can be interpreted as a design stress, is plotted against the lifetime for a selection of tapes and their respective sides in Figure 2.11.

Comparing the inert strength with the characteristic strength values given in Table 2.2, it becomes clear how drastic the strength decreases, if realistic failure probabilities and loaded surface areas are assumed. This decrease mainly depends on the Weibull modulus of the strength distribution and is illustrated when extrapolating the characteristic strength of the smooth side of the 160 µm thick 10Sc1CeSZ tape. Here the measured characteristic strength of more than 1 GPa is reduced down to 33 MPa. This reveals that tapes with a Weibull modulus as low as $m = 5$ are practically of no use due to their unreliability.

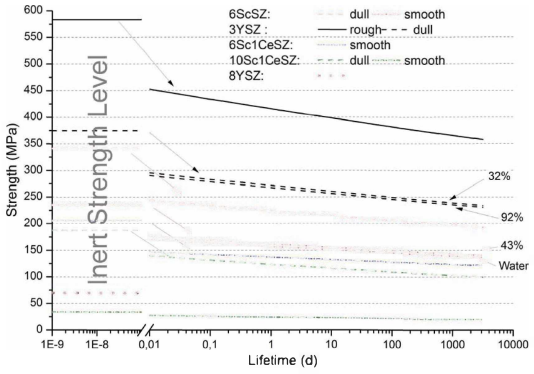

Figure 2.11: Strength-lifetime plot for different zirconia tapes and their respective surfaces following Equation (2.12) and the data given in Table 2.2 and 2.3 including the respective inert strength level assuming $P = 0.0001$ and $S = 10\text{cm}^2$. For the dull side of 3YSZ and the smooth one of 6ScSZ the strength for both measured humidity levels is displayed. The corresponding strength level of 8YSZ disregarding SCCG is included and taken from [38].

The importance of the Weibull modulus is further highlighted as the originally weaker rough side of 3YSZ (see Figure 2.6) becomes stronger than the dull side due to its larger modulus. Judging from the fractography however, it is doubtful that this reflects the true behaviour. For the smooth and dull sides, near surface volume flaws are strength determining, whereas for the rough sides the surface itself limits the strength. This involves less scatter in the latter, but leads to a lower strength. There is no reason that near surface flaws are not present on these sides as well. They simply are not strength determining as they are less scarce than the surface flaws. When extrapolating towards a low failure probability the near surface flaws will become the crucial ones as they show a larger scatter and so will become at a certain flaw size scale more frequent (compare lower Weibull modulus of the smooth and dull surfaces of 3YSZ and 6ScSZ with the rough ones). Hence from a design perspective rather dull and smooth sides of zirconia tapes should be considered.

The ranking of the different zirconia materials regarding their inert strength does not change at low failure probabilities, as the Weibull for all materials is close to $m = 10$ (except the smooth side of the 160µm 10Sc1CeSZ). This indicates a comparable quality of the manufacturing process as the ranking basically follows the fracture toughness of the different compounds. Also taking SCCG into account has no significant influence on the ranking as the crack growth rates in humid atmospheres are comparable as well. It is interesting to note that the presence of humidity reduces the strength drastically already on small time scales, whereas at larger scales the strength is further significantly reduced. Figure 2.11 also depicts the strength decrease of the dull side of 3YSZ and the smooth side of 6ScSZ for different humidity levels. It is revealed that the amount is only of minor importance and that the crack growth parameters need to be determined for one representative environment, e.g. normal laboratory air. Further description of the high temperature behaviour, ageing and the strength of electrolyte-electrode assemblies will be the topic of a subsequent article.

Next to the scandia stabilized zirconia and the 3YSZ, the other prominent zirconia compound applied for SOFCs is 8 mol% Y_2O_3 stabilized ZrO_2 (8YSZ). The best strength parameters at RT for this compound were published by *Selcuk* and *Atkinson* [38] and read: $\sigma_0 \cong 446$ MPa, $m = 6.7$ and $S_{eff} \approx 9$ mm² (estimated from the size of the inner loading of the ring-on-ring test rig). As the strength was not determined under inert conditions, the characteristic inert strength is roughly

estimated according to Figure 2.10 to be 125% of the published one assuming a load rate greater than 100 MPa/s. Applying Equation (2.6) gives then the corresponding strength level for a $P = 0.0001$ and a $S = 10$ cm^2 of $\sigma = 69.8$ MPa and is also plotted in Figure 2.11. Compared to the other compounds, it possesses a rather low strength. Considering that this strength is then even further lowered if subcritical crack growth is taken into account, it appears to be not suitable for the application in electrolyte supported SOFC. This is further underlined by the fact that 10Sc1CeSZ with a comparable toughness ($K_{Ic,8YSZ} = 1.61 \pm 0.12$ MPa m^{½} [36], $K_{Ic,10Sc1CeSZ} = 1.8 \pm 0.17$ MPa m^{½}) and thus with a comparable potential robustness, has a significantly higher ionic conductivity [39] and is therefore to be favoured.

2.5 Conclusions

(i) The large surface of electrolytes used in SOFCs requires the application of strength tests, which also load comparable surface areas, in order to determine the strength at low failure probabilities with a relative high confidence. It is found that Ring-on-Ring bending test is most suited for this purpose as the more accurate Ball-on-3-Balls test loads too small areas and might even measure a not relevant strength distribution. Ball-on-3-Balls test on the other hand is well suited to describe material intrinsic properties such as static fatigue due to sub critical crack growth, where large amounts of specimens and a high accuracy is required.

(ii) Comparing the inert strength of the four different zirconia compounds investigated, it was found that the difference in strength is basically determined by the fracture toughness. Hence the strength of the 6ScSZ and 6Sc1CeSZ is comparable to 3YSZ, while they provide a greater ionic conductivity. 10Sc1CeSZ on the other hand possesses a significant lower toughness which is directly reflected in a relatively low strength.

(iii) Extrapolating their strength down to realistic loaded surface areas and failure probabilities, the respective strength is much lower than the measured characteristic strength, which is due to a Weibull modulus close to $m = 10$, as found to be common for most tapes. The strength of all compounds is further significantly reduced taking sub critical crack growth into account, which is promoted due to the omnipresence of moisture in environmental air.

(iv) In general it can be concluded that if stresses are limited to less than 100 MPa, the application of the tetragonal zirconia electrolytes should be safe, which appears to be feasible.

2.6 Acknowledgements

The authors would like to thank *R. Bächtold, U. Weissen, H.-J. Schindler* and *B. Iwanschitz*, for the unconditional support. Furthermore, the funding of this work by the *Swiss Federal Office of Energy* under the contract no. 8100076; SI/500084-02 and by *Swisselectric Research* within the *SOF-CH-ESC* project is gratefully acknowledged.

2.7 References

[1] R. Danzer, T. Lube, P. Supancic, R. Damani, Advanced Engineering Materials, 10 (2008) 275-298.
[2] M. Radovic, E. Lara-Curzio, G. Nelson, Ceramic Engineering and Science Proceedings, 27 (2007) 373-381.
[3] W.M. Rainforth, F.L. Lowrie, R.D. Rawlings, Journal of the European Ceramic Society, 20 (2000).
[4] A.N. Kumar, B.F. Sorensen, Materials Science and Engineering, A333 (2002) 380.
[5] J. Alcala, M. Anglada, Materials Science and Engineering a-Structural Materials Properties Microstructure and Processing, 232 (1997) 103-109.
[6] A. Selcuk, A. Merere, A. Atkinson, Journal of Materials Science, 36 (2001) 1173-1182.
[7] B.F. Sorensen, S. Primdahl, Journal of Materials Science, 33 (1998) 5291-5300.
[8] J. Malzbender, P. Batfalsky, R. Vaßen, V. Shemet, F. Tietz, Journal of Power Sources, 201 (2012) 196-203.
[9] J. Chevalier, L. Gremillard, A.V. Virkar, D.R. Clarke, Journal of the American Ceramic Society, 92 (2009) 1901-1920.
[10] M. Chen, Y.L. Liu, A. Hagen, P.V. Hendriksen, F.W. Poulsen, Fuel Cells, 9 (2009) 833-840.
[11] A. Mai, B. Iwanschitz, U. Weissen, R. Denzler, D. Haberstock, V. Nerlich, A. Schuler, in: S.C. Singhal, K. Eguchi (Eds.) ECS Transactions, 2011, pp. 87-95.
[12] F. Fleischhauer, A. Tiefenauer, T. Graule, R. Danzer, A. Mai, J. Kuebler, Journal of Power Sources, 258 (2014) 382-390.
[13] S.P.S. Badwal, F.T. Ciacchi, D. Milosevic, Solid State Ionics, 136-137 (2000) 91-99.

[14] A. Nakajo, J. Kuebler, A. Faes, U.F. Vogt, H.J. Schindler, L.-K. Chiang, S. Modena, J. Van Herle, T. Hocker, Ceramics International, 38 (2012) 3907-3927.
[15] Y. Chen, A. Aman, M. Lugovy, N. Orlovskaya, S. Wang, X. Huang, T. Graule, J. Kuebler, Fuel Cells, 13 (2013) 1068-1075.
[16] J. Malzbender, R.W. Steinbrech, Journal of the European Ceramic Society, 27 (2007) 2597-2603.
[17] N. Orlovskaya, S. Lukich, G. Subhash, T. Graule, J. Kuebler, Journal of Power Sources, 195 (2010) 2774-2781.
[18] S. Spinner, W.E. Tefft, Proceedings ASTM, 61 (1961).
[19] J. Kuebler, U.F. Vogt, D. Haberstock, J. Sfeir, A. Mai, T. Hocker, M. Roos, U. Harnisch, Fuel Cells, 10 (2010) 1066-1073.
[20] J. Kuebler, Ceramic Engineering and Science Proceedings, 20 (1999) 495-499.
[21] R. Danzer, P. Supancic, W. Harrer, Journal of the Ceramic Society of Japan, 114 (2006) 1054-1060.
[22] A. Börger, P. Supancic, R. Danzer, Journal of the European Ceramic Society, 22 (2002) 1425-1436.
[23] A. Börger, P. Supancic, R. Danzer, Journal of the European Ceramic Society, 24 (2004) 2917-2928.
[24] R. Damani, R. Gstrein, R. Danzer, Journal of the European Ceramic Society, 16 (1996) 695-702.
[25] T. Fett, Engineering Fracture Mechanics, 64 (1999) 357-362.
[26] T. Kushi, K. Sato, A. Unemoto, S. Hashimoto, K. Amezawa, T. Kawada, Journal of Power Sources, 196 (2011) 7989-7993.
[27] EN 843-5, in: EN 843-5, 1997, pp. 40.
[28] R. Bermejo, P. Supancic, R. Danzer, J. Eur. Ceram. Soc., 32 (2012) 251-255.
[29] S.W. Freiman, S.M. Wiederhorn, J.J. Mecholsky, J. Am. Ceram. Soc., 92 (2009) 1371-1382.
[30] R. Bermejo, P. Supancic, C. Krautgasser, R. Morrell, R. Danzer, Engineering Fracture Mechanics, 101 (2013) 108-121.
[31] B. Lawn, Fracture of Brittle Solids, Cambridge University Press, Cambridge, 1993.
[32] H. Peterlik, Journal of the European Ceramic Society, 13 (1994) 509-519.
[33] P.H. Supancic, H.M. Schopf, Journal of the European Ceramic Society, 32 (2012) 4031-4040.
[34] S. Strobl, P. Supancic, T. Lube, R. Danzer, Journal of the European Ceramic Society, 32 (2012) 1491-1501.
[35] J. Chevalier, C. Olagnon, G. Fantozzi, Journal of the American Ceramic Society, 82 (1999) 3129-3138.
[36] A. Atkinson, A. Selcuk, Solid State Ionics, 134 (2000) 59-66.
[37] R.M. Anderson, L.M. Braun, Journal of the American Ceramic Society, 73 (1990) 3059-3062.
[38] A. Selcuk, A. Atkinson, Journal of the American Ceramic Society, 83 (2000) 2029-2035.
[39] V. Kharton, F. Marques, A. Atkinson, Solid State Ionics, 174 (2004) 135-149.

Chapter 3

HIGH TEMPERATURE MECHANICAL PROPERTIES OF ZIRCONIA TAPES USED FOR ELECTROLYTE SUPPORTED SOLID OXIDE FUEL CELLS

Journal of Power Sources 273 (2015) 237-243

Felix Fleischhauer[1,2], Raul Bermejo[2], Robert Danzer[2], Andreas Mai[3], Thomas Graule[1], Jakob Kuebler[1]

[1]Empa, Swiss Federal Laboratories for Materials Science and Technology, Laboratory for High Performance Ceramics, Ueberlandstr. 129, 8600 Duebendorf, Switzerland

[2]Institut für Struktur-und Funktionskeramik, Montanuniversität Leoben, Peter-Tunner-Str. 5, 8700 Leoben, Austria

[3]Hexis Ltd., Zum Park 5, 8404 Winterthur, Switzerland

Abstract

Solid-Oxide-Fuel-Cell systems are efficient devices to convert the chemical energy stored in fuels into electricity. The functionality of the cell is related to the structural integrity of the ceramic electrolyte, since its failure can lead to drastic performance losses. The mechanical property which is of most interest is the strength distribution at all relevant temperatures and how it is affected with time due to the environment.

This study investigates the impact of the temperature on the strength and the fracture toughness of different zirconia electrolytes as well as the change of the elastic constants. 3YSZ and 6ScSZ materials are characterised regarding the influence of sub critical crack growth (SCCG) as one of the main lifetime limiting effects for ceramics at elevated temperatures. In addition, the reliability of different zirconia tapes is assessed with respect to temperature and SCCG. It was found that the strength is only influenced by temperature through the change in fracture toughness. SCCG has a large influence on the strength and the lifetime for intermediate temperature, while its impact becomes limited at temperatures higher than 650°C. In this context the tetragonal 3YSZ and 6ScSZ behave quite different than the cubic 10Sc1CeSZ, so that at 850°C it can be regarded as competitive compared to the tetragonal compounds.

3.1 Introduction

Electrolyte supported solid oxide fuel cells (SOFCs) are state of the art electrochemical devices, which are employed for the efficient conversion of chemical energy stored with in a fuel (e.g. natural or bio gas) into electricity. Such systems contain many ceramic components, which have to maintain their structural integrity in order to function properly throughout the whole targeted lifetime. Here the electrolyte is responsible for the cells structural integrity, while physically separating the fuel and the air from one another and providing a sufficient ionic conductivity. If the separation is not maintained, intra cellular leakage will negatively affect the cell and stack performance instantaneously, which is the case, if the electrolyte fractures.

In order to predict the risk of failure a prospective electrolyte has to be properly characterized regarding its mechanical behaviour within a system specific environment, which is characterised by mechanical stresses, temperature and the presence of chemically active species. Since the state of the art electrolytes are brittle ceramics, such as zirconia and ceria-gadolinia, the strength depends in principle on two material specific features: the flaw size and shape distribution, within the components volume or at the surface, and its fracture toughness [1]. Both are first of all influenced by the material selection, processing and handling but also later on by the exposure to a system specific environment, where mechanical stresses, elevated temperatures and the contact with other components may alter these properties either instantaneously or with time. For instance subcritical crack growth (SCCG) [2-5] and cracks growing from the electrodes into the electrolyte [6, 7] in combination with an applied stress influence the flaw size distribution whereas temperature itself changes the toughness. Ageing effects which are diffusion controlled and thus time dependent processes may also decrease or increase the materials resistance towards fracture [8-10] or change the stress state due to creep relaxation. All these aspects have to be considered, when assessing the reliability of a ceramic component, while the proper and accurate determination of the initial strength distribution, which reflects the initial flaw size distribution, is the most crucial one. A comprehensive overview of the available strength data of commercial and experimental yttria stabilized zirconia and ceria-gadolinia tapes was given by *Nakajo* et al. [11], while scandia stabilized zirconia has received less attention [12-14]. Studies investigating the specific reliability of anode supported SOFCs for a

given load environment were already undertaken by *Nakajo* et al. and *Clague* et al. [15, 16]. However they lack a sound knowledge of afore mentioned material specific behaviour, simply due to the huge effort, which is required to thoroughly gather all necessary parameters.

Hence this study aims to provide understanding on how the temperature influences the mechanical properties such as strength, fracture toughness, subcritical crack growth and the elastic constants of zirconia-based SOFC electrolytes. The emphasis here lies on the characterization of scandia doped zirconia electrolytes, which are known for their high ionic conductivity [17] and 3 mol% yttria stabilized zirconia (3YSZ) as a reference material. The reliability of these tapes is discussed considering thermal stresses and clamping loads and the evolution of their strength at elevated temperatures taking sub critical crack growth and the change of the elastic constants into account.

3.2 Experimental

The experimental investigation is centred on four different zirconia compounds. The tape samples of 6ScSZ (commercial code: FF-2003501), 6Sc1CeSZ (FF-2003507), 10Sc1CeSZ (FF-2003505) and 3YSZ (FF-2003504) were supplied by *Hexis* (Winterthur, Switzerland) and had a nominal thickness of 160, 110, 230 and 140 µm respectively.

The elastic constants of 3YSZ, 6ScSZ, 6Sc1CeSZ were measured at various temperatures using the Impulse-Excitation-Technique (IET) as described in [18], while bearing the rectangular plates (12x45x3.25 mm^3) either on a cross or two parallel bars in order to measure either their flexural or torsional frequencies in accordance with the EN 843-2 standard. These frequencies are then converted into the Young's and shear modulus following the approach of *Spinner* and *Tefft* [19]. The samples were manufactured via uniaxial pressing and sintering from the same powder (also supplied by *Hexis*) as was used for the respective tapes, except for 3YSZ, which was purchased from *Tosoh* (Tokyo, Japan). The powders have an average grain size between 0.5-0.6 µm and were sintered at 1580°C for 2 h. The sample densities were determined via the dimensions and the weight and are greater than 98% of the theoretical density.

Ball-on-3-Balls (B3B) tests were conducted on rectangular specimens as described in Ref. [20]. For 3YSZ, 6ScSZ, 10Sc1CeSZ the rougher tape side (side which was cast onto the support foil) and for 6Sc1CeSZ the dull appearing side (side which was opposite to the support foil during the casting process) was consequently tested. If otherwise, it is explicitly mentioned. The strength analysis of these bending tests is based on the work of *Börger* et al. [21], where the maximum principle stress σ_{max} is related to the fracture force F by:

$$\sigma_{max} = f\frac{F}{t^2} \tag{3.1}$$

where t is the specimen thickness and f is a dimensionless proportionality factor, which depends on the thickness, size and Poisson's ratio of the specimen and the diameter of the balls. This factor and the corresponding effective surface area have been calculated for balls with a diameter of 2.2 mm and plates of 4x3 mm^2 using the same finite element-model as in [20], with the same test rig as described in [13]. The results are comprised in following sample and test rig specific fit-function:

$$f = 0.21427 + \frac{((2.9136 + 9.958\ mm^{-1}t - 4.65\ mm^{-2}\ t^2)(1 + 0.9393\ \nu)}{1 + 9.63\ mm^{-1}\ t} \tag{3.2}$$

which describes f with an error of less than 1% for thicknesses between $0.1 \leq t \leq 0.4$ mm and a Poisson's ratio between $0.2 \leq \nu \leq 0.4$.

All B3B-tests have been performed in a force controlled mode providing a constant force rate (N/s) during each test. Using Equation (3.1) and (3.2) the applied load rate (MPa/s) can be obtained, which was between 700 and 1000 MPa/s (so that fracture occurred in less than two seconds), if not mentioned otherwise.

3.3 Results

3.3.1 Elastic constants as a function of temperature

In order to describe the elastic behaviour of thin plates the Young's modulus and the Poisson's ratio have to be known and since electrolytes are operated at elevated temperatures, their elastic constants also have to be known at these conditions. Figure 3.1 shows the results of the IET experiments. Additionally the Young's modulus of 3YSZ is plotted according to *Giraud* and *Canel* [22], which was measured using the same technique. Furthermore, the elastic constants of 10Sc1CeSZ are shown, which were taken from *Kushi* et al. [23] and which will be used for the following discussion of the present 10Sc1CeSZ tapes.

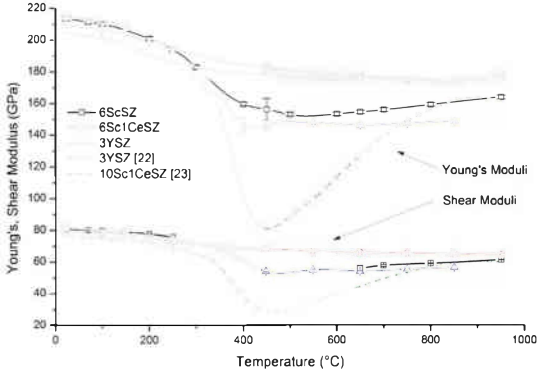

Figure 3.1: Young's and shear modulus at varying temperatures for 3YSZ, 6ScSZ and 6Sc1CeSZ including the standard deviation of each measurement. A reference curve is taken for 3YSZ from [22], while the values of 10Sc1CeSZ are taken from [23].

All zirconia compounds display the same behaviour, while possessing comparable Young's and shear moduli up to a temperature of 250°C. While 3YSZ then continues its monotonic decay agreeing with the data given in [22], all other compounds run through a minimum between 400 and 500°C, which becomes more pronounced as the

content of doping is increased. This minimum is accompanied by increased internal friction and damping [23]. This damping is responsible that the shear modulus of 6ScSZ cannot be obtained with the applied method over a large temperature range between 300°C and 600°C. This is, because any torsional excitement is quickly absorbed, therefore no torsional vibration of the sample can be detected. The values taken for further discussion and analysis of the four different materials investigated in the present study are given in Table 3.1, including the standard deviation of the three samples from this study, which was calculated from at least ten single experiments per sample and temperature.

Table 3.1: Elastic parameters used for further discussion including the standard deviation given in the brackets. The Poisson's Ratio ν was calculated from the shear G and the Young's modulus E according to $\nu=E/2G-1$.Values of 10Sc1CeSZ are taken from [23].

T	3YSZ		6ScSZ		6Sc1CeSZ		10Sc1CeSZ	
(°C)	E (GPa)	ν	E (GPa)	ν	E (GPa)	ν	E (GPa)	ν
25	214.3 (±0.1)	0.314 (±0.002)	213.6 (±1.5)	0.321 (±0.005)	209.5 (±0.1)	0.314 (±0.001)	204.6	0.345
250	195.2 (±0.8)	0.312 (±0.002)	194.2 (±1.4)	0.280 (±0.01)	191.9 (±1.4)	0.314 (±0.004)	185.0	0.345
350	"	"	"	"	"	"	155.7	0.361
450	182.5 (±0.1)	0.336 (±0.002)	156.2 (±7)	0.3*	146.2 (±0.2)	0.340 (±0.01)	80.9	0.401
650	176.9 (±0.1)	0.337 (±0.002)	155.0 (±1.1)	0.372 (±0.022)	146.4 (±0.5)	0.343 (±0.005)	127.4	0.411
850	173.6 (±0.1)	0.334 (±0.001)	160.1 (±1.1)	0.340 (±0.006)	148.9 (±0.1)	0.308 (±0.001)	161.9	0.355

*Poisson's ratio of 6ScSZ at 450°C was estimated due to the non-applicability of the IET-method at that temperature

3.3.2 High temperature inert strength

The operating temperature of electrolyte supported SOFCs is typically between 700°C and 900°C, while the trend goes to ever decreasing temperatures. Therefore the strength of an electrolyte has to be known over the temperature range from room temperature to operating temperatures, in order to assess its suitability from a reliability point of view. For this purpose the four different zirconia compounds were investigated regarding their material specific temperature dependent strength. Since this behaviour does typically not depend on the size of flaws, the B3B-test was adapted for high temperature measurements by applying a test rig manufactured from alumina. For every temperature step at least 10 specimens per material were tested, selecting for 6ScSZ, 10Sc1CeSZ and 3YSZ the rough sides of the tapes and for

6Sc1CeSZ the dull sides. To avoid SCCG all tests were conducted in dry argon(80%)/oxygen(20%). The oxygen was to ensure that zirconia does not get reduced at the surface, since it is unknown how this would affect the strength or the toughness.

Table 3.2 shows the results of the median strength for different temperature levels. For all materials 30 specimens were tested at RT, which resulted in a Weibull modulus for 3YSZ, 6ScSZ, 6Sc1CeSZ and 10Sc1CeSZ of $m_{3YSZ,RT} = 20$, $m_{6ScSZ,RT} = 18$, $m_{6Sc1CeSZ,RT} = 20$ and $m_{10Sc1CeSZ,RT} = 11$, respectively. For 6ScSZ and 3YSZ the Weibull modulus at RT was reproduced at 850°C testing more than 20 specimens ($m_{3YSZ,850°C} = 20$, $m_{6ScSZ,850°C} = 18$), which supports the assumption, that also at elevated temperatures the distribution and thus failure mechanism does not change and the same flaws are governing fracture. According to the definition of the stress intensity factor [24]:

$$K_{Ic} = \sigma_{frac} Y \sqrt{\pi a} \tag{3.3}$$

the fracture toughness K_{Ic} is proportional to the fracture stress σ_{frac}. Therefore, the change in strength is solely attributed to a change in fracture toughness, making it possible to apply the following relation as a consequence of Equation (3.3) between the strength and the toughness:

$$\frac{\sigma(T_1)}{\sigma(T_2)} = \frac{K_{Ic}(T_1)}{K_{Ic}(T_2)} \tag{3.4}$$

so that the temperature dependency of the toughness can be obtained (see also Table 3.2), applying the RT toughness values given in Ref. [13]. Figure 3.2 shows the toughness normalised to the RT-values. The applicability of Equation (3.4) is not always given, since flaws may alter with temperature. However, comparing the dull and the rough side of 6ScSZ and taking the directly measured toughness of 3YSZ into account, shows that for zirconia and the considered temperature range Equation (3.4) holds and delivers values within a justifiable error.

It is remarkable that the zirconia compounds consisting predominately of the tetragonal phase behave fairly the same, following the same monotonic decay, which is probably governed by the ability of the tetragonal phase to transform into the

monoclinic phase and leads to the well-known transformation toughening [25]. The higher the temperature the lower the driving force for this transformation and hence the volume fraction at a crack tip, which transforms, decreases lowering the toughening effect. 10Sc1CeSZ does not possess this mechanism, which is why it has the lowest toughness to begin with. Its toughness is mainly determined by the surface energy, which together with the fracture toughness is proportional to the Young's modulus [26]. Hence, 10Sc1CeSZ follows qualitatively the trend of its Young's modulus shown in Figure 3.1, which is in agreement with the strength data, toughness and Young's modulus published by *Orlovskaya* et al. [18] and has also been found for cubic 8YSZ [2].

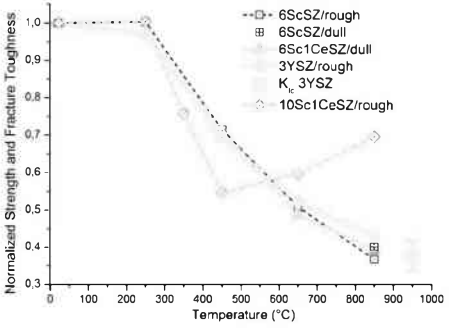

Figure 3.2: Temperature dependent fracture toughness normalised to room temperature values, including the normalised toughness of 3YSZ at 950°C taken from [27].

For SOFCs the dominant mechanical loads are typically deformation controlled, which means that a material has to sustain a certain deformation rather than a force or stress. This is the case for thermal stresses, residual stresses within the cell due to thermal mismatch strains and local stresses due to an uneven clamping of the cell [28]. Since clamping loads can become significant in magnitude and are present from RT to operating temperature, the temperature behaviour of the biaxial fracture strain ($\varepsilon_{frac,biax} = \sigma_{frac,biax}\,(1-\nu)/E$) is considered as well and shown in Figure 3.3.

For 6ScSZ and 6Sc1CeSZ the RT level is maintained until T = 450°C, from where it then drops down to 50% at 850°C. 3YSZ behaves similarly but begins its decay already at T = 250°C. Again 10Sc1CeSZ shows a complete different trend. Its strength minimum at 450°C is overcompensated by the Young's modulus and turns into a maximum, while it retains at 850°C 90% of its RT fracture strain.

Table 3.2: Median strength for varying temperature and the corresponding fracture toughness calculated according to Equation (3.3) from high temperature strength data.

T	3YSZ		6ScSZ		6Sc1CeSZ		10Sc1CeSZ	
(°C)	$\sigma_{50\%}$ (MPa)	K_{Ic} (MPa m$^{1/2}$)	$\sigma_{50\%}$ (MPa)	K_{Ic} (MPa m$^{1/2}$)	$\sigma_{50\%}$ (MPa)	K_{Ic} (MPa m$^{1/2}$)	$\sigma_{50\%}$ (MPa)	K_{Ic} (MPa m$^{1/2}$)
25	1595	5.0* (±0.24)	1360	4.1** (±0.25)	1929	3.7** (±0.1)	665	1.8** (±0.17)
250	1548	4.8	1365	4.1	1872	3.6	668	1.8
350	"	"	"	"	"	"	504	1.4
450	1107	3.5	973	2.9	1374	2.6	364	1.0
650	831	2.6	691	2.1	939	1.8	397	1.1
850	685	2.1	499	1.6	756	1.4	463	1.3
950	"	1.9* (±0.21)	"	"	"	"	"	"

*Values taken from [27]; **Values taken from [13]

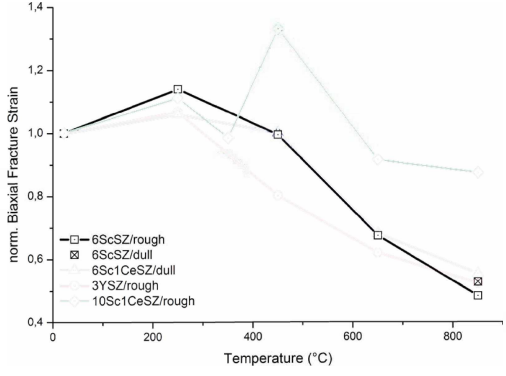

Figrue 3.3: Biaxial fracture strain normalised to the RT values for different zirconia compounds and varying temperature.

3.3.3 Strength at high temperature affected by sub critical crack growth

If strength determining flaws are accessible by moisture which is omnipresent in environmental air, these flaws tend to grow subcritically if a stress below the respective fracture stress is applied. Thus the strength itself becomes dependent on the time under load, which leads to a limited life time. Since the perspective operating time of a fuel cell can be up to eight years including several thermo cycles, while being subjected to humid environments on both sides, this effect has to be measured for varying temperatures. Typically SCCG is described via the crack growth rate da/dt of a crack or a flaw with the size a, which typically follows a Paris law in the form of:

$$\frac{da}{dt} = v_0 \left(\frac{K_{app}}{K_{Ic}}\right)^n \tag{3.5}$$

where v_0 is the reference velocity, which is the crack growth rate when the applied stress intensity factor K_{app} reaches the fracture toughness K_{Ic}. n is the so called crack growth exponent, which is lower the more sensitive a material is to moisture. Since K_{app} depends not just on the applied stress σ_{app} but also on the crack size a, expressed by (analogue to Equation 3.3):

$$K_{app} = \sigma_{app} Y \sqrt{\pi a} \tag{3.6}$$

with Y being the geometry factor of the crack, which was set to $Y = 0.85$ to reflect semi-elliptical surface cracks [29], which remains independent of the crack size for small cracks. SCCG can now be described by the two parameters v_0 and n, which have to be determined for a defined temperature and humidity. By inserting Equation (3.6) in Equation (3.5) a differential equation is obtained. If the applied stress is constantly increased with the load rate $\dot{\sigma}$, following expression can be derived [1]:

$$\log \sigma_{app}(t_f) = \log \sigma_f = \frac{1}{n+1} \log \dot{\sigma} + \frac{1}{n+1} \log\left(\frac{2\, K_{IC}^2\, (n+1)}{v_0\, \pi\, Y^2\, (n-2)}\, \sigma_{inert}^{(n-2)}\right) \tag{3.7}$$

with σ_{inert} being the inert strength in the absence of the SCCG effect and σ_f the fracture stress. By measuring the strength as a function of the load rate, it is

possible to determine the crack growth parameters. For the four zirconia compounds investigated in the present study these parameters have been already published at RT for different humidity levels by *Fleischhauer* et al. [13]. It was found that already at RT the strength is affected drastically by SCCG even at small time scales. In the present study, 6ScSZ has been chosen to investigate how this effect changes with temperature by measuring the strength as a function of the load rate while keeping the absolute humidity constant at a partial pressure of p_{H2O} = 11.5 mbar (43% relative humidity at T = 22°C) and applying the same data analysis procedure as in Ref. [13]. The constant humidity was ensured by bubbling a dry argon(80%)/oxygen(20%) mixture through a saturated aquatic K_2CO_3-solution kept at T = 22°C and is supposed to represent environmental air. The results including the data at RT taken from [13] are shown in Figure 3.4.

At T = 250°C the strength shifts to greater values, which leads to a strengthening of 6ScSZ at elevated temperatures, while being subjected to humid environments. This phenomenon has not been reported before in literature and is at this point not soundly understood. Interestingly this effect apparently requires a certain time under load, as no strength increase has been found for the samples tested at a very high load rate of 1 GPa/s, although they were held equally long compared to the other samples at 250°C prior to the test. It is also remarkable that the crack growth exponent just significantly changes at T = 450°C towards a much lower value. At T = 650°C instead of a continuous strength decay a formation of a threshold strength σ_{th} is recognisable, which at T = 850°C is even at the level of the inert strength. For the rough side of 3YSZ the threshold strength at T = 650°C and a partial water vapour pressure of p_{H2O} = 8 mbar (30% relative humidity at T = 22°C) has been determined to be $\sigma_{th,650°C}$ = 797 MPa ($\sigma_{inert,650°C}$ = 840 MPa), while at 850°C no significant crack growth occurred as well.

Hence the effect of SCCG becomes very limited at higher and for the operation of SOFCs rather relevant temperatures. This trend has been already reported for 3YSZ, 8YSZ and also for magnesia partially stabilized zirconia by *Alcala* and *Anglada* [5], *Choi* [30] and *Davidson* et al. [31], respectively and leads for zirconia compounds to the general assumption that at temperatures greater than 800°C no significant humidity related SCCG occurs.

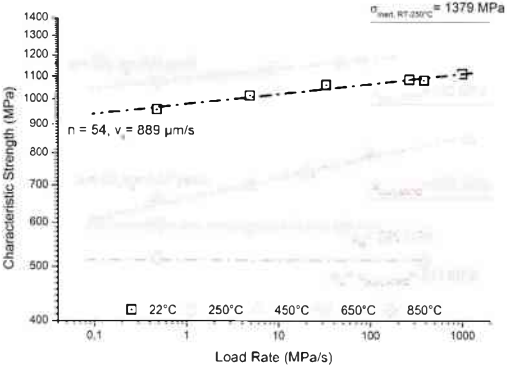

Figure 3.4: Strength dependence on the load rate of 6ScSZ at vaying tempertures including the respective inert srength levels, SCCG parameter and observed threshold strength at T = 650°C and T = 850°C. The inert strength is determined at a loading rate close to 1 GPa/s.

3.4 Discussion

Having determined the strength distribution, the temperature dependence and the SCCG parameter, it is finally possible to compare and assess the investigated zirconia compounds regarding their strength in humid environments for different temperatures. If no SCCG occurs the strength σ is a function of the required failure probability and the loaded surface area and can be described via the standard Weibull distribution [1]:

$$\sigma(S, P, T) = \left(\frac{S_0}{S}\,\sigma_0(T)^m\, ln\left(\frac{1}{1-P}\right)\right)^{\frac{1}{m}} \tag{3.8}$$

where the temperature dependency is expressed through the characteristic strength σ_0, which can be obtained from RT values by applying Equation (3.3). If SCCG has to be taken into account, the respective time dependent strength is obtained by the combination of Equation (3.5-6) and (3.8) and becomes:

$$\sigma(T,S,P,t_f) = \left(\frac{K_{Ic}^{\,2} \left(\frac{S_{eff}}{S}\, \sigma_0(T)^m \ln\left(\frac{1}{1-P}\right) \right)^{\frac{n(T)-2}{m}}}{v_0(T)\, t_f\, \pi\, Y^2 \left(\frac{n(T)}{2}-1\right)} \right)^{1/n(T)} \tag{3.9}$$

with the reference velocity v_0 and the crack growth exponent n being temperature dependent as well. If SCCG reaches a threshold, Equation (3.8) is applied again inserting the respective time independent threshold strength instead of the inert strength. Taking the strength data of the dull sides (side of the cast tape which was opposite to the support foil) of commercial 3YSZ, 6ScSZ and 10Sc1CeSZ tapes from a previous study [13], given in Table 3.3, the influence of temperature and SCCG can be quantitatively assessed for a given system and its respective load environment. To give an example how these different dependencies influence the strength, the load environment of the μ-CHP (small scale combined heat power plant) the *Galileo 1000N* of *Hexis AG* (Winterthur, Switzerland) [32] is considered for further discussion, which has been described in a previous study [28]. At T = 850°C it is assumed that the peak loads are caused by thermal stresses, which effectively load a surface area S of approximately 10 cm² of the total cell area of 200 cm². For simplicity the same area is kept constant for varying temperatures. As one single failed cell might harm a whole stack and can lead to significant performance losses, a required failure probability P of 1:10,000 is assumed, which means that in average, roughly every hundredth stack might contain a failed cell. The prospective operating time of the stack is 8 years, of which the system remains idle between 0-50% of the time, depending on the heat demand. Therefore, a life time t_f of four years is considered for RT, while at T = 850°C no time dependent strength decay is expected. According to Equation (3.8) and (3.9) the respective strength of the three zirconia compounds is shown in Figure 3.5 including the 90% confidence intervals.

Apart from the thermal stresses, residual stresses and clamping loads are also present at all times, thus also during thermo cycling. Hence the strength of 6ScSZ is plotted also for 250 and 450°C according to Equation (3.9) assuming a life time of twenty days, which is a rough and conservative estimation of the cumulated time the electrolyte is subjected to SCCG at the respective temperature during cooling down and heating up, as one complete thermo cycle requires one day, assuming twenty cycles during 8 years. At 650°C the threshold strength observed for 3YSZ and 6ScSZ

is translated analogue to Equation (3.4) into a threshold stress intensity factor $K_{I,th}$, below which no SCCG occurs, applying the respective inert strength and the corresponding fracture toughness at 650°C. Again following Equation (3.4) the RT strength given in Table 3.3 can be translated into the SCCG affected strength at 650°C applying the threshold $K_{I,th}$ instead of the fracture toughness. The strength of 3YSZ at 450°C is given, using the $K_{I,th}$ = 2.2 MPa m^{½} at 450°C given by [5], while the respective strength of 8YSZ at RT and 900°C is given as comparison and taken from [33]. Among all the published data, this data shows until now the highest achievable strength at high temperatures for this compound and is at the same time the most dependable since it was obtained testing 30 and 20 specimens, respectively applying a low friction high temperature RoR set up, which ensured a high level of accuracy. The RT SCCG affected strength was calculated, using the threshold stress intensity factor $K_{I,th}$ = 0.72 MPa m^{½} and the fracture toughness of K_{Ic} = 1.51 MPa m^{½}.

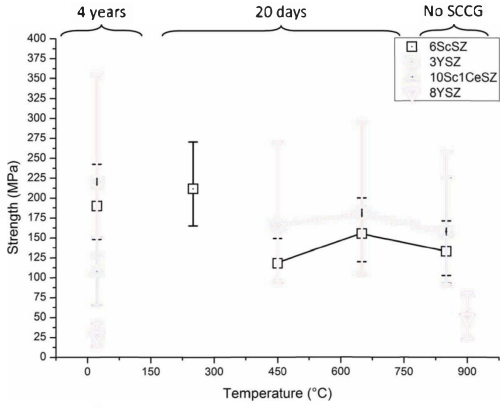

Figure 3.5: Strength of different zirconia tapes including the 90% confidence intervals at varying temperatures for S = 10 cm^2 and P = 0.0001, taking SCCG for different lifetimes into account.

Table 3.3: Selection of strength and SCCG data at RT used for further discussion taken for 8YSZ from [33] and the other compounds from [13]. The values given in the brackets are the 90% confidence intervals.

	Characteristic strength σ_0 (MPa)	Weibull modulus m	Reference surface area S_0 (mm²)	Crack growth exponent n	Reference velocity v_0 (m/s)
3YSZ	1433 (1501 | 1369)	10 (15 | 7.2)	15	55	0.09
6ScSZ	1126 (1153 | 1100)	11 (13.6 | 9.2)	18	54	0.9
10Sc1CeSZ	1136 (1168 | 1106)	12 (15.0 | 9.2)	0.025	37	0.004
8YSZ	446* (468 | 425)	6.7 (8.4 | 5.2)	9**	-	-
8YSZ (900°C)	282 (296 | 268)	8 (10.7 | 5.7)	9**	-	-

*taken as inert strength, although measured in humid air
**values roughly estimated, as they are not explicitly given

When taking SCCG into account the strength over the temperature of 3YSZ and 6ScSZ does not show a monotonic decay as for the inert strength depicted in Figure 3.2. At T = 450°C the strength becomes comparable with that at T = 850°C, while it rises again when coming to lower temperatures. Considering 10Sc1CeSZ, it is revealed, that SCCG leads to a lower strength at RT than at 850°C, where it surprisingly even reaches up to the levels of the tetragonal zirconia compounds. 8YSZ on the other hand appears to be the weakest of the common zirconia. Comparing the strength to the magnitude of thermal stresses which are expected to rise due a generally given inhomogeneous temperature distribution throughout the cell and which are typically in the range of 50-60 MPa [16, 28, 34, 35], it is revealed that 8YSZ is not suited for the application in electrolyte supported fuel cells.

To evaluate the risk of cell failure the strength, which can be interpreted as a design stress, is plotted for 6ScSZ, 10Sc1CeSZ and 3YSZ at RT, assuming again four years of lifetime and at 850°C versus the failure probability for varying loaded surface areas, as shown in Figure 3.6. Assuming again thermal stresses in the range of 50-60 MPa the depicted zirconia compounds show a high reliability even with loading surface areas as large as 100 cm². Interestingly the differences between the three materials at 850°C are small if not negligible considering the confidence intervals given in Figure 3.5. Next to thermal stresses the electrolyte is also subjected to stresses due to the clamping, as the contact between the metallic interconnect (MIC) and the cell is never perfectly flat and leads to local bending, and residual stresses due to thermal mismatch of the cell components. The residual stresses are small at

operating temperatures, while they increase if the cell is cooled down to RT, putting the electrolyte under a slight compressive load (~20 MPa) [28, 36]. Hence the residual stresses can be neglected for further discussion. Stresses due to clamping on the other hand can become significant and might lead to local damage [28]. Figure 3.6 can now be used to reveal the allowed magnitude of clamping stresses. For 3YSZ and 6ScSZ the respective analysis just has to be made at operating temperatures, since the strength at RT is significantly higher. Depending on the tolerated risk of failure and the area where the peak stresses (superposition of all expected loads) act on, stresses apart from thermal stresses (assumed to be ~50 MPa) can reach between 50 and 150 MPa. For 10Sc1CeSZ the difference in strength between RT and 850°C is roughly the amount for the reported thermal stresses, hence the allowed clamping loads for this material have to be oriented on the RT strength level, which results in a similar range of 50-150 MPa as for the tetragonal compounds. Hence according to the strength data given in Table 3.3, the highly conductive 10Sc1CeSZ compound can be regarded as competitive compared to 3YSZ and 6ScSZ from a reliability perspective.

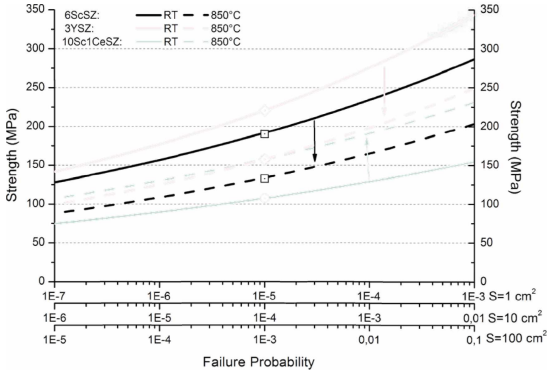

Figure 3.6: Strength of 10Sc1CeSZ, 3YSZ and 6ScSZ versus failure probability for different considered loaded surface areas at RT and 850°C. Also plotted are the respective points given in Figure 3.5.

3.5 Conclusion

(i) The change of strength of the tested zirconia compounds with temperature can be attributed solely to the change of the fracture toughness, so that any given RT strength can be translated into the respective strength at elevated temperatures.

(ii) The tetragonal zirconia compounds have similar monotonic temperature decay of their inert strength, while the cubic 10Sc1CeSZ shows a minimum at 450°C. The minimum of the inert fracture strain lies for all compounds at 850°C.

(iii) At 850°C SCCG does not affect the strength of these zirconia compounds, while 6ScSZ shows the greatest sensitivity at 450°C. Taking SCCG into account, the temperature behaviour of the strength becomes more complex and depends basically on the required lifetime of the component at each temperature it is exposed to. This also highlights the importance of the determination of the inert strength, as it is crucial to calculate the strength degradation and correspondingly the lifetime.

(iv) Based on the requirements associated with the operating conditions of the *Galileo 1000 N*, it was found that it is sufficient to assess the reliability of the tetragonal zirconia compounds just at the operating temperature, whereas for 10Sc1CeSZ at least the stress environment at RT has to be considered as well, since its fracture strain and stress was found to be lower at RT than at 850°C.

(v) Based on the strength data of a previous study, the overall stress levels that the electrolyte experiences while maintaining a level of reliability has to be limited between 100-200 MPa, depending on the specifics of the respective system, which appears feasible. It was further found that 10Sc1CeSZ can be regarded as competitive compared to 6ScSZ and 3YSZ.

(vi) The Ball-on-3-Balls bending test proves to be very suitable to characterise material specific properties such as the change of strength with temperature or the determination of the sub critical crack growth parameter, as it is very accurate and requires only small samples with a rectangular shape. Additionally any gaseous media can easily be applied during testing, to ensure a defined environment.

3.6 Acknowledgements

The authors would like to thank *R. Bächtold* and *U. Weissen* for the unconditional support. Furthermore, the funding of this work by the *Swiss Federal Office* of *Energy* under the contract no. 8100076; SI/500084-02 and by *Swisselectric Research* within the *SOF-CH-ESC* project is gratefully acknowledged.

3.7 References

[1] R. Danzer, T. Lube, P. Supancic, R. Damani, Advanced Engineering Materials, 10 (2008) 275-298.
[2] M. Radovic, E. Lara-Curzio, G. Nelson, Ceramic Engineering and Science Proceedings, 27 (2007) 373-381.
[3] W.M. Rainforth, F.L. Lowrie, R.D. Rawlings, Journal of the European Ceramic Society, 20 (2000).
[4] A.N. Kumar, B.F. Sorensen, Materials Science and Engineering, A333 (2002) 380.
[5] J. Alcala, M. Anglada, Materials Science and Engineering a-Structural Materials Properties Microstructure and Processing, 232 (1997) 103-109.
[6] A. Selcuk, A. Mercre, A. Atkinson, Journal of Materials Science, 36 (2001) 1173-1182.
[7] B.F. Sorensen, S. Primdahl, Journal of Materials Science, 33 (1998) 5291-5300.
[8] J. Malzbender, P. Batfalsky, R. Vaßen, V. Shemet, F. Tietz, Journal of Power Sources, 201 (2012) 196-203.
[9] J. Chevalier, L. Gremillard, A.V. Virkar, D.R. Clarke, Journal of the American Ceramic Society, 92 (2009) 1901-1920.
[10] M. Chen, Y.L. Liu, A. Hagen, P.V. Hendriksen, F.W. Poulsen, Fuel Cells, 9 (2009) 833-840.
[11] A. Nakajo, J. Kuebler, A. Faes, U.F. Vogt, H.J. Schindler, L.-K. Chiang, S. Modena, J. Van Herle, T. Hocker, Ceramics International, 38 (2012) 3907-3927.
[12] Y. Chen, A. Aman, M. Lugovy, N. Orlovskaya, S. Wang, X. Huang, T. Graule, J. Kuebler, Fuel Cells, 13 (2013) 1068-1075.
[13] F. Fleischhauer, M. Terner, R. Bermejo, R. Danzer, T. Graule, A. Mai, J. Kuebler, Journal of Power Sources 275 (2015) 217-226.
[14] J. Malzbender, R.W. Steinbrech, Journal of the European Ceramic Society, 27 (2007) 2597-2603.
[15] R. Clague, A.J. Marquis, N.P. Brandon, Journal of Power Sources, 221 (2013) 290-299.
[16] A. Nakajo, Z. Wuillemin, J. Van herle, D. Favrat, Journal of Power Sources, 193 (2009) 203-215.
[17] S.P.S. Badwal, F.T. Ciacchi, D. Milosevic, Solid State Ionics, 136-137 (2000) 91-99.
[18] N. Orlovskaya, S. Lukich, G. Subhash, T. Graule, J. Kuebler, Journal of Power Sources, 195 (2010) 2774-2781.
[19] S. Spinner, W.E. Tefft, Proceedings ASTM, 61 (1961).

[20] R. Danzer, P. Supancic, W. Harrer, Journal of the Ceramic Society of Japan, 114 (2006) 1054-1060.
[21] A. Börger, P. Supancic, R. Danzer, Journal of the European Ceramic Society, 22 (2002) 1425-1436.
[22] S. Giraud, J. Canel, Journal of the European Ceramic Society, 28 (2008) 77-83.
[23] T. Kushi, K. Sato, A. Unemoto, S. Hashimoto, K. Amezawa, T. Kawada, Journal of Power Sources, 196 (2011) 7989-7993.
[24] B. Lawn, Fracture of Brittle Solids, Cambridge University Press, Cambridge, 1993.
[25] M. Matsui, T. Soma, I. Oda, Journal of the American Ceramic Society, 59 (1986) 198-202.
[26] J.J. Mecholsky Jr, Materials Letters, 60 (2006) 2485-2488.
[27] J. Kuebler, U.F. Vogt, D. Haberstock, J. Sfeir, A. Mai, T. Hocker, M. Roos, U. Harnisch, Fuel Cells, 10 (2010) 1066-1073.
[28] F. Fleischhauer, A. Tiefenauer, T. Graule, R. Danzer, A. Mai, J. Kuebler, Journal of Power Sources, 258 (2014) 382-390.
[29] S. Strobl, P. Supancic, T. Lube, R. Danzer, Journal of the European Ceramic Society, 32 (2012) 1491-1501.
[30] S.R. Choi, in: D. Bray (Ed.) 22nd Annual Conference on Composites, Advanced Ceramics, Materials, and Structures: B, Amer Ceramic Soc, Westerville, 1998, pp. 293-301.
[31] D.L. Davidson, J.B. Campbell, J. Lankford, Acta Metallurgica Et Materialia, 39 (1991) 1319-1330.
[32] A. Mai, B. Iwanschitz, U. Weissen, R. Denzler, D. Haberstock, V. Nerlich, A. Schuler, in: S.C. Singhal, K. Eguchi (Eds.) ECS Transactions, 2011, pp. 87-95.
[33] A. Atkinson, A. Selcuk, Solid State Ionics, 134 (2000) 59-66.
[34] A. Nakajo, Z. Wuillemin, J. Van herle, D. Favrat, Journal of Power Sources, 193 (2009) 216-226.
[35] H. Severson, M. Assadi, Journal of Fuel Cell Science and Technology, 10 (2013).
[36] J. Laurencin, G. Delette, F. Lefebvre-Joud, A. Dupeux, Journal of the European Ceramic Society, 28 (2008) 1857-1869.

Chapter 4

STRENGTH OF AN ELECTROLYTE SUPPORTED SOLID OXIDE FUEL CELL

Journal of Power Sources 297 (2015) 158-167

Felix Fleischhauer[1,2], Raul Bermejo[2], Robert Danzer[2], Andreas Mai[1], Thomas Graule[3], Jakob Kuebler[3]

[1]Hexis Ltd., Zum Park 5, 8404 Winterthur, Switzerland

[2]Institut für Struktur-und Funktionskeramik, Montanuniversität Leoben, Peter-Tunner-Str. 5, 8700 Leoben, Austria

[3]Empa, Swiss Federal Laboratories for Materials Science and Technology, Laboratory for High Performance Ceramics, Ueberlandstr. 129, 8600 Duebendorf, Switzerland

Abstract

For the proper function of solid oxide fuel cells (SOFC) their structural integrity must be maintained during the whole lifetime. Any cell fracture would cause leakage and partial oxidization of the anode, leading to a reduced performance, if not catastrophic failure of the whole stack. In this study, the mechanical strength of a state of the art SOFC, developed and produced by the *Hexis AG*/Switzerland, was investigated with respect to the influence of temperature and ageing, whilst for the anode side of the cell the strength was measured under reducing and oxidising atmospheres. Ball-on-3-Ball bending strength tests and fractography conducted on anode and cathode half-cells revealed the underlying mechanisms, which lead to cell fracture. They were found to be different for the cathode and the anode side and that they change with temperature and ageing. Both anode and cathode sides exhibit the lowest strength at T = 850°C, which is greatly reduced to the initial strength of the bare electrolyte. This reduction is the consequence of the formation of cracks in the electrode layer which either directly penetrate into the electrolyte (anode side) or locally increase the stress intensity level of pre-existing flaws of the electrolytes at the interface (cathode side).

4.1 Introduction

Solid oxide fuel cells (SOFCs) are state of the art ceramic based components, to convert chemical energy of many different fuels into electrical energy. The electrical efficiency of the underlying electrochemical conversion process can reach up to 70%. One requirement for these high levels of efficiency is the physical separation of the fuel from the oxidizing air, through the gastight electrolyte. This ensures that the fuel is not directly burned off. Any kind of leakage reduces the amount of effectively utilizable fuel and therefore causes lower efficiency.

One way for leakage to occur in a SOFC system is when the electrolyte fractures and the gas tightness is no longer maintained. Hence the mechanical reliability of the electrolyte as part of the cell has to be ensured during the whole time of operation; including thermo and red-ox cycles.

One approach is to keep possible tensile stresses acting on the cell to a minimum. This can be done, for instance, by proper thermal management, in order to reduce the thermal stresses that are caused by inevitable thermal gradients over the cell area [1]. Another way is to select the electrodes and the electrolyte in a way, so that the strength of the cell and the corresponding reliability is sufficiently large. An overview over the mechanical properties of several gadolinia-ceria and zirconia electrolytes can be found in Ref. [2-4]. Beside the properties of the electrolyte, the robustness of the cell is further determined by the properties of the electrodes and their interphases or interfaces, respectively. In previous studies it has been reported that cracks within the electrodes may extend into the electrolyte, thus weakening its strength [5-7]. This damage process is either promoted by residual stresses or when an external tensile stress is applied to the electrode.

In the present study the robustness and the reliability of a state of the art electrolyte supported SOFC is investigated, which was provided by the *Hexis AG* (Winterthur, Switzerland). The cell is characterised by an initial power output of 22 W, when supplied with 4 g/h of partial catalytic reformed natural gas per cell (corresponds to 52 W), operated at 0.7 V cell voltage and 850°C. The steady state power degradation at a constant voltage operation is 0.7%/1000 h [8]. This cell is employed in the current *Hexis* μ-Combined-Heat-and-Power plant, the *Galileo 1000 N*. Further information about the stack and system is also given in Ref. [8]. Here the cell has to endure any given mechanical load being operated at 850°C, while being subjected to

reducing and oxidising atmospheres for up to 40'000 hours and several thermo redox cycles (on-off cycles). In order to take these different aspects into account, Ball-on-three-Balls (B3B) bending strength measurements have been performed on cathode and anode half-cell specimens covering the whole relevant temperature range from room temperature up to 850°C, whilst the anode half cells were tested either in their reduced or oxidized state. Possible ageing effects are investigated by testing half-cells obtained from cells, which were continuously operated for up to 12'000 hours.

4.2 Experimental

4.2.1 Specimens

The SOFC from Hexis consists of five layers as shown in Figure 4.1. The anode is a bilayer with a 30 µm thick current collector (A2) consisting of a porous NiO (70 wt.-%)-$Ce_{0.6}Gd_{0.4}O_2$ (30 wt.-%) cermet and a 10 µm thick functional layer (A1) comprised of the same cermet but with 50 % NiO content. The electrolyte is a dense 6 mol-% Sc_2O_3 stabilized ZrO_2, with a thickness of 160 µm. The cathode is again a porous bilayer with a 60 µm thick $(La_{0.78}Sr_{0.2})MnO_{3-\delta}$ current collector (C2) and a 15 µm thick functional layer (C1) comprised of a $(La_{0.78}Sr_{0.2})MnO_{3-\delta}$ (50 wt.-%)-Y_2O_3(8 mol%)-ZrO_2 (50 wt.-%) cermet.

The electrolyte is produced via a tape casting route. Therefore it possesses two surfaces, one which was in contact with the supporting foil, where it was cast onto and the opposite side, which was in contact with the doctor blade. As the supporting foil has a structured surface, the respective electrolyte exhibits a rougher topography than the other side of the tape after sintering. In order to study the influence of the different roughness, two different cells were investigated: a cell, where the anode was screen-printed onto the rough side, which marks the standard case and one where it was printed onto the smoother side.

The samples for the B3B bending tests were prepared by cutting the cells with a diamond wheel saw into 4 x 3 mm^2 rectangular plates, while gluing them onto a support foil. The cutting speed was adjusted, so that no cracking occurred at the samples edges, which was checked via light microscopy. Any possible effect of micro cracks, which might have not been detected and having a length smaller than 10 µm, is neglected, as the B3B bending test just loads the samples centre with tensile

stress, while the edges are compressed [9, 10]. Also, this way of sample preparation has been successfully applied to glass substrates, which are even more delicate to handle due to their low fracture toughness [11].

The actual testing was performed on half-cells, where both cathode layers of each specimen were gently polished off to obtain the anode half-cells and vice versa to obtain cathode half-cells (see Figure 4.1). The advantage of these samples is that it simplifies the stress analysis. Furthermore the potential uncertainties regarding the description of the elastic response of these heterogeneous multilayers, which is necessary for stress analysis, is reduced to minimum.

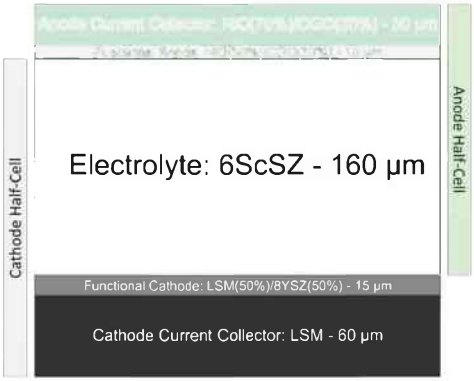

Figure 4.1: Principle architecture and composition of the Hexis SOFC.

4.2.2 Biaxial Bending Strength Testing

The biaxial strength was determined using the Ball-on-three-Balls (B3B) test [9, 10, 12], where plate like specimens can be tested in biaxial flexure. Details of the testing procedure can be found elsewhere [13]. For the testing of the 4x3 mm^2 sized specimens 2.2 mm balls were chosen. The three balls were arranged below the sample, supporting it, while the loading ball was on top of the sample as described in [3]. All tests were performed in a dry atmosphere in order to avoid possible sub

critical crack growth, as found in this type of material [4]. At room temperature (RT) tests were made in an argon atmosphere. Samples that should remain in their oxidized state were tested in a mixture of argon(80%)/oxygen(20%), while forming gas (5% H_2/95% N_2) was used to reduce two sets of anode half-cell samples. The first set was heat treated under forming gas and annealed for 2 h at 850°C. The strength tests were then conducted at room temperature applying an inert argon atmosphere. The specimens of the second set were reduced with forming gas prior to each individual test at 850°C for 20 min while being already placed in the B3B set up. Subsequently the gas flow was upheld to maintain the reduced state during the actual testing. Thermogravimetry was used to ensure that the anode is completely reduced after 20 min, by measuring the relative mass loss of the two respective anode powders while being exposed to forming gas at the respective temperature. The displacement speed of the test rig was in general set in a way, so that fracture occurred in less than 4 seconds. The thicknesses of the electrodes and the electrolyte were determined optically from the edges of the cut specimens with an accuracy of ± 2 µm.

4.2.3 Stress calculation for half-cells subjected to B3B bending

4.2.3.1 Half-cells with pure elastic deformation until fracture

In order to calculate the fracture stress of any layer of a multi-layered elastically heterogeneous plate loaded in the B3B set up, it is necessary to describe the stress state as a function of the height coordinate z for a given applied load. For the general case of a multilayer being subjected to a bending moment M perpendicular to its stacking direction, *Hsueh* et al. presented a closed form solution. Here the first principal stress σ becomes a function of two effective constants describing the elastic response of a given multilayer and reads [14, 15]:

$$\sigma_i(z) = \frac{E_i\,(z - z_n^*)\,M}{\left(1 - \nu_i^2\right)D^*} \tag{4.1}$$

with the index i referring to the i-th layer (1 = electrolyte, 2 = first functional electrode layer, 3 = current collector layer), the respective Young's modulus E and Poisson ratio ν, z being the height coordinate of the whole stack. D^* is the effective

plate constant and describes the flexural rigidity of the multi-layered plate and z_n^* gives the height of the neutral bending plane, which might significantly vary from the central plane of the specimen. The method for calculating these can be found in [14, 15] as well.

The applied moment M can be generally calculated from the maximum of the first principal stress [16]:

$$M = \sigma_{max} \frac{t^2}{6} \tag{4.2}$$

For the B3B bending this stress is described as [10]:

$$\sigma_{max} = \frac{L}{t^2} C' \tag{4.3}$$

with C' being the respective pre-factor for the B3B test and L the applied force. Inserting Equation (4.3) into (4.2), the moment becomes just a function of L and C', so that Equation (4.1) can be written as:

$$\sigma_i(z) = \frac{E_i\,(z - z_n^*)\,L}{6\left(1 - \nu_i^2\right)D^*}\,C' \tag{4.4}$$

For the 4x3 mm² rectangle specimens C' was determined via a finite-element model of this specific test rig. The principle approach and model was previously published by *Danzer* et al. [12]. Based on this analysis the pre-factor is here calculated according to:

$$C' = 0.21427 + \frac{\left((2.914 + 9.96\ mm^{-1}\ t_{el} - 4.65\ mm^{-2}\ t_{el}^2\right)(1 + 0.939\ \nu)}{1 + 9.63\ mm^{-1}\ t_{el}} \tag{4.5}$$

Since only the maximum stress in the electrolyte is of interest in the present study, t_{el}, the thickness of the electrolyte, is taken into account.

For the fracture stress evaluation based on Equation (4.1) the effective constants D^* and z_n^* have to be determined. For any bending test, it can be assumed that the load-displacement curve is proportional to the flexural rigidity of the plate, which is expressed by its plate constant [16]. Hence the load displacement curves of different dense zirconia plates with known plate constant [3] have been plotted in order to

obtain the proportionality factor K for the test rig used. It is given in Figure 4.2. As the electrodes may have cracks, large pores or other inhomogeneities, which result from the manufacturing process, their Young's moduli were not taken from literature but have been chosen, so that the median plate constant fits the measured median force-displacement slope of each tested sample set. As it is not possible to resolve the differences between the two electrode layers, the ratio between their Young's moduli has been chosen to correspond to the one published in [17]. For all electrode layers the Poisson's ratio is set to be $\nu = 0.3$. This is only an estimate but a consequence of the inconsistent literature data, of which an overview is found in [2]. Based on these Young's moduli and this Poisson's ratio the position of the neutral bending plane is calculated as well.

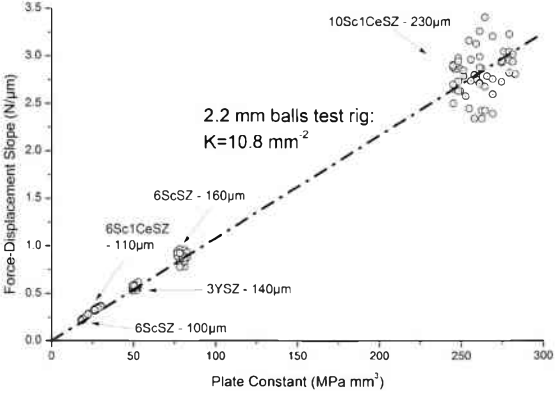

Figure 4.2: Correlation between the force-displacement-slope and the plate constant based on the measurement of zirconia samples with 4x3 mm² in size and different thickness taken for the test rig with balls of 2.2 mm in diameter.

4.2.3.2 Half-cells with delaminating electrode layer prior to fracture

In the case of local delamination, the plate constant does not describe the elastic behaviour of the sample anymore, as the neutral bending plane underneath the delaminated electrode is shifted towards the middle plane of the electrolyte as sketched in Figure 4.3. Assuming that at the fracture site this shift is complete, the electrolyte can now be treated locally as being elastically disconnected from the anode at the moment of fracture. However, the locally acting bending moment and the corresponding fracture stress cannot be derived from the applied force, since the force flow is distributed over the whole sample, which is now an ill-describable heterogeneous system.

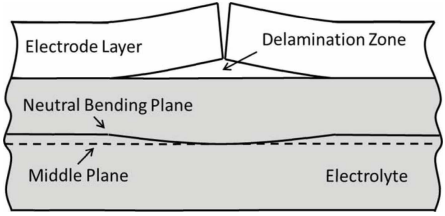

Figure 4.3: Sketch (cross-section) of the shift of the neutral bending plane of an electrolyte as part of a half-cell subjected to pure bending underneath a locally delaminated electrode layer.

The here presented approach is based on following idea. If at the point of fracture the electrolyte is decoupled from the anode it has to be able to sustain the same deflection as if it were uncoated. Hence, instead of taking the measured force, the corrected displacement at the moment of fracture is used in order to calculate an equivalent fracture force L_{eq}, which relates the coated sample with an uncoated one. Knowing the thickness of the electrolyte and its elastic constants, the plate constant of the assumedly bare electrolyte is calculated. Via the plate constant and together with the proportionality factor K (not to be confused with the stress intensity factor K_I) derived from Figure 4.2, the equivalent force displacement slope is obtained, so that the measured and corrected displacement can be converted into the corresponding equivalent fracture force. Equation (4.3) gives then the fracture stress in the electrolyte. In order to reduce the uncertainty regarding the measured

displacement, the pre-load prior to the test is minimised and set to 0.1 N. After correcting the load displacement curve regarding the compliance of the test rig and the load cell the lower region of the measured curve between 1 and 5 N was linearly extrapolated towards zero load. The so obtained displacement is then considered as the point of zero displacement. Any sample, which did not show a continuous load-displacement curve, was disregarded.

4.3 Experimental results and discussion

4.3.1 Anode half-cells

4.3.1.1 Strength at RT

Since – as mentioned above – the electrolyte has a different surface quality at the top and botten side, it can be speculated that the strength of both sides may be different. Therefore the biaxial bending strength of the electrolyte has been determined at RT under inert conditions for samples being 4x3 mm^2 in size with either the smooth (R_{rms} = 0.13 µm, doctor blade side) or the rough surface (R_{rms} = 0.9 µm, supported side) of the electrolyte at the interface tensile loaded side of the specimens. The respective strength distributions are displayed in a Weibull plot shown in Figure 4.4, where the strength of each specimen is ranked in an ascending order, assigning then every value a failure probability of $F = (j\text{-}0.5)/n$. j refers to the ranking position and n to the sample set size. Any given Weibull modulus is calculated according to *EN 843-5 (2006)* standard. The elastic paramertes used for the stress calculation are given in Table 4.1. The Weibull parameters decribing the strength distribution are given in Table 4.2.

The bare 6ScSZ electrolyte has at its rough side a characteristic strength of σ_0 = 1379 MPa and at its smooth side σ_0 = 2017 MPa while both sides show a Weibull modulus close to $m \cong 20$ [3] (note that the "smooth" side here is referred to as "dull" in the reference). Comparing these stress levels with the one shown in Figure 4.4, it becomes apparent, that the strength of the electrolyte on the cell level is greatly reduced. It is further interesting to note that the two sides of the electrolyte now show a similar strength, already indicating that a different failure mechanism is correlated to the presence of the anode.

Table 4.1: Elastic constants used for the fracture stress calculation of all tested anode half-cells. The values given in the brackets correspond to the standard deviation of the measured parameter.

T	A1	A2	6ScSZ**	
(°C)	E (GPa)	E (GPa)	E (GPa)	ν
25	40 (±5)	30 (±4)	213.6	0.32
250	39*	29*	194.2	0.28
450	39*	27*	156.2	0.30
650	38*	26*	155.0	0.37
850	37*	25*	160.1	0.34
950	37*	24*	164.2	0.33

*estimated by taking the temperature dependency of the A1 and A2 given in Ref. [17] for RT and T = 950°C assuming a linear behaviour
**taken from Ref. [4]

Table 4.2: Compilation of Weibull parameters for all unaged sample sets tested in this study including the 90% confidence intervals.

Samples	Tested Interface/Surface	Temperature T (°C)	Characteristic Strength σ_0 (MPa)	Weibull modulus m
Anode Half-Cells/oxidized	smooth	RT	786 (806|767)	13.3 (17.1|10.3)
	rough	RT	840 (859|821)	9.7 (11.5|8.3)
		250	621*	35*
		450	508 (517|501)	32 (46|22)
		650	407 (414|402)	36 (57|23)
		850	335 (341|329)	25 (36|18)
Anode Half-Cells/reduced	rough	RT	1164 (1188|1141)	19 (26|14)
		850	698*	20*
Cathode Half-Cells	smooth	RT	2015 (2055|1975)	16 (21|13)
		850	499 (524|475)	9.4 (13.5|6.6)
Electrolyte**	rough	RT	1379 (1404|1354)	18 (22|14)
		850	511 (519|502)	18 (23|15)
	smooth	RT	2017 (2050|1985)	20 (25|16)
		850	822 (853|794)	19 (29|11)

*Estimated from the lower branch of the measured specimens
**Taken from earlier studies [3, 4]

It was previously reported that the here investigated anodes tend to form a channel crack network as the anode is not robust enough to sustain the residual tensile stress, which originates form the differences in thermal expansion coefficients between the anode and the electrolyte material after cooling down from the sintering temperature of $T_{sinter,anode}$ = 1210°C [18]. This is also the case for the here tested samples as can be seen in Figure 4.5a). It has been already observed that these channel cracks are able to act as the main flaw, as they extend into the electrolyte

and thus weaken its strength [5, 6]. Figure 4.5b) shows a characteristic fracture origin site, where the crack runs straight through the anode and the electrolyte, without any sign of delamination at the interphase. The fracture initiation site is hereby identified by the orientation of the ripples on the fracture surface, which run perpendicular to the former crack front and converge at the origin. Microscopy reveals that a 2 μm thick interphase within the electrolyte has formed. This interphase forms due to the diffusion of CGO into the zirconia substrate [19, 20]. The interphase displays a transition from a transgranular to intergranular fracture (see Figure 4.5c), indicating that the fracture toughness is significantly reduced. This explains why the strength between samples with rough and smooth interphase is rather small if not negligible, since a crack in the anode will expand sub critically into the low toughness region of the electrolyte creating a new kind of fracture dominating flaws which are independent of the already pre-existing flaws at the interface of the electrolyte.

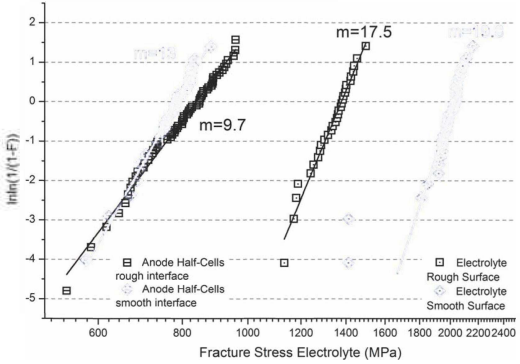

Figure 4.4: Weibull plot of the maximum principle stress within the electrolyte when fracture occurs for different anode- half-cells at RT including the respective Weibull modulus.

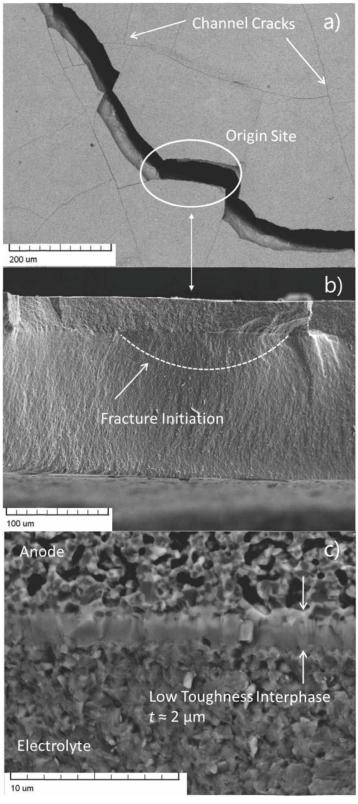

Figure 4.5: a) On-top view of the fracture origin site of a fractured anode half-cell with rough electrolyte anode interphase; b) Corresponding fracture surface of a) with fracture origin site of an anode half-cell with rough electrolyte anode interphase; c) Detail of the fracture surface showing the low toughness interphase at a fracture origin site of an anode half-cell.

4.3.1.2 Strength at elevated temperatures

SOFCs are operated at elevated temperatures, it is thus of interest to investigate how the strength of these anode half-cells develops with increasing temperature. As the accuracy of the determination of the respected Youngs moduli decreases at elevated temperatures, the values at elevated temperatures are estimated from the RT constants by taking the temperature dependency of the A1 (RT: 65 GPa, 950°C: 60GPa) and A2 (RT: 50 GPa, 950°C: 40 GPa) given in Ref. [17] assuming a linear behaviour. They are given in Table 4.1, while the respective Weibull parameters are given in Table 4.2.

Figure 4.6 shows the evolution of the strength distribution of the anode half-cells tested from RT up to 850°C. The strength steadily decays with increasing temperature. The scatter of the strength however undergoes a change from a low Weibull modulus of m = 9.7 towards a significantly higher modulus of m = 25 or even greater at temperatures larger or equal to 450°C. At 250°C the transition is clearly visible in the form of a kink in the distribution of the individual ascendingly ordered strength values. The reason for this transition remains so far unclear and could not be resolved by fractography alone. However, it must be related to the temperature evolution of the fracture toughness as it determines how easily the anode channel crack can penetrate into the electrolyte.

The change in the strength distribution is also accompanied by a change in the crack formation, which is revealed by the different force-deflection curves recorded during the single fracture tests. Figure 4.7 shows a selection of these curves (as recorded) measured at RT and 850°C. At 850°C the fracture does not happen instantaneously, but is characterised by plateau formation, where the critical flaws grow at a constant applied force until reaching a critical size.

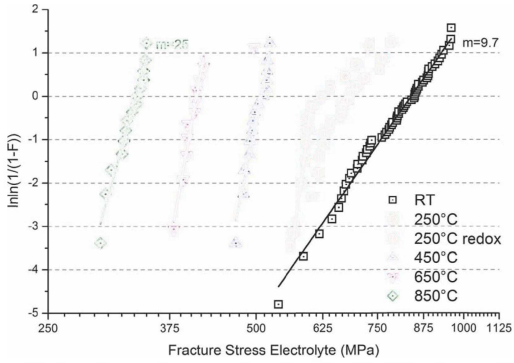

Figure 4.6: Weibull diagram of the fracture stress distribution of the electrolyte as part of a anode half-cell with the rough interphase for varying temperatures. Also shown is the strength distribution at 250°C after exposing the samples to one redox-cycle.

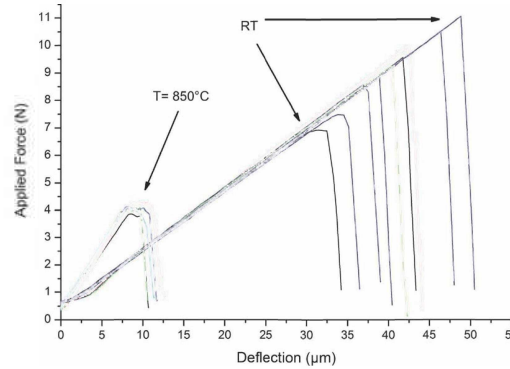

Figure 4.7: Selection of force-deflection curves for anode half-cells tested at RT and 850°C.

At RT the fracture of the stronger specimens occurs in a single event, while already for the weakest samples also a plateau formation can be observed. Together with the kink found for the samples tested at 250°C and the single runaway value at 650°C it can be concluded, that the probability, at which this transition happens, is increased with temperature. It can be speculated that also at RT such a transition could be observed at a certain strength level if a sufficient number of specimens would be tested. As a consequence the found distribution with a Weibull modulus of m = 9.7 would have a limit and will turn into a distribution with a higher modulus. This limit might be even at a lower strength level than shown for the 250°C data, as the residual stress is at RT at its maximum, while the toughness does not further increase [4]. To demonstrate this effect, further experiments would be necessary, which is out of the scope of this investigation.

4.3.1.3 Strength of the reduced anode half-cells

Most of the operating time, the anode is in its reduced state. Due to the reduction, the mechanical properties change and thus a change in the fracture strength can be expected and has to be investigated. The results of the strength tests are shown in Figure 4.8, while the respective Weibull parameters describing the strength distribution are given in Table 4.2. Fractography reveals that the anode gradually delaminates off the electrolyte at the zone, where the local stress maximum is applied to the sample (shown in Figure 4.9a) and b)). This is confirmed by the non-linear relationship between force and the corrected (true) displacement, where the force-displacement-slope decreases while increasing the applied force. This indicates an irreversible change in the samples stiffness, which correlates to the delamination process. Hence, the fracture stress in the electrolyte is calculated according to the approach developed in Section 4.2.4.2.

At RT the maximum stress at fracture of the electrolyte being part of the reduced anode half-cell is significantly increased compared to the samples being in their oxidised state. As the anode delaminates its cracks are no longer able to penetrate into the electrolyte but they are deflected to follow the interphase between electrolyte and anode. Therefore, the strength in this case depends on the strength of the electrolyte itself. The strength distribution is characterised by an increased Weibull modulus of m = 19, which is close to the one of the bare electrolyte, while the

characteristic strength of $\sigma_{0,anode,red} = 1088$ MPa is lower compared to $\sigma_{0,electrolyte} = 1379$ MPa of the bare electrolyte and its corresponding surface. This decrease can be explained by the low toughness interphase, which remains at the surface after the delamination of the anode. It effectively increases the size of any surface flaw by 2 µm. Following the definition if the stress intensity factor [21], the critical flaw size $a_{c,0}$ can be expressed as a function of the fracture stress σ_0:

$$a_{c,0} = \frac{K_{Ic}^2}{\sigma_0^2 Y^2 \pi} \tag{4.6}$$

Now, the difference in the characteristic strength, applying a geometric factor $Y = 0.85$ [3] and the fracture toughness of 6ScSZ $K_{Ic} = 4.1$ MPa $m^{½}$, results according to Equation (4.6) in a difference in the flaw size of $\Delta a_{c,0} = 2.36$ µm, which fits very well the observation. A potential change of the strength of the electrolyte, because of it being reduced, is neglected, as *Hashida* et al. [22] found the strength of zirconia to be independent of reduction.

In order to measure the strength of the anode half-cells in their reduced state at 850 °C, each specimen while being already placed in the test rig was subjected to constant flow of forming gas 20 min prior to and during the test. The 20 min were chosen due to the results of the thermogravimetry. The load-displacement curves were again linear and the anode showed no delamination (see Figure 4.9c)), hence the maximum applied stress within the electrolyte was calculated according to Equation (4.4). The Young's moduli for the two reduced anode layers were estimated from the slopes of the load displacement curves to be $E_{A1} = 30 \pm 15$ GPa and $E_{A2} = 20 \pm 10$ GPa analogue to the ones taken for the analysis of the oxidised samples. The large uncertainty is a consequence of the comparably large scatter of the slopes but leads to a systematic error in the stress analysis of only ± 73 MPa. The respective distribution is shown in Figure 4.8 and compared to the one of the oxidised samples. Despite the observation that the anode did not delaminate before or during fracture, the maximum applied stress within the electrolyte is increased remarkably and even exceeds the one of the corresponding rough side of the bare electrolyte.

As for the oxidised sample the crack is formed underneath a pre-existing channel crack, as is shown in Figure 4.9c). However, in the case of the reduced samples the

crack origin is not the channel crack itself in combination with the low toughness interphase but a flaw within the electrolyte, which requires an unexpectedly large stress to become critical. Two aspects are so far unknown to explain this finding. First, it is unclear how the low toughness interphase layer is affected by the reducing atmosphere, whether it shrinks or expands. Second, it is also unclear, whether the shrinking NiO or the expanding CGO is dominating the overall behaviour of the anode and thus whether the anode tends to become compressed or stretched. It exceeds the scope of this study to investigate these material features as the main focus here is set upon a strength evaluation in order to discuss the reliability of the overall fuel cell. However, as these issues are of relevance for the design of future fuel cells, they will be addressed in a subsequent article.

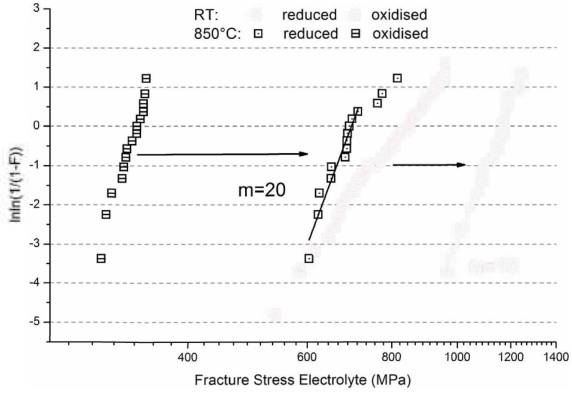

Figure 4.8: Comparison of the strengh distribution of the reduced and oxidised anode half-cells at RT and T = 850°C including the Weibull modulus of the reduced anode half-cells.

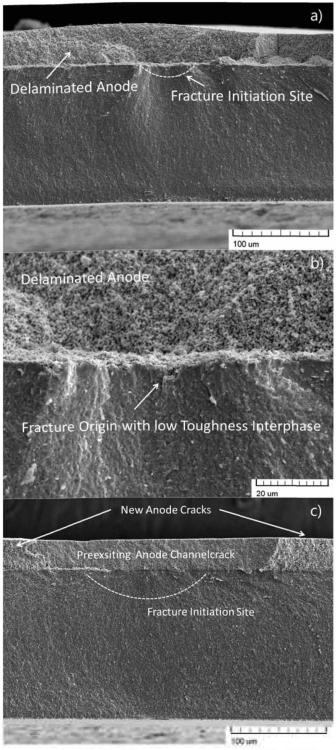

Figure 4.9: a) Fracture surface at the fracture initiation site showing the delaminated anode of an reduced anode half-cell tested at RT; b) Magnified fracture origin of a) showing the delaminated anode above the origin and the origin surrounding low toughness interphase; c) Fracture surface at the fracture initiation site of an reduced anode half-cell tested at T = 850 °C. The fracture origin is located underneath a pre-existing channel crack. The path of the expanding crack is independent of the pre-existing channel crack as it runs straight through the electrolyte, creating new cracks in the anode.

4.3.2 Strength of cathode half-cells

Analogue to the anode half-cells the strength of the cathode half-cells was tested as well, in order to gain a comprehensive picture on the overall cell strength. The results of the strength tests are shown in Figure 4.10, while the corresponding Weibull parameters are given in Table 4.2. At RT the maximum applied stress within the coated electrolyte is similar to the uncoated one. Fractography reveals that as in the case of the reduced anode half-cells the cathode tends to delaminate (see Figure 4.11a)), which is also recognised by a decreasing force-displacement slope as the applied force approaches fracture. As no distinct interphase layer is observed, the electrolyte underneath the delaminated cathode displays the same strength as the respective side of the bare electrolyte.

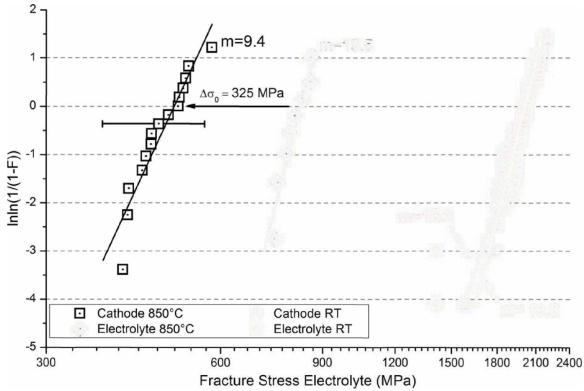

Figure 4.10: Comparison of the strength distribution of the cathode half-cells tested at RT and T = 850 °C with the one of the respective bare electrolyte including the Weibull moduli of each sample set. Also exemplarily shown is the 90% confidence interval of the median strength value of the cathode half-cells at T = 850°C due to the large uncertainties regarding the elastic parameter of the cathode layers. Furthermore the median strength is estimated based on the assumption that prior to fracture a cathode crack was formed.

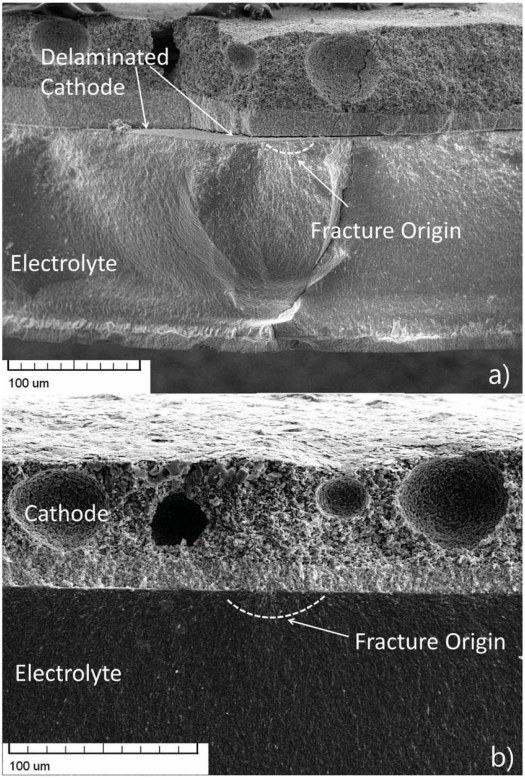

Figure 4.11: a) Fracture initiation site of a cathode half-cell tested at RT showing the delaminated cathode; b) Fracture origin of a cathode half-cell tested at T = 850°C.

At the operating temperature however no cathode delamination and a drop in the strength was observed (see Figure 4.10 and 4.11b)) so that the half-cells' fracture stress was again calculated according to Equation (4.4). The Young's moduli of the two layers was set to be E_{K1} = 16 GPa and E_{K2} = 24 GPa keeping the ratio of the already published values [17], while dealing with a relative standard deviation of ± 23% due to the large scatter of the force-displacement-slopes at T = 850°C. Keeping the Young's moduli within the 90% confidence interval (corresponds to a relative variation of ± 38%), gives a systematic error for every strength value of ± 20%. Despite this great uncertainty, a significant drop in strength is observed, compared to the strength of the respective side of the bare electrolyte, which is accompanied by an increased scatter, expressed by the decreased Weibull modulus.

The following fracture mechanism is proposed in order to explain this discrepancy. Prior to cell fracture a single crack forms in the cathode layer at the sample's centre, where the maximum tensile stress is built up. It expands then down to the substrate interface. The pre-cracking of the cathode is simply a consequence of its much lower strength compared to the electrolyte [23]. As this crack only forms locally its effect on the sample's stiffness is negligible and thus not recognisable in the force displacement curve, which still shows a constant slope between force and displacement until fracture (compare with the force-displacement curves of the oxidised anode half-cells tested at RT, shown in Figure 4.4b)). According to *Ye* et al. [24] this stressed crack will contribute to the stress intensity acting on a stressed surface or near surface flaw within the electrolyte, which is located underneath the electrode crack. Due to this contribution the fracture stress of the electrolyte as part of the cathode half-cells is reduced compared with the respective side of the bare electrolyte.

Additionally the large pores within the current collecting layer of the cathode may explain the increase in scatter. As the cathode is bent, these pores are weak spots and presumably act as origins, where the crack in the cathode layer is initiated. While the crack front expands and reaches out towards the electrolyte its stress intensity factor varies with the occurrence of pores within its flanks. A large pore hereby reduces significantly the stiffness of the cathode leading to a locally reduced stress intensity factor in comparison to a region of the cathode crack with no pores. This stress intensity factor distribution along the path of the crack is superimposed by the distribution of flaws at which the crack has to renucleated in the electrolyte.

The superposition in principle will cause an increase in scatter and decrease of the Weibull modulus, as described in Ref. [25] for the case of superimposing a distribution in form of measurement uncertainties. However the magnitude of this effect and its quantitative influence on the Weibull modulus for this special case remains unclear.

4.3.3 Ageing

In order to investigate how ageing might affect the cell strength, two cells, which were continuously operated for eight and twelve thousand hours at a temperature of T_{op} = 850°C, respectively and a 6ScSZ electrolyte, which was annealed for more than eleven thousand hours at T = 900°C, were tested at RT. Figure 4.12 compiles the respective characteristic strength including the 90% confidence intervals and compares them to the initial values. The bare electrolyte, with its rough side being tested shows no significant signs of ageing and retains its initial strength as well as its relatively large Weibull modulus of $m \approx 20$.

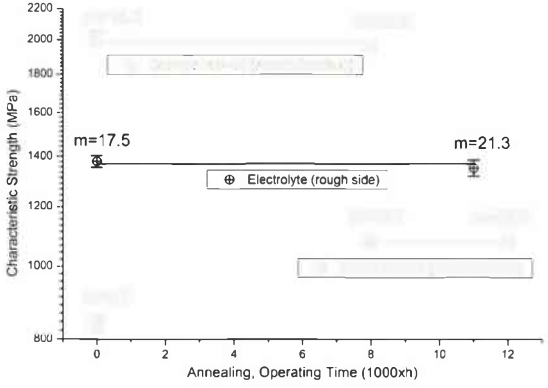

Figure 4.12: Compilation of the characteristic strength including the Weibull modulus of the aged electrolyte and the operated fuel cells together with the corresponding initial strength and the respective 90% confidence intervals.

This behaviour is also observed for the cathode half-cells. As described in the previous section, at RT the cathode tends to delaminate, rather than introducing potential cracks into the electrolyte. Hence, the strength of the cathode half-cell is determined by the strength of the smooth side of the electrolyte. Also for the aged samples this delamination process is observed. Therefore, it is conclusive that just like the electrolyte itself the strength of the cathode half-cell is also not significantly affected by prolonged operation.

Compared to the cathode half-cells, the anode half-cells even increase their strength. This is because after the continuous operation of several thousand hours the anode starts to delaminate as well. It is no longer able to introduce its channel cracks into the electrolyte. Henceforth, the strength is determined by the electrolyte and again does not further change with the operating time. The difference between the strength of the rough side of the electrolyte as part of the anode half-cell compared to the one of the bare electrolyte is explained by the remaining low toughness interface (see Figure 4.13), as it has been found already and discussed for the half-cells with the reduced anode in Section 4.3.1.3. Interestingly the low toughness interphase remains unchanged maintaining its initial thickness of 2 µm, as shown in Figure 4.13. Therefore, the strength of the aged anode half-cell is equal to the strength of the non-aged reduced one.

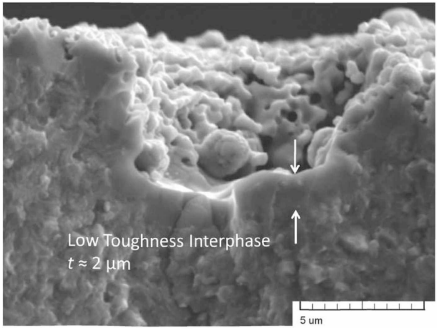

Figure 4.13: Fracture origin of an anode half-cell being operated for 8000 hours and tested at RT with delaminated anode and low tougness interphase.

4.4 Consequences for stack behaviour and stack design

The Hexis state of the art SOFC was measured regarding its mechanical strength, in particular with regard to the fracture strength of the electrolyte upon which the whole cell integrity depends. The strength was characterised with respect to the influence of the cathode and anode layers at varying temperatures, atmospheres and ageing times. Within the considered parameter range the cell strength underlies several fracture mechanisms. Some might drastically reduce the electrolyte strength and hence the cell strength.

To function properly, the mechanical integrity of the cell has to be maintained throughout the whole operating time including several thermo- and redox-cycles. Based on the carried out measurements it is possible to identify the states at which the cell is weakest. The anode half-cell shows its lowest strength when it is oxidized and subjected to temperatures close to the operating point. At lower temperature its strength rises as the effect of the increasing toughness of 6ScSZ overweighs the increasing residual stresses. In a reducing atmosphere a drastic increase in strength was observed. The results from the ageing experiments and the tested sample set being exposed to one complete thermo-redox-cycle and measured at $T = 250°C$ (see Figure 4.6 indicate that the anode suffers over time and while being cycled from mechanical degradation, leading to a reduced interfacial toughness between anode and electrolyte, which affects the strength of the cell in a positive way. Hence an unaged anode half-cell possesses the lowest mechanical strength. As the crack initiating flaw is found to be the low toughness interphase it is hereby of less importance whether the anode is printed on the weaker or stronger side of the electrolyte.

The cathode half-cell is also found to be weakest at elevated temperatures, being weakened due to the local cracking of the cathode layer exerting additional contributions to the stress intensity factor on flaws within the electrolyte. At RT the cathode tends to delaminate, so that the strength of the cell just depends on the original electrolyte strength. At which temperature this transition between the two fracture mechanisms happens has not been resolved. However, it can be assumed that the lowest strength is to be found, where the electrolyte exhibits its lowest fracture toughness. Considering the temperature range the cell is subjected to, the lowest strength is therefore expected to be at operating temperatures. For the fracture mechanism found for this temperature, it would make a difference whether

the cathode is printed on the stronger or weaker side of the electrolyte. As the cracked cathode just amplifies the stress intensity of a pre-existing flaw within the electrolyte, the side with the greater flaws would naturally display a lower strength. Based on the current cell it is therefore preferential to print the cathode on the stronger side of the electrolyte, as it would make no difference for the anode. The results from the ageing experiments suggest that interdiffusion between the LSM and the electrolyte does not affect locally the toughness of 6ScSZ. This indicates that the strength of the cathode half cells at operating temperatures is not decreasing.

So far just the inert strength of the fuel cell has been discussed. Like in the case of a bare electrolyte, the strength of the cell is also influenced by humidity induced sub-critical crack growth (SCCG). As the failure of the cell depends just on the crack propagation within the electrolyte, the same crack growth parameters published by *Fleischhauer* et al. [3, 4] have to be applied. For the typical operation of a fuel cell it was reported that the lowest strength of the electrolyte is at temperatures greater than 800°C where no SCCG of zirconia is observed even if SCCG at lower temperatures is considered. In order to evaluate whether this is also true on the cell level, the basic equation of SCCG is considered, which relates the growth rate of a flaw da/dt with the total stress intensity factor $K_{I,total}$ in the form a Paris law [26]:

$$\frac{da}{dt} = v_0 \left(\frac{K_{I,total}}{K_{Ic}}\right)^n \tag{4.7}$$

In the case of a bare electrolyte (Case I) $K_{I,total}$ is proportional the root of the crack size a of a flaw within the electrolyte and the applied stress $\sigma_{electrolyte}$ acting on it [27]:

$$K_{I,total} = K_{I,electrolyte} \sim \sigma_{electrolyte}\sqrt{a} \tag{4.8}$$

In the case of a half-cell (Case II), where stress intensity of a flaw the size a within the electrolyte is amplified by a crack in the electrode layer (as for the cathode and oxidized anode half-cells at elevated temperatures), $K_{I,total}$ is the sum of the contribution of the directly applied stress $K_{I,electrolyte}$ as in Case I and a second term representing this additional stress intensity factor $K_{I,electrode}$. According to *Ye* et al. this contribution can be expressed as [24]:

$$K_{I,electrode} \sim \sigma_{electrode} \sqrt{\omega a} \tag{4.9}$$

with the mean applied stress in the electrode layer $\sigma_{electrode}$ acting on the crack next to the stress being applied to the electrolyte $\sigma_{electrolyte}$ and a function ω of the crack size a with the property $d\omega/da \leq 0$.

In the case of SCCG and according to Equation (4.7) and Relation (4.8) crack growth promotes itself. This is because $K_{I,total}$ grows with the crack size a (see Relation (4.8)) while the crack growth rate da/dt increases with $K_{I,total}$ (Equation (4.7)). To decide whether a half-cell is subject to more severe or a reduced crack growth compared to the bare electrolyte, $dK_{I,total}/da$ has to be considered. For $K_{I,electrolyte}$ holds:

$$\frac{dK_{I,electrolyte}}{da} > 0 \tag{4.10}$$

The opposite holds for $K_{I,electrode}$:

$$\frac{dK_{I,electrode}}{da} \leq 0 \tag{4.11}$$

Hence:

$$\frac{dK_{I,total}}{da}(Case\,I) \geq \frac{dK_{I,total}}{da}(Case\,II) \tag{4.12}$$

as $dK_{I,total}/da$ for Case II contains a contribution from $dK_{I,electrode}/da$. Therefore, it can be concluded that these half-cells show less pronounced subcritical crack growth, so that as for the bare electrolytes also for the considered half-cells SCCG will not lead to a lower strength at $T < 850°C$ than at $T = 850°C$. So the cathode and anode half cells have their strength minimum even in a humid SCCG promoting atmosphere at operating temperature.

Based on the above analysis the parameter with greatest potential can be identified, in order to optimise the cell strength. It has been revealed that a weak interface between electrode and electrolyte is beneficial with regard to its mechanical behaviour. In the case of electrode delamination the cell strength just depends on the electrolyte strength. This can be achieved by reducing the sintering temperature or additional surface treatment. If this is not achievable other parameters are the

Young's moduli of the electrode layers and their thickness. A reduction at this point would in accordance with Equation (4.4) also reduce the stress within the film and thus the corresponding stress intensity factor (see Relation (4.9)). The Young's modulus can directly be controlled by the relative pore content of the electrodes. For the anode a reduction of the sintering temperature would further reduce the width of the low-toughness interphase and hence the flaw size. A reduction of the thermal mismatch is less beneficial, because residual stresses are of less importance as the lowest strength is found at elevated temperatures, anyway. In principle an increase of the toughness of the electrolyte is always beneficial to the strength. However, 6ScSZ already belongs to the comparably tough electrolytes which provide sufficient ionic conductivity.

4.5. Conclusion

(i) The cell is weakest at its anode side at temperatures close to the operating temperatures (850°C), which are common for SOFC systems with electrolyte supported cells. At these conditions the anode is in its oxidized state. Hereby, the minimum strength is not further decreased due to ageing or sub critical crack growth. This result is in accordance with the failure analysis performed on these cells published by *Fleischhauer* et al. [18], where no correlation between operating time and the amount of fractured cells was found. It was further suggested that the fracture initiating event must have happened during the first shut-down process, when the cell gets oxidized.

(ii) The weakening mechanism is attributed to the penetration of a crack from the anode into the electrolyte (anode channel crack). This is assisted by the formation of a low toughness interphase between CGO of the anode and the 6ScSZ electrolyte.

(iii) The cathode is at operating temperatures weakened by a similar mechanism. The formed cathode crack however does not penetrate into the electrolyte but causes an increase of the stress intensity factor for already existing flaws within the electrolyte, hence a reduced strength is observed. The cathode strength hereby remains above the anode one, so that this side shows to be the stronger one of the cell. It is also not further reduced due to ageing.

(iv) Given a certain stress environment during operation the cell will either crack at the beginning of its history of operation or maintain its structural integrity throughout the whole lifetime.

(v) As the strength minima of cathode and anode are at elevated temperatures, residual stresses are found to be negligible. It was shown for the anode half cells that even at low temperatures their contribution to the fracture stress is comparably low, as an increased stress level in the anode is partially compensated by the compressive stress within the electrolyte at the interface.

(vi) A lower Young's modulus and a reduced thickness of the electrodes have been identified to increase the cell strength. The ultimate improvement would be the decreasing interfacial toughness so that an electrode crack gets deflected at the interface rather than penetrating into the electrolyte. All discussed measures however interact directly with the electrochemical performance of the cell.

4.6 Acknowledgements

The authors would like to thank *R. Bächtold* and *U. Weissen* for the unconditional support. Furthermore, the funding of this work by the *Swiss Federal Office of Energy* under the contract no. 8100076; SI/500084-02 and by *Swisselectric Research* within the *SOF-CH-ESC* project is gratefully acknowledged.

4.7 References

[1] A. Nakajo, Z. Wuillemin, J. Van herle, D. Favrat, Journal of Power Sources, 193 (2009) 203-215.
[2] A. Nakajo, J. Kuebler, A. Faes, U.F. Vogt, H.J. Schindler, L.-K. Chiang, S. Modena, J. Van Herle, T. Hocker, Ceramics International, 38 (2012) 3907-3927.
[3] F. Fleischhauer, M. Terner, R. Bermejo, R. Danzer, T. Graule, A. Mai, J. Kuebler, Journal of Power Sources 275 (2015) 217-226.
[4] F. Fleischhauer, R. Bermejo, R. Danzer, T. Graule, A. Mai, J. Kuebler, Journal of Power Sources, 273 (2015) 237-243.
[5] A. Selcuk, A. Merere, A. Atkinson, Journal of Materials Science, 36 (2001) 1173-1182.
[6] B.F. Sorensen, S. Primdahl, Journal of Materials Science, 33 (1998) 5291-5300.
[7] B.F. Sorensen, H. Toftegaard, S. Linderoth, M. Lundberg, S. Feih, Journal of the European Ceramic Society, 32 (2012) 4165-4176.

[8] A. Mai, B. Iwanschitz, U. Weissen, R. Denzler, D. Haberstock, V. Nerlich, A. Schuler, in: F. Lefebvre-Joud, E. Bouyer, J. Kiviaho, J. Laurencin, F.L. Naour, J. Mougin, M. Petitjean (Eds.) 10th European SOFC Forum, European Fuel Cell Forum AG, Lucerne, 2012, pp. A04-20-A04-27.
[9] A. Börger, P. Supancic, R. Danzer, Journal of the European Ceramic Society, 24 (2004) 2917-2928.
[10] A. Börger, P. Supancic, R. Danzer, Journal of the European Ceramic Society, 22 (2002) 1425-1436.
[11] R. Bermejo, P. Supancic, C. Krautgasser, R. Morrell, R. Danzer, Engineering Fracture Mechanics, 101 (2013) 108-121.
[12] R. Danzer, P. Supancic, W. Harrer, J. Ceram. Soc. Jpn., 114 (2006) 1054-1060.
[13] R. Bermejo, P. Supancic, I. Kraleva, R. Morrell, R. Danzer, Journal of the European Ceramic Society, 31 (2011) 745-753.
[14] C.H. Hsueh, C.R. Luttrell, P.F. Becher, Dental Materials, 22 (2006) 460-469.
[15] C.H. Hsueh, C.R. Luttrell, Compos. Sci. Technol., 67 (2007) 278-285.
[16] W.C. Young, R.G. Budynas, Roark's Formulas for Stress and Strain, 7th ed., MacGraw-Hill, New York, 2002.
[17] J. Kuebler, U.F. Vogt, D. Haberstock, J. Sfeir, A. Mai, T. Hocker, M. Roos, U. Harnisch, Fuel Cells, 10 (2010) 1066-1073.
[18] F. Fleischhauer, A. Tiefenauer, T. Graule, R. Danzer, A. Mai, J. Kuebler, Journal of Power Sources, 258 (2014) 382-390.
[19] A. Tsoga, A. Gupta, A. Naoumidis, P. Nikolopoulos, Acta Materialia, 48 (2000) 4709-4714.
[20] A. Mai, V.A.C. Haanappel, F. Tietz, D. Stöver, Solid State Ionics, 177 (2006) 2103-2107.
[21] B. Lawn, Fracture of Brittle Solids, Cambridge University Press, Cambridge, 1993.
[22] T. Hashida, K. Sato, Y. Takeyama, T. Kawada, J. Mizusaki, Solid Oxide Fuel Cells 11 (Sofc-Xi), 25 (2009) 1565-1572.
[23] A. Atkinson, A. Selcuk, Solid State Ionics, 134 (2000) 59-66.
[24] T. Ye, Z. Suo, A.G. Evans, International Journal of Solids and Structures, 29 (1992) 2639-2648.
[25] R. Bermejo, P. Supancic, R. Danzer, Journal of the European Ceramic Society, (2012).
[26] S.M. Wiederhorn, Journal of the American Ceramic Society, 50 (1967) 407-414.
[27] R. Danzer, T. Lube, P. Supancic, R. Damani, Advanced Engineering Materials, 10 (2008) 275-298.